Diss. ETH No. 19606

Microscopic Probing and Manipulation of Ultracold Fermions

A dissertation submitted to the
ETH ZURICH

for the degree of
Doctor of Sciences

presented by

TORBEN MÜLLER

Dipl.-Phys.,
Johannes Gutenberg-Universität Mainz, Germany

born 18.06.1980 in Weilburg, Germany
citizen of Germany

accepted on the recommendation of
Prof. Dr. Tilman Esslinger, examiner
Prof. Dr. Jonathan Home, co-examiner

2011

Kurzfassung

Diese Arbeit beschreibt Experimente, die erstmals einen lokalen Zugang zur mikroskopischen Quanten-Vielteilchen-Physik ultrakalter atomarer Fermionen erlauben. Ein Quantengas aus ^{6}Li Atomen wird *in-situ* mit zuvor nie erreichter Auflösung untersucht, wodurch ein direkter Einblick in die charakteristischen Fluktuations- und Korrelationseigenschaften des Systems gegeben ist. Auf derselben Längenskala von einem Mikrometer wird mit flexibel formbaren optischen Dipolfallen zudem eine lokale Manipulation erreicht. Wichtigstes Instrument für die gezeigten Experimente bilden zwei identische hochauflösende Mikroskopobjektive, die das Kernstück der im Rahmen dieser Arbeit aufgebauten Apparatur darstellen.

Eines der beiden Mikroskopobjektive dient zur hochauflösenden Abbildung. Mit dessen Hilfe werden räumlich aufgelöste Dichte- und Dichtefluktuationsprofile eines gefangenen, schwach wechselwirkenden Fermi-Gases gemessen und analysiert. Für Quantenentartung zeigt das Fermi-Gas unterdrückte Dichtefluktuationen unterhalb des Niveaus für thermisches Schrotrauschen. Dahingegen wird im nicht entarteten Fall thermisches, atomares Schrotrauschen beobachtet. Die gemessenen sub-Poisson'schen Fluktuationen sind eine direkte Folge des Pauli-Prinzips und manifestieren damit fermionisches Antibunching im Ortsraum. Zudem liefern die ortsaufgelösten Messungen lokale Informationen über thermodynamische Eigenschaften des Systems, wie zum Beispiel den Grad der Quantenentartung und die Kompressibilität. Gestützt auf die Aussagen des Fluktuations-Dissipations-Theorems wird eine neue fluktuationsbasierte Methode zur Temperaturmessung in atomaren Fermi-Gasen realisiert.

Darüber hinaus stellen wir eine neuartige, quanten-limitierte Interferometrie-Methode vor, die es ermöglicht Spinfluktuationen in einem gefangenen, zweikomponentigen Fermi-Gas mit Mikrometerauflösung zu detektieren. Im Vergleich zu einem thermischen Gas beobachten wir aufgrund des Pauli Prinzips eine Unterdrückung der Spinfluktuationen um 4.5dB für ein schwach wechselwirkendes, quantenentartetes Gas. Für ein stark wechselwirkendes Gas aus Feshbach-Molekülen messen wir bedingt durch die Paarbildung von Atomen mit entgegengesetztem Spin eine Reduktion der Fluktuationen um 9.2dB.

Mit Hilfe eines zweiachsigen akusto-opitschen Deflektors und der neuen hochauflösenden Optik werden mikroskopisch formbare optische Dipolpotentiale generiert. Diese umfassen sowohl statische als auch zeitgemittelte Fallenpotentiale in vielfältigen

Geometrien. Wir präsentieren die Charakterisierung einer einzelnen, stark fokussierten Dipolfalle und zeigen die Realisierung eines zweidimensionalen optischen Gitters mit 4x4 Gitterplätzen und einer Ringgitterkonfiguration aus 8 Potentialtöpfen. Zudem demonstrieren wir das ortsaufgelöste Abbilden von kalten Atomen, die in diesen projezierten optischen Potentiallandschaften eingeladen und gefangen werden.

Abstract

This thesis reports on experiments that provide for the first time a local access to the microscopic quantum many-body physics of ultracold atomic fermions. A quantum gas of ^{6}Li atoms is optically probed *in-situ* with unprecedented spatial resolution, giving direct insight into the distinctive fluctuation and correlation properties of the system. Likewise on the same length scale of one micrometer, local manipulation is achieved by means of flexible confinement in optical dipole traps. The essential tool for the presented experiments is a pair of identical, high-resolution microscope objectives that constitute the key feature of the new apparatus which has been set up in the scope of this PhD project.

Employing one of the two microscope objectives for high-resolution imaging, spatially resolved density and density fluctuation profiles of a trapped, weakly interacting Fermi gas are measured and analyzed. In the quantum degenerate regime, the Fermi gas shows a suppression of the density fluctuations below the atomic shot noise limit, whereas in the non-degenerate case thermal atomic shot noise is observed. The measured sub-poissonian fluctuations are a direct result of the Pauli exclusion principle and represent an explicit manifestation of antibunching in real space. Moreover, the spatially resolved measurements reveal local information about thermodynamic quantities such as the level of quantum degeneracy and the compressibility. Using the predictions of the fluctuation-dissipation theorem, a novel fluctuation-based method for thermometry in atomic Fermi gases is realized.

A novel shot-noise limited interferometer is introduced enabling us to measure the spin fluctuations in a trapped, two-component Fermi gas with a micrometer resolution. Compared to a thermal gas, we observe a reduction of the spin fluctuations of up to 4.5dB for a weakly interacting quantum degenerate gas due to the Pauli principle, and 9.2dB for a strongly interacting gas of Feshbach molecules due to pairing.

Using a two-axis acousto-optical deflector in combination with the microscope setup, we demonstrate the generation of microscopically tailored optical dipole potentials. Covering static as well as time-averaged potentials, versatile trapping geometries are achieved, including a tightly focussed single optical dipole trap, a 4x4-site two-dimensional optical lattice and a 8-site ring lattice configuration. Moreover, we present the spatially resolved imaging of cold atoms residing in these optically projected potential patterns.

Contents

1 Introduction 1

2 Quantum degenerate Fermi gases 7

2.1 Degenerate fermions . . . 8

2.1.1 Non-interacting trapped Fermi gas . . . 9

2.2 Interactions in an ultracold quantum gas . . . 11

2.2.1 Elastic scattering . . . 11

2.2.2 Feshbach resonances . . . 12

2.2.3 BEC-BCS crossover . . . 15

2.3 Quantum statistics . . . 19

2.3.1 Grand canonical ensemble . . . 19

2.4 Density fluctuations . . . 21

2.4.1 Fluctuations in phase space . . . 21

2.4.2 Fluctuations in real space . . . 25

2.4.3 Density fluctuations in an ultracold Fermi gas of ^{6}Li . . . 27

2.5 Fluctuation-dissipation theorem . . . 29

2.5.1 Fluctuations and susceptibilities . . . 30

2.5.2 Fluctuations and correlations . . . 31

3 Experimental setup 35

3.1 General design considerations . . . 35

3.2 Overview of the experimental setup . . . 37

3.2.1 Cooling strategy . . . 37

3.2.2 Vacuum system . . . 38

3.3 Laser cooling . . . 43

3.3.1 Laser system . . . 43

3.3.2 Zeeman slower . . . 45

3.3.3 Magneto-optical trap . . . 46

3.4 All-optical evaporative cooling . . . 48

3.4.1 Resonator trap . . . 49

3.4.2 Running wave dipole trap . . . 55

3.4.3 Optical transport . . . 57

3.5 Magnetic fields . . . 58

3.5.1 Main coils . . . 59
3.5.2 Auxiliary coils . . . 60
3.6 Imaging techniques . . . 61
3.6.1 Absorption imaging . . . 61
3.6.2 Dispersive probing . . . 63
3.6.3 Optical setup for standard imaging . . . 64
3.7 Experimental sequence towards quantum degeneracy . . . 66
3.7.1 Experimental cycle . . . 66
3.7.2 Quantum degenerate, non-interacting Fermi gas . . . 68
3.7.3 Bose-Einstein condensate of molecules . . . 69

4 Microscope setup 71
4.1 Microscope objectives . . . 71
4.1.1 Objective design . . . 72
4.1.2 Objective mounting . . . 73
4.2 High-resolution imaging . . . 75
4.2.1 Optical setup . . . 75
4.2.2 Optical performance . . . 77

5 Microscopically tailored optical potentials 81
5.1 Generation of optical micro-potentials . . . 82
5.1.1 Basic concept . . . 82
5.1.2 Optical setup . . . 82
5.2 Optical micro-potentials . . . 84
5.2.1 Single spot micro-trap . . . 84
5.2.2 Multiple spot micro-traps . . . 85
5.3 Atoms in micro-potentials . . . 87
5.3.1 Loading the micro-traps . . . 87
5.3.2 Single-site resolved imaging . . . 88
5.3.3 Lifetime in micro-traps . . . 89
5.4 Summary . . . 90

6 Local observation of antibunching 91
6.1 Introduction . . . 92
6.2 Probing density fluctuations in a trapped Fermi gas . . . 92
6.2.1 Preparation and measurement procedure . . . 93
6.2.2 Data processing . . . 94
6.3 Manifestation of antibunching in real space . . . 96
6.3.1 Density fluctuations above and below quantum degeneracy . . . 96
6.3.2 Density fluctuation profiles . . . 98
6.4 Fluctuation-based thermometry . . . 100
6.5 Summary . . . 101

7 A local interferometer probing spin fluctuations in a quantum gas 103
7.1 Local interferometry . . . 103
7.1.1 Concept of the local interferometer . . . 104

7.1.2 Imprinting atomic spin onto light phase 105
7.1.3 High-precession at the shot noise limit 106
7.2 Probing spin fluctuations in a two-component Fermi gas 107
7.2.1 Spin fluctuations in a weakly interacting Fermi gas 108
7.2.2 Spin fluctuations in a strongly interacting Fermi gas 109
7.3 Magnetic susceptibility 110
7.4 Summary 111

8 Conclusions and outlook 113

A Physical constants 117

B Atomic properties of ^{6}Li 119
B.1 Fundamental physical properties of ^{6}Li 119
B.2 Atomic level structure of ^{6}Li 120
B.3 Zeeman splitting of ground and excited state levels 121

C Noise propagation 123

D Data processing for interferometry 125

E Alignment of the microscope setup 127

Bibliography 131

Publications related to this thesis 145

Acknowledgements 147

Curriculum Vitae 149

1 Introduction

The study of quantum many-body physics has long since captured the interest of physicists, most of which has been sparked by the serendipitous discovery of new states and properties in the field of condensed matter physics. The emergence of phenomena such as superfluidity, superconductivity, the Kondo effect or the fractional quantum Hall effect, has stimulated the development of new conceptual frameworks for our basic understanding of many-body physics. In all of these systems, the physics is determined by fermionic particles whose complex collective behavior arises from the intricate interplay of interparticle interactions and the Pauli exclusion principle. Gradually, new aspects of quantum many-body theory have spread far beyond condensed matter physics, to nuclear and particle physics, and also cosmology.

Lately, a new research field related to condensed matter physics has started to address fundamental concepts of many-body physics, but from a different perspective. With the advent of ultracold atomic Fermi gases, flexible paradigm model systems have become available that provide the unique opportunity to experimentally realize and investigate quantum many-body physics in a very controlled way [1, 2]. In contrast to solid state many-body systems, dilute gases of fermionic atoms - cooled down to nanokelvin temperatures and confined in magnetic or optical traps - are very pure and offer a large variety of experimentally tunable parameters, such as the density, the temperature, and most notably the strength of interparticle interactions. Yet, the research with quantum gases pursues a fundamentally different approach to many-body physics. While in solid state physics observations triggered the search for a theoretical explanation, experiments with ultracold atoms often revisit known models and attempt to further explore emergent many-body phenomena therein. The crossover between Bose-Einstein condensation and Bardeen-Cooper-Schrieffer superfluidity represents a prominent example, which currently is intensively studied in strongly interacting Fermi gases [3]. Whether this approach - commonly referred to as quantum simulation - may soon profoundly influence our further understanding of quantum many-body physics is strongly dependent on practical experimental methods to prepare, manipulate and probe these model systems. In particular, new experimental techniques are needed to reveal sufficient details about strongly correlated quantum phases in order to be able to verify and even anticipate theoretical results. The desire for such novel tools sets the framework of this thesis.

Currently, increasing experimental effort in the research field of ultracold atoms is directed towards the development of tools to probe and manipulate quantum gases with high spatial resolution [4, 5, 6, 7]. Access to the underlying physics at a microscopic scale is now within reach. In this thesis, we present a new experimental apparatus - featuring two high-resolution microscope objectives - that allowed us for the first time to locally probe the distinctive many-body physics of an ultracold Fermi gas of ^{6}Li atoms at the fundamental length scale of the Fermi wavelength.

A key concept of quantum many-body physics are correlations whose importance was already highlighted by Nobel laureate J. Schwinger in a series of publications on the theory of many-particle systems half a century ago: "The quantities that fully describe the local behavior, and which thereby serve to characterize both the macroscopic and the microscopic aspects of the situation, are time dependent field correlations, or, in the language of field theory, Green's functions." [8]. In general, correlations emerge from the interplay of interparticle interactions and quantum statistics. In the case of fermions, the quantum statistic is given by the Fermi-Dirac distribution [9, 10, 11], or equivalently by the Pauli exclusion principle. One consequence of the Pauli exclusion principle is that ordered phases in ultracold Fermi gases are not directly reflected in the density or momentum profile of the atomic cloud. Hence, e.g. superfluidity of paired fermions in the BEC-BCS crossover does not become apparent as a coherence peak in the density profile [12], in contrast to the bosonic case, where the condensed fraction is discernible by its low momentum. [13, 14].

Most fundamentally, quantum mechanically induced correlations between the constituents of a many-body system manifest themselves in the noise properties of the system. Here, noise refers to the distinctive fluctuations of a physical observable such as the particle number or the magnetization. For a few years, the correlation induced noise properties of quantum gases have become the subject of many theoretical investigations, covering both bosonic and fermionic systems [12, 15, 16]. Meanwhile, correlations in systems of ultracold quantum gases have also been addressed experimentally. Very different approaches have been pursued which partly accessed the intrinsic correlations via the noise properties of the system, but nearly all rely on techniques to probe the quantum correlations indirectly, i.e. to globally map the microscopic correlation effects onto macroscopic observables. Such probing techniques include for example Hanbury Brown–Twiss-like experiments to reveal bunching and antibunching effects of bosonic and fermionic atoms respectively [17, 18, 19, 20], dissociation of atom pairs to detect the pair correlations of weakly bound molecules in time of flight experiments [21], measurements of the double occupancy in a 3D optical lattice to probe nearest-neighbor correlations in the fermionic Mott insulator [22], and Bragg spectroscopy in strongly interacting Fermi gases to measure the static structure factor which corresponds to the Fourier transform of the pair correlation function in real space [23, 24, 25].

So far, only few experiments have focussed on the direct *in-situ* measurement of correlations in atomic quantum gases, currently restricted to Bose gases in low dimensions only [26, 27, 28], while corresponding measurements of correlations in Fermi gases remain elusive. A closer look at the distinctive correlations of a Fermi gas, such as density-density correlations, shows that their smallest fundamental length scale is given by the Fermi wavelength λ_F [29]. In ultracold Fermi gases, λ_F is typically of the order of one micrometer, which is in principle accessible by optical means but places high demands on the spatial resolution for the *in-situ* probing technique.

Within the scope of this thesis we set up a new experimental apparatus that offers the unprecedented opportunity to access the physics of strongly correlated Fermi gases at a microscopic scale length. Employing a high-resolution microscope imaging setup with a maximum resolution of 660 nm, we demonstrate the *in-situ* measurement of density fluctuations in a weakly interacting Fermi gas of trapped ^{6}Li atoms. The observed sub-Poissonian density fluctuations for a quantum degenerate gas provides the first direct manifestation of fermionic antibunching in real space, a textbook proof of the most fundamental particle correlations present in a fermionic system. Due to the high spatial resolution this measurement also constitutes a local probe of quantum degeneracy in the trapped Fermi gas. In thermal equilibrium, the density fluctuations are universally linked to the thermodynamic properties of the gas via the fluctuation-dissipation theorem. Using this relation, we demonstrate a novel type of fluctuation-based thermometry universally applicable to quantum gases.

In a complementary approach we have developed a novel method for an interferometric measurement of the magnetization in a Fermi gas. It allows to implement a recently proposed concept to characterize the strong correlations in the ground-state of an interacting many-body systems [30]. The method combines the two decisive benefits given by the shot noise limited precision of interferometric measurements on the one hand, and the high spatial resolution of our microscope setup on the other hand. With this we were able to locally measure the spin fluctuations in a trapped, two-component Fermi gas. In comparison to a thermal gas, we observe a strong suppression of spin-fluctuations due to the Pauli principle in a weakly interacting, quantum degenerate cloud. In addition, we find an even more pronounced spin squeezing effect in a strongly interacting gas due to the formation of molecules.

Besides the detection of correlations, another pending challenge concerns the microscopic manipulation and preparation of atomic quantum gas. In addition to the tunability of the interaction strength with so-called Feshbach resonances, the high level of controllability on these systems also relies on versatile tools to manipulate the confinement and thus the external degree of freedom. For this, optical dipole traps [31] offer a huge variety of applications. In particular, the use of optical lattices - artificial crystals of light formed at the intersection of three standing light waves - established an entire new research field, also allowing to access the strongly interacting regime [32, 33]. Currently, experiments with ultracold fermions or bosons in optical lattice pursue a novel route to emulate fundamental model Hamiltonians of condensed matter physics. More precisely, these systems constitute an almost ideal experimental realization of the Hubbard model with highly tunable parameters [34, 35]. Very recently, even single site resolution imaging has been achieved for bosonic systems [36, 37, 7]. However, the concept of optical lattices is by design restricted to the investigation of periodic systems with a high degree of symmetry. In this thesis, we reach out for an extension of optical potentials towards more flexible trapping geometries. With the help of a second high-resolution microscope objective, we demonstrate the generation of versatile optical dipole potentials that can be shaped down to length scales well below one micrometer. Moreover, we show the ability to load and detect a small number of cold fermionic atoms in these trapping potentials.

Review on the recent experimental research with ultracold fermions

For more than ten years, ultracold atomic Fermi gases have been enjoying ever increasing attention, and are currently studied in a broad spectrum of experiments at the forefront of atomic physics. Four years after the first experimental realization of atomic Bose-Einstein condensation in 1995 [13, 14], the onset of quantum degeneracy in an atomic Fermi gas was observed for the first time in a magnetically trapped sample of evaporatively cooled ^{40}K atoms [38]. Here, the Pauli principle posed a natural barrier for further cooling since collisions between identical fermions of the same spin are strongly suppressed at this low temperatures. Two years later, deeper degeneracies could be achieved via sympathetic cooling in the presence of bosonic species, thereby reaching relative temperatures of the order of 20 percent of the Fermi temperature [39, 40, 41, 42].

Around the same time, the development of optical dipole traps had already achieved great success, providing a very versatile alternative to magnetic trapping potentials [31]. Consequently, the first all-optical preparation of a quantum degenerate Fermi gas was demonstrated in 2002 [43]. In particular, optical traps offer the very positive side effect of liberating the atomic spin degree of freedom since any spin states can be trapped. In turn, this enabled the employment of external magnetic fields to tune the interaction properties between different spin states by means of so-called magnetic Feshbach resonances [44]. For the fermionic isotope ^{6}Li, theoretical calculations [45] predicted the existence of a broad Feshbach for the s-wave scattering length between the two lowest spin states of the hyperfine ground state [46], whose exact position was experimentally located around a magnetic field of about 840 G [47, 48]. Henceforth, Feshbach resonances have turned out to be an extremely useful tool in cold atom experiments as they allow to precisely control the interaction strength of two colliding particles from zero to nearly any attractive or repulsive value. Among other properties, this tunability of the interaction strength founds the current experimental appeal of ultracold quantum gases. Most of all, Feshbach resonances finally paved the way to enter the regime of strong interactions and thus strong correlations, which apart from experiments with optical lattices had not been accessible so far.

Shortly after the first advance towards strongly interacting atomic Fermi gases [49], experiments with fermions - most of them working with ^{6}Li - started to explore the twofold pairing behavior for attractive and repulsive interparticle interaction respectively. In the case of repulsive interactions between two particles of opposite spin, a bound state emerges supporting the formation of weakly bound dimers. Though the constituents are fermions, the dimers themselves are of bosonic nature, for which the phase transition into a molecular Bose-Einstein condensate (BEC) was demonstrated by three different groups in quick succession [50, 51, 52]. On the other hand, for attractive interactions the system favors a Cooper pair like state similar to that known from the Bardeen-Cooper-Schrieffer (BCS) theory of superconductors [53]. In contrast to the BEC regime, the BCS regime is governed by genuine many-body physics. As a unique opportunity offered by cold samples of ^{6}Li and ^{40}K atoms, the Feshbach resonance connects both regimes. Exploiting this, a considerable number of outstanding experiments studied the pairing behavior in this so-called BEC-BCS crossover that encompasses a unitarity limited interaction regime around the resonance, where the scattering length diverges [54, 55, 56, 57, 58, 59, 60]. Pairing of fermions is a prerequisite condition for superfluidity which was expected to occur throughout the entire crossover regime, but whose experimental emergence in atomic Fermi gases remained elusive for a long time. Finally, the observation of long-lived, ordered vortex lattices in a rotating balanced Fermi mixture provided the convincing evidence for superfluidity [61]. In addition, both experimentalists and theorists investigated the question to which extent superfluidity can be sustained in imbalanced Fermi mixtures, i.e. for unequal atom numbers in both spin components. Measurements revealed a breakdown of superfluidity beyond a critical imbalance, the Clogston limit, and the sample was found to separate into a core region of equal densities, surrounded by a shell at unequal densities [62, 63, 64, 65, 66]. Currently, an open issue about the existence of a pseudo-gap phase in the unitarity regime of strong interactions is controversially discussed. A recent experiment found evidence that pair formation - according to conventional BCS theory occurring in coincidence with superfluidity - may already appear above the critical temperature for the superfluid phase transition [67]. The unitarity regime between the two well-understood limiting situations of BEC and BCS is of special interest because there the interaction reaches the maximum allowed value and the Fermi energy sets the only relevant energy scale. By nature, any other unitarity limited Fermi system, such as neutron stars, shares the same universal thermodynamic properties, and very recently, experiments and theory have started to explore the universal thermodynamics of strongly interaction systems [68, 69, 70, 71]. Hence, this link given by universality nicely demonstrates how highly controllable atomic Fermi gases may reveal details about other unitary Fermi systems.

Clearly, the exploration of many-body physics using ultracold quantum gases continues to gain momentum. In general, the experimental research now progresses towards gaining more quantitative insights into the underlying physics of the very intriguing regimes described above. As we have seen, the related phenomena are driven by pair formation and are characterized by spin correlations, which typically vary in space. The new apparatus presented in this thesis offers for the first time the ability to observe those effects on their relevant length scales, and thus may contribute to reach the next step towards a more quantitative understanding.

Outline of this thesis

The work presented in this thesis was carried out in close collaboration with Bruno Zimmermann, Jakob Meineke, Henning Moritz, Jean-Philipp Brantut, and David Stadler.

- The second chapter introduces the theoretical framework for the description of ultracold atomic Fermi gases, including the physics of low temperature interactions. The main part of this chapter focusses on the relation between quantum statistics, density fluctuations, correlations and thermodynamic properties of a Fermi system.
- In the third chapter, the design of our new apparatus is presented which was set up during the first two years of this thesis. Besides a detailed description of all relevant components, we also discuss the experimental sequence used to produce a quantum degenerate Fermi gas of ^{6}Li atoms.
- The fourth chapter is devoted to the key feature of our apparatus, the high-resolution optical setup aiming at the microscopic probing and manipulation of ultracold fermions. We first discuss the technical details of the two microscope objectives which represent the core part of the optical setup. Subsequently, we characterize the performance of the high-resolution imaging system that employs one of the two microscopes.
- The preparation of ultracold fermions in microscopically tailored optical dipole potentials is subject of the fifth chapter. Using the second microscope objective and an acousto-optical deflector, we demonstrate the generation of various micro-trap configurations. Moreover, we show the single-site resolved imaging of ultracold fermions populating the micro-traps arrays.
- In the sixth chapter, we present a textbook experiment on the local observation of antibunching in a trapped Fermi gas, constituting a local probe of quantum degeneracy. We analyze the measured density fluctuations in the framework of the fluctuation-dissipation theorem and provide a promising route for fluctuation-based temperature measurements in Fermi gases.
- The seventh chapter reports on the *in-situ* measurement of spin-fluctuations in a weakly and strongly interacting two-component Fermi gas. For this measurement, we have developed a novel shot-noise limited interferometric technique with high spatial resolution that allows us to characterize distinctive correlations of the quantum gas in a spatially localized region.

2 Quantum degenerate Fermi gases

The system under investigation throughout this thesis is an ultracold Fermi gas of ^{6}Li atoms confined in an optical dipole trap. As we will derive in the following chapter, the ground state of such an ensemble in the absence of interaction effectively realizes the textbook example of the ideal Fermi gas. Including interactions, the ground state of the system changes dramatically and the spin degree of freedom plays an important role. In a two-component Fermi gas, already small attraction between particles of different spin may cause the formation of atomic Cooper pairs which are able to condense into a superfluid below a critical temperature. This superfluid state of neutral particles directly corresponds to the many-body state of electronic Cooper pairs in solid state superconductors, both of which are well described by the Bardeen-Cooper-Schrieffer (BCS) theory [53]. On the other hand, for repulsive interactions two particles can form a bound state of molecular dimers, which can undergo a phase transition into a Bose-Einstein condensate (BEC) of molecules. What is most exciting about ultracold atomic quantum gases is the capability to precisely control the interparticle interaction by means of so-called Feshbach resonances. By this, the scattering length between two colliding particles can be tuned from zero to any arbitrary large attractive or repulsive interaction, which finally allowed experiments on ultracold Fermi gases to enter the regime of strongly correlated many-body physics. Resuming the argumentation of the introduction, quantum mechanically induced correlations emerge from the interplay of quantum statistics and interactions, and manifest themselves in distinctive fluctuations of physical observables, such as the particle number or the magnetization. Measurements of such fluctuations are becoming increasingly important as they provide direct access to key quantities that characterize the many-body system.

In the following chapter, we discuss the theoretical framework of ultracold atomic Fermi gases. Starting with the description of an ideal Fermi gas, we subsequently summarize the physics of collision-based interactions and the concept of Feshbach resonances in ultracold quantum gases. Based on that, we discuss the different interaction regimes and related phenomena of the so-called BEC-BCS crossover. For further reading, we refer to the textbooks [72, 73] and to the detailed review article [3] which provide an excellent introduction to this field. The main part of this chapter focusses on the quantum statistics and thermodynamic properties of Fermi systems.

Thereby, we place strong emphasis on the role of density fluctuations and particle correlations.

2.1 Degenerate fermions

In the classical limit at high temperatures, the constituents of a dilute atomic gas can be considered as distinguishable, point-like particles. However, the situation changes for low temperatures. As as soon as the thermal deBroglie wavelength λ_{dB} becomes comparable to the mean interparticle separation, i.e. when the wave packets of individual particles start to overlap, the statistics of the gas is governed by quantum mechanics: identical particles become indistinguishable and the intrinsic angular momentum, the spin, starts to play a dominant role. At this point, the underlying quantum statistics leads to fundamental differences depending on whether the particles are bosons (particles with integer spin) or fermions (particles with half-integer spin). Fig. 2.1 qualitatively depicts the different behavior of bosons and fermions trapped in a harmonic potential. When the gas is cooled below quantum degeneracy, bosons condense into the ground state of the trap, thereby undergoing the phase transition to a Bose-Einstein condensate (BEC). In contrast, fermions obey the Pauli exclusion principle which prohibits two identical fermions to occupy the same quantum state. According to this, fermions start to fill up the lowest lying states of the

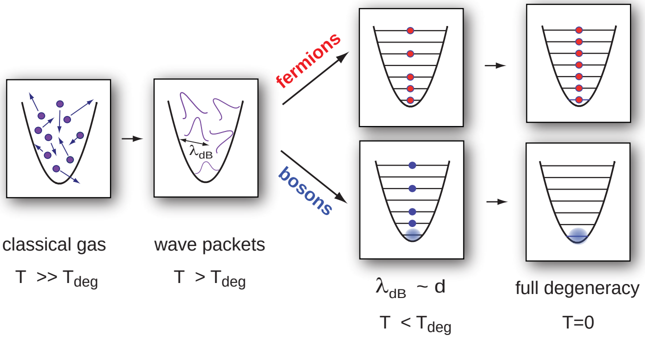

Fig. 2.1: Cooling a gas of identical particles down to quantum degeneracy causes the point-like character of distinguishable particles to fade out and their wave-like nature to show up. When the thermal deBroglie wavelength λ_{dB} reaches the order of the interparticle separation, the specific particle statistics becomes important and leads to contrary situations for bosons and fermions. Bosons start to condense into a single quantum state, the ground state of the trap. In contrast, fermions start to fill up the lowest lying trapping states due to the Pauli principle, which causes them to avoid each other. At zero temperature, the Bose gas is fully condensed, all particles behave coherently and are described by a single wave function. On the other hand, fermions fill the energy levels of the trap from the bottom to the Fermi energy with unity occupation.

trap with unity occupation, thereby forming a Fermi sea at temperatures below the Fermi temperature. Experimentally, both situations, the BEC and the quantum degenerate Fermi gas, have been successfully realized with ultracold atoms [13, 14, 38] and are the starting point of many intriguing experiments worldwide.

2.1.1 Non-interacting trapped Fermi gas

At very low temperatures, interactions between two fermions in the same internal state are essentially absent because the only relevant scattering process, s-wave scattering, is suppressed by the Pauli principle (see section 2.2). Therefore, in first approximation, the properties of an ultracold atomic quantum gas consisting of single-component fermions can be derived by treating the particles as non-interacting and the ensemble as the textbook example of an ideal Fermi gas. In the following we consider the atoms to be confined in a trapping potential $V_{\mathrm{trap}}(\boldsymbol{r})$. Although the trap isolates the gas from an external reservoir, it is convenient to study the system in the grand canonical ensemble, i.e. in terms of the temperature T and the chemical potential μ. At thermal equilibrium, the mean occupation number of a phase space cell is given by the Fermi distribution function [74]

$$f_{\mathrm{F}}(\boldsymbol{r},\boldsymbol{p},T)=\frac{1}{e^{\left(\frac{\boldsymbol{p}^2}{2m}+V_{\mathrm{trap}}(\boldsymbol{r})-\mu\right)/(k_{\mathrm{B}}T)}+1}\,, \tag{2.1}$$

where $\boldsymbol{r}$ and $\boldsymbol{p}$ are position and momentum of a particle with mass m, and k_{B} is the Boltzmann constant. The chemical potential μ is determined by the total number of atoms N via the constraint that the integration of (2.1) over the full real space V and momentum space P corresponds to the total atom number:

$$N=\int_P\int_V f_{\mathrm{F}}(\boldsymbol{r},\boldsymbol{p},T)d\boldsymbol{p}^3\,d\boldsymbol{r}^3\,. \tag{2.2}$$

In general, the chemical potential μ depends on temperature. At zero temperature, it becomes by definition the Fermi energy E_{F}, which corresponds to the energy of the highest occupied state in the trap. In many experimental situations, the trapping potential for ultracold atoms can be assumed to be an anisotropic harmonic oscillator potential with oscillation frequencies $\omega_{x,y,z}$ along the principal axes x, y and z,

$$V_{\mathrm{trap}}(\boldsymbol{r})=\frac{1}{2}m\left(\omega_x^2x^2+\omega_y^2y^2+\omega_z^2z^2\right)\,. \tag{2.3}$$

The system is then described by the Hamiltonian $\hat{H}=\frac{1}{2m}(\hat{p}_x^2+\hat{p}_y^2+\hat{p}_z^2)+V_{\mathrm{trap}}(\hat{r})$, and for a given total atom number N, the integration of (2.2) at $T=0$ yields the Fermi energy

$$E_{\mathrm{F}}=k_{\mathrm{B}}T_{\mathrm{F}}=\hbar\overline{\omega}(6N)^{1/3}\,. \tag{2.4}$$

Here, $\overline{\omega} = (\omega_x \omega_y \omega_z)^{1/3}$ is the mean oscillation frequency. Equation (2.4) also defines the Fermi temperature T_F which marks the crossover to the degenerate Fermi gas, when the mean occupation number in the center of the trap approaches unity.

The density distribution of a trapped cloud of fermions in its ground state is obtained in the Thomas-Fermi approximation. In this semi-classical approximation, the kinetic energy in the Hamiltonian $\hat{H}$ is considered to be much smaller than the trapping potential, and therefore it is neglected. Hence, the properties of the gas at a certain point $\boldsymbol{r}$ are assumed to match those of a uniform gas with a density equal to the local density $n(\boldsymbol{r})$. Finally, the integration of (2.1) over momenta $|\boldsymbol{p}| < \sqrt{2m(E_\mathrm{F} - V_\mathrm{trap}(\boldsymbol{r}))}$ gives

$$n(\boldsymbol{r}, T=0) = \frac{1}{6\pi}\left(\frac{2m}{\hbar^2}\left[\mu - V_\mathrm{trap}(\boldsymbol{r})\right]\right)^{3/2} . \tag{2.5}$$

At *zero temperature*, the condition $V(R_{TF,i}) = \mu = E_\mathrm{F}$ determines the maximum extensions of the cloud, denoted as Thomas-Fermi radii $R_{TF,i} = \sqrt{2\mu/(m\omega_i^2)}$. With these, the total number of particles is obtained by integrating the density over the volume of the cloud $N = \frac{\pi^2}{8} n(\boldsymbol{r}=0) R_x R_y R_z$. In addition, the local density $n(\boldsymbol{r})$ is related to the local Fermi wave number via

$$k_\mathrm{F}(\boldsymbol{r}) = (6\pi^2 n(\boldsymbol{r}))^{1/3}. \tag{2.6}$$

This relation shows that the wave number is maximum at the trap center, and moreover of the order of the average interparticle separation, as in a homogeneous gas. While the density distribution can be anisotropic, the momentum distribution of a non-interacting Fermi gas is always isotropic, independent of the trapping potential. This is a consequence of the isotropy of the single-particle kinetic energy in momentum space.

At *finite temperature*, $0 < T \leq T_\mathrm{F}$, the density distribution is mainly modified only at the wings of the cloud. Here, the integration of (2.1) over momentum results in a polylogarithm function

$$n(\boldsymbol{r}, T) = \frac{1}{(2\pi\hbar)^3} \int_P f(\boldsymbol{r}, \boldsymbol{p}, T) d\boldsymbol{p}^3 = -\frac{1}{\lambda_{dB}^3} Li_{3/2}\left(-e^{(\mu(N,T) - V(\boldsymbol{r}))/(k_B T)}\right) , \tag{2.7}$$

where $Li_n(z) = \sum_{k=1}^{\infty} z^k/k^n$ is the n^{th}-order polylogarithm function and $\lambda_{dB} = \sqrt{\frac{2\pi\hbar^2}{m k_B T}}$ is the thermal deBroglie wavelength.

In the experiment, the temperature of the atomic Fermi gas can be determined from the analytic form of the density distribution (see e.g. section 6.4). Releasing the trapped cloud from the confining potential leads to a free ballistic expansion for the non-interacting particles. Thereby, the distinctive shape of the density distribution remains unchanged over a certain time of flight (TOF). The expanded cloud is finally imaged by means of absorption imaging onto a charged coupled device (CCD) camera, which records the integrated two-dimensional column density distribution. Analytical scaling expressions, which depend on the underlying trapping potential, allow to relate the experimentally accessible column density back to the in-trap three-dimensional density distribution. Fitting an appropriate function to the expanded density distribution yields the fugacity $z = e^{\mu/(k_\mathrm{B}T)}$, the only remaining parameter which determines the ratio T/T_F. For a harmonic trapping potential (2.3), the corresponding relation between the fugacity and the relative temperature is derived by integration and re-arrangement of equation (2.2) for $T \geq 0$,

$$T/T_F = (-6Li_3(-z))^{-1/3} \ . \tag{2.8}$$

In chapter 6 we will refer back to these equations when reporting on the observation of density fluctuations in a nearly non-interacting Fermi gas.

2.2 Interactions in an ultracold quantum gas

While a non-interacting Fermi gas impresses by its simplicity, many exciting phenomena of fermionic systems, like superfluidity or superconductivity, rely on the presence of interactions. It is a unique attribute of ultracold quantum gases that the properties of the interparticle interactions can be precisely adjusted via so-called Feshbach resonances. This high level of control plays an important role in every stage of our experiment: interactions between different spin states are indispensable not only for evaporative cooling of an atomic Fermi gas below quantum degeneracy, but also for the formation of weakly bound dimers [75, 76] which can be cooled into a molecular Bose-Einstein condensate [50, 51, 52]. In addition, Feshbach resonances open the way to tune atomic Fermi gases into regimes of arbitrarily attractive and repulsive interactions which eventually triggered the experimental exploration of the crossover between Bose-Einstein condensation of tightly bound molecules and the superfluid BCS-like state of weakly bound Cooper pairs [54, 57, 58, 61, 63]. In this section, we shortly summarize the basic concepts of scattering and interactions in ultracold quantum gases as well as the mechanism of Feshbach resonances. A detailed description of low energy collision physics can be found in [46, 77]. A comprehensive description of Feshbach resonances is given by [44, 78].

2.2.1 Elastic scattering

Interactions in quantum gases are mediated by scattering processes which take place in a Lennard-Jones potential $V_\mathrm{scat}(\boldsymbol{r})$ as illustrated in Fig. 2.2(a). The specific shape of the potential is caused by the strong repulsion of the overlapping electron clouds at short distances and the van der Waals interaction $\propto \frac{1}{r^6}$ at long distances. In quantum mechanics, the solution for the elastic scattering of two particles in the center of mass frame is expressed by an incoming plane wave with momentum k and an outgoing spherical wave whose amplitude is modulated by the scattering amplitude [46]. For large distances it reads

$$\psi(\theta, \boldsymbol{r}) \sim \exp ikz + f(\theta, k)\frac{\exp ikr}{r} \,. \tag{2.9}$$

All the physics is contained in the scattering amplitude $f(\theta, k)$ which depends on the incident scattering energy $E_0 \propto k^2$ and the scattering angle θ between the incoming particle and the observation direction. The integration of $f(\theta, k)$ over the solid angle yields the total scattering cross section. Since the scattering potential is spherical symmetric, the wave function (2.9) can be expanded in partial waves, which themselves separate into a radial term $R_{kl}(r)$ and an angular term $f_l(\theta, k) \propto k^{2l}$ with a quantized angular momentum l. The effect of scattering is to add an extra phase δ_l to each partial wave. In the low energy limit of ultracold temperatures, the scattering energy is very small ($E_0 \simeq 0$), and therefore only the lowest angular momentum $l = 0$ has to be considered. Hence, the isotropic s-wave scattering is the only relevant contribution, and the amplitude f_0 sufficiently describes the full scattering process. An important conclusion of this is that for low temperatures identical fermions do not collide due to the requisite anti-symmetric shape of the total wave function. Thus, identical fermions form an ideal Fermi gas (see previous section), and scattering of fermions at low temperatures only occurs between particles in different spin states. It can be shown that f_0 is related to the background scattering length a_{bg} via $-f_0 = a_{\mathrm{bg}} = \delta_0/k$. The exact value of the scattering length a_{bg} depends on the scattering potential. If the interatomic scattering potential is deep enough to support a bound state just below the threshold with a binding energy E_{B}, the background scattering length a_{bg} is positive and the binding energy is given by $E_{\mathrm{B}} = -\frac{\hbar^2}{m a_{\mathrm{bg}}^2}$. When the bound state approaches the continuum, the scattering length gets larger and finally diverges when the bound state coincides with the continuum. Vice versa, just above the continuum one can find a quasi-bound state, and a_{bg} becomes negative.

2.2.2 Feshbach resonances

For a given interatomic scattering potential, the background scattering length a_{bg} is constant. However, a Feshbach resonance, a phenomenon first discussed in the field of nuclear physics [79], allows to tune the scattering length a of an atomic quantum gas to any repulsive ($a > 0$) or attractive ($a < 0$) value by applying an external magnetic field. In the following section, we discuss the nature of Feshbach resonances using the example of the broad Feshbach resonance between the two lowest hyperfine sub-states of ^{6}Li at 834 G. Above a homogeneous magnetic field of 140 G, the Zeeman level structure of ^{6}Li enters the Paschen-Back regime where the two lowest spin states $|1\rangle$ and $|2\rangle$ (see appendix B.3) show the same electronic spin $m_s = -\frac{1}{2}$. An incoherent mixture of colliding atoms in these two states thus interacts via a triplet scattering potential which is called the *open channel* and is characterized by the background scattering length a_{bg} (see Fig. 2.2(a)). In principle, scattering of ultracold atoms is a multi-channel process due to different available hyperfine states. However, the scattering potential corresponding to the singlet scattering state of ^{6}Li, in which the electron spins of two colliding atoms have opposite quantum numbers $m_s = \pm\frac{1}{2}$, is not available for the incident atoms since the scattering continuum of the singlet state is higher in energy than the continuum of the triplet state (see Fig. 2.2(a)). The singlet state is therefore called a *closed channel*. Atoms scattering in the open channel may however couple to the closed channel, for example via hyperfine coupling. A Feshbach resonance occurs when the collision energy of the two colliding atoms in the open channel is close to the energy of the bound state of the closed channel. Owing to enhanced second order processes during the collision, the two atoms can virtually occupy the bound state of the closed channel, which modifies the scattering phase shift and thus influences the value of the scattering length a in the open channel.

Since the triplet and singlet scattering states have different magnetic moments ($\Delta\mu = \mu_{sgl} - \mu_{tri}$), one can use a homogeneous magnetic field B to tune the two potential curves with respect to each other. Due to the coupling to the bound state in the closed channel, as described above and illustrated in Fig. 2.2(b), the scattering length a of the open channel thereby changes from negative to positive values and diverges to $\pm\infty$ on both sides of the resonance.

The B-field dependence of the scattering length in the vicinity of the broad (open channel dominated) Feshbach resonance between 600 G and 1200 G is well described

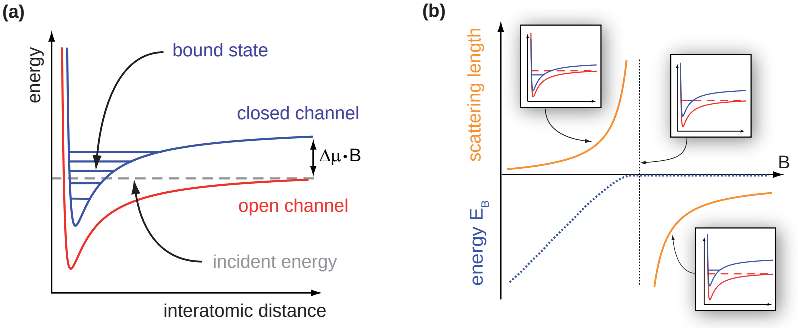

Fig. 2.2: (a) Scattering potentials of two colliding atoms in a spin-triplet (red) and spin-singlet (blue) configuration, which are denoted as open and closed channel respectively. The bound states in the closed channel can be tuned relative to the continuum of the open channel. A Feshbach resonance occurs when a bound state of the closed channel becomes energetically resonant to the incident energy of the colliding particles entering the open channel at the continuum threshold. (b) Resonant behavior of the scattering length a (orange line) as function of the magnetic field B which tunes the relative position of the bound state. The insets illustrate qualitatively the relative scaling of the scattering potentials. At B_0, the scattering length diverges. Above the resonance, the scattering length is negative (attractive interaction), whereas below the resonance it becomes positive (repulsive interaction). There, a bound state exists, whose binding energy is plotted as blue dotted line.

by [47, 80]

$$a = a_{\mathrm{bg}} \left(1 + \frac{\Delta B}{B - B_0}\right) (1 + \alpha(B - B_0)) , \tag{2.10}$$

where B_0 marks the center position and ΔB denotes the width of the Feshbach resonance. The numerical parameters for ^{6}Li read $a_{\mathrm{bg}} = -1405\,\mathrm{a}_0$, $B_0 = 834.15\,\mathrm{G}$, $\Delta B = 300\,\mathrm{G}$ and $\alpha = 0.040\,\mathrm{kG}^{-1}$ [47, 48]. Here, a_0 corresponds to the Bohr radius. In Fig. 2.3, the scaling of the scattering length between the two lowest spin states of ^{6}Li is plotted over a larger range of the magnetic field B, from 0 G to 1500 G.

Above the resonance, no real bound state exists and the scattering length is negative. For large magnetic fields, a saturates at a large off-resonant background scattering length of $a_{\mathrm{bg}} = -2000\,a_0$, which originates from a virtual bound state just above the scattering continuum of the open channel. On resonance, the bound state crosses the continuum of the open channel and the scattering is resonantly enhanced, subsequently changing the sign. Below the resonance, the bound molecular state is energetically below the continuum of the open channel (see Fig. 2.2(b)), and a resulting bound eigenstate evolves whose B-field dependent binding energy E_{B} is plotted as blue dotted line in Fig. 2.2(a). In analogy to the avoided crossing in a two level system, the resulting bound state is connected adiabatically to the free-atom continuum when the closed channel is tuned into the continuum. Thus, by adiabatically ramping the magnetic field across the resonance, pairs of atoms can be converted into molecules [76]. The reverse process dissociates the dimers. However, the bound state stems from the coupled system, and the formed molecules are a coherent superposition of the bound molecule in the closed channel and a long-range atom pair in the open channel.

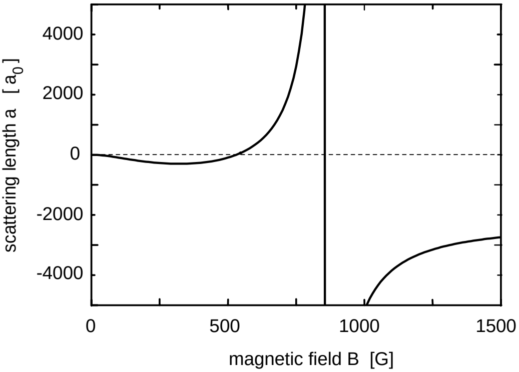

Fig. 2.3: Scattering length a between the two lowest hyperfine sub-states of ^{6}Li across a magnetically tuned Feshbach resonance. The plotted data rely on a coupled-channel calculation [81]. The position of the broad Feshbach resonance was experimentally determined to be located at $B = 834\,\mathrm{G}$ [47, 48]. The scattering length a is given in units of the Bohr radius a_0.

Apart from the broad Feshbach resonance between the two lowest spin states of ^{6}Li at $B = 834\,\mathrm{G}$, there also exists another very narrow ($\Delta B = 0.1\,\mathrm{G}$) Feshbach resonance at $B = 543\,\mathrm{G}$ for the same states (not shown in Fig. 2.3). Moreover, at $B = 527\,\mathrm{G}$ [82], there is a zero-crossing of the scattering length a, which enables the realization of a non-interacting Fermi gas in our experiments. For even lower magnetic fields, the scattering length further decreases to a local minimum of about $-300\,a_0$ at $B \simeq 325\,\mathrm{G}$, and subsequently smoothly increases to zero at zero magnetic field (see Fig. 2.3).

2.2.3 BEC-BCS crossover

The unique possibility to tune the interactions in ultracold Fermi gases opened the path to experimentally address a long-standing problem in many-body physics: As proposed by Eagles [83] in 1969 and finally shown by Leggett [84] in 1980, there exists a smooth crossover of a superfluid system from the Bose-Einstein condensate regime of tightly bound molecules into the Bardeen Cooper Schrieffer (BCS) regime of weakly bound Cooper pairs. In this section we summarize the basic phenomena related to this crossover as it appears in a strongly interacting gas of ultracold ^{6}Li atoms. There, both regimes are smoothly connected due to the variable interaction strength across the Feshbach resonance. Theory-wise, the crossover can be parameterized by the dimensionless quantity $1/k_\mathrm{F}\,a$, where k_F is the Fermi momentum and a the scattering length. To give an intuitive picture of how the entire crossover regime was covered for the first time in a single quantum system [55, 59, 85, 56, 54, 86], we first consider the two limiting cases of BEC ($1/k_\mathrm{F}\,a \gg 1$) and BCS ($1/k_\mathrm{F}\,a \gg -1$) in an interacting Fermi gas. Here, the nature of pairing is the key element for the further understanding how the many-body state evolves from two-body pairing in real space (BEC) to Cooper pairing in momentum space (BCS). In between ($1/k_\mathrm{F}\,a \ll 1$), the quantum gas is strongly interacting and limited by unitarity, i.e. independent of any particularities of the interaction properties. For weak interactions, both limiting cases can be described in the framework of well-established theory. However, for strong interactions the BEC and BCS approaches break down and the description of the strongly interacting system turns out to be a difficult task, which poses great challenges for many-body quantum theories.

BEC limit

Two fermionic atoms can be transferred into a bosonic molecule by adiabatically ramping the magnetic field across the resonance towards repulsive interaction. The formation of so-called Feshbach molecules was first demonstrated with ^{40}K atoms [76]. In the case of ^{6}Li, these diatomic molecules populate the highest vibrational state with a vibrational quantum number $\nu = 38$. Close to the resonance their binding energy is given by

$$E_B = \frac{\hbar^2}{2m_r a^2}\,, \tag{2.11}$$

where m_r is the reduced mass of both atoms. The binding of the molecules becomes deeper when going further away from the resonance towards lower magnetic fields. There, the scaling of the binding energy with the scattering length is modified since the range of the van der Waals interaction, defined by $r_{\mathrm{eff}} = \left(\frac{mC_6}{\hbar^2}\right)^{1/4}$, now reaches the extension of the scattering length a. With the van der Waals C_6-coefficient $C_6 = 1.3340 \times 10^{-76}\,\mathrm{Jm}^6$ for ^{6}Li, the scattering length a has to be modified by a mean scattering length $\overline{a} = \frac{\Gamma(3/4)}{2\sqrt{2}\Gamma(5/4)} r_{\mathrm{eff}}$ to account for the finite extent of the scattering potential. The binding energy far off from resonance can be calculated by

$$E_{\mathrm{B}} = \frac{\hbar^2}{2m_r(a-\overline{a})^2}\,. \tag{2.12}$$

The molecules, although their constituents are fermions, are of bosonic nature and therefore can undergo the phase transition into a molecular Bose-Einstein condensate (BEC) at a critical temperature T_C. This temperature is independent of the binding energy, but only determined by the bosonic particle statistics. Since the Feshbach molecules can be considered as a coherent mixture of an atom pair and a molecular state, their size is rather large and becomes largest at the resonance. The intermolecular scattering length was determined to be $a_m = 0.6a$ [87]. Feshbach molecules are stable as they neither do dissociate by collisions, nor do they relax into deeply bound molecules. For strong interactions, the critical temperature of the phase transition to a molecular Bose-Einstein condensate scales with the Fermi energy like $T_{\mathrm{C}} \simeq 0.55\,E_{\mathrm{F}}/k_{\mathrm{B}}$, and was observed for the first time in 2003 [50, 51, 52].

BCS limit

On the right hand side of the Feshbach resonance (see Fig. 2.3), weak interactions can induce a phase transition into a superfluid state of the fermionic system which corresponds to the famous BCS state, first introduced by Bardeen, Cooper and Schrieffer to describe superconductivity in metals. In general, the BCS theory describes a fermionic system with weak attractive interactions, where the mean distance between interacting particles is much larger than the interparticle spacing. Since the Fermi sea is unstable against the weakest attractive interactions, the system prefers to form so-called Cooper pairs with exponentially small binding energy, which effectively decreases the total energy. Here, the pairing takes place between two atoms of opposite momentum and spin at the Fermi surface. It is important to note that the pairing in the BCS regime is a true many-body effect in contrast to the two-body nature of the pairing in the BEC regime. This is also reflected in the size of the corresponding pairs. While the size of Feshbach molecules is small compared to the typical interparticle spacing, Cooper pairs are spatially overlapped because their size greatly exceeds the interparticle separation. The Cooper pairing mechanism is related to an energy gap Δ_{gap} in the superfluid single-particle excitation spectrum, which is given by

$$\Delta_{gap} = \frac{8}{e^2} E_{\mathrm{F}} e^{-\pi/(2k_{\mathrm{F}}|a|)}\,. \tag{2.13}$$

The Fermi gas exhibits frictionless flow below the critical temperature T_C of the superfluid phase transition which is proportional to the gap Δ_{gap}. In the regime of weak interactions $k_\mathrm{F}|a| \ll 1$, it reads

$$T_\mathrm{C} \approx 0.277\, T_\mathrm{F}\, e^{-\pi/(2k_\mathrm{F}|a|)} \tag{2.14}$$

Above the critical temperature, we find a normal phase that corresponds to a weakly interacting Fermi liquid with gapless excitations. For realistic values of $k_\mathrm{F}|a|$, the transition temperature quickly becomes very small (see Fig. 2.4), making the observation of the true BCS state with atomic quantum gases at weak interactions rather difficult. However, the observation of a vortex lattice in a strongly interacting, rotating Fermi gas provided clear evidence for superfluidity in the crossover regime for $1/k_\mathrm{F}\,|a| \ll -1$ [61]. In this regime, the pairing gap has been measured for different interaction parameters $1/k_\mathrm{F}\,a$ [57, 60].

Unitarity regime

In the vicinity of the resonance for $1/k_\mathrm{F}|a| \ll 1$, the s-wave scattering length a between two colliding fermions diverges. In this situation, the strongly interacting Fermi gas is limited by unitarity which means that the Fermi energy E_F and $1/k_\mathrm{F}$ remain the only relevant energy and length scales of the system. Under these conditions, an ultracold atomic Fermi gas acquires universal properties which can also be found in other strongly interacting Fermi gases such as neutron stars or atomic nuclei. Unitarity implies a simple scaling behavior of physical quantities with respect to the non-interacting Fermi gas at zero-temperature. For instance, the chemical potential for a unitarity limited gas is then given by $\mu = (1+\beta)E_\mathrm{F}$, and the mass of the atoms m can be replaced by the effective mass $m_\mathrm{eff} = (1+\beta)^{-1}m$. In a similar way, the density profile of a universal Fermi gas is well described by a re-scaled Thomas-Fermi profile with a size reduced by a factor $(1+\beta)^{1/4}$. The universal scaling parameter β is constantly being refined, both by theoretical calculations based on Monte-Carlo methods ($\beta = -0.56(1)$ and $\beta = -0.58(1)$) as well as by experimental measurements on ^{6}Li and ^{40}K. For finite, non-zero temperatures, the Fermi gas in the unitarity regime obeys universal thermodynamics, which currently is also studied with great interest in experiments and theory [68, 69, 70, 71]. The nature of the atom pairs in the unitarity regime neither corresponds to pure Feshbach molecules nor to Cooper pairing. One may consider them as generalized molecules, stabilized by many-body effects, or vice versa as generalized Cooper pairs. Their binding energy is of the order of the Fermi energy, and the size of the constituent fermions is comparable to the interparticle spacing [60]. This leads to a very exciting aspect of the unitarity regime, namely the fact that the critical temperature T_C for superfluidity is very high, of the order of $(0.15-0.2)E_\mathrm{F}/k_\mathrm{B}$. The ground state at $T=0$ is a superfluid of pairs, a so-called resonance superfluid. The zero-temperature ground state stays superfluid over the entire crossover, from the BEC into the BCS regime. In the normal phase above the critical temperature, the unitary gas remains strongly interacting. According to conventional BCS theory, pair formation and condensation usually coincide in superfluid Fermi systems. However, a very recent experiment [67] could provide evidence for an energy gap in the dispersion relation for a small range above T_C. This so-called pseudogap implies pairing above the condensation temperature, owing to persisting pair correlations in the system, which is not present in conventional BCS superfluids.

In summary, Fig. 2.4 illustrates the phase diagram of an interacting two-component Fermi gas in the crossover between Bose-Einstein condensation and Bardeen Cooper Schrieffer superfluidity [88]. Following the previous discussion, the diagram schematically shows the evolution of the normal and superfluid phase as a function of the interaction parameter $1/k_\mathrm{F}\, a$ and the relative temperature T/T_F.

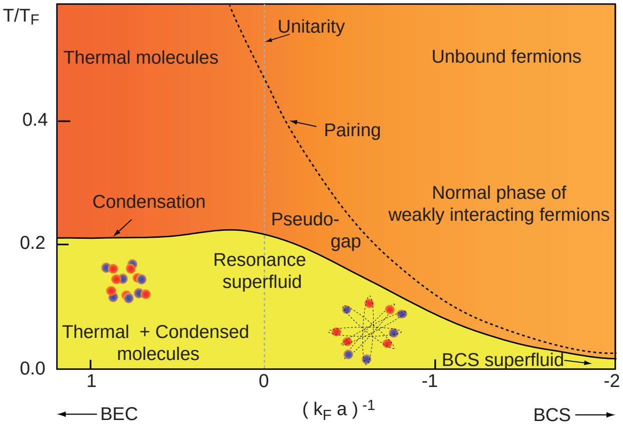
T/T_F
0.4
0.2
0.0
Thermal molecules
Unitarity
Unbound fermions
Pairing
Condensation
Pseudo-
gap
Normal phase of
weakly interacting fermions
Resonance
superfluid
Thermal + Condensed
molecules
BCS superfluid
1
0
-1
-2
BEC
(k_F a) -1
BCS

Fig. 2.4: Phase diagram of the BEC to BCS crossover as a function of the interaction parameter $(k_\mathrm{F}\, a)^{-1}$ and the relative temperature T/T_F based on [88]. Below a critical temperature the Fermi system shows superfluid pairing (yellow region), which either can be approximated by a BEC of molecules or a BCS state of Cooper pairs. The critical temperature for the transition into a superfluid strongly depends on the interaction parameter $(k_\mathrm{F}\, a)^{-1}$ for the BCS regime, whereas in the BEC regime it is mainly dependent on the particle statistics only. In between, for $(k_\mathrm{F}\, |a|)^{-1} \ll 1$, the Fermi gas is in the strongly interacting BEC-BCS crossover regime. The ground state at $T = 0$ is often referred to as resonance superfluid. Right on resonance, the system is in the unitarity regime. Pairing occurs on the left hand side of the dashed line. For increasing $(k_\mathrm{F}\, a)^{-1}$, the pair-formation line diverges away from the critical temperature. At unitarity, a pairing pseudo gap is expected in between both lines, which implies pairing above the condensation temperature.

Spin imbalance

The two-dimensional phase diagram in Fig. 2.4 can be extended along a third axis, which measures the population imbalance of the two components in a spin-mixture Fermi gas, i.e. the polarization. Exploring imbalance effects of the spin degree of freedom states another unique property of ultracold Fermi gases, which for example is nearly impossible in solid state superconductors due to the Meißner Ochsenfeld effect. Experiments with spin imbalanced samples of strongly interacting ^{6}Li atoms could show that superfluidity is quenched at a certain interaction dependent imbalance, even at zero temperature [63, 66]. This limit is known as the Chandadrasekhar-Clogston or Pauli paramagnetic limit of superfluidity. Moreover, these experiments revealed a phase separation between the excess fermions of the majority component from the superfluid core [63, 64]. Very recently, experimental progress towards a very exotic polarized superfluid state was achieved in a one dimensional Fermi gas [89]. This so-called FFLO state was proposed by Fulde and Ferrell [90], as well as by Larkin and Ovchinnikov [91] nearly 40 years ago. There, superfluidity is predicted to exist under imbalanced spin conditions due to the formation of pairs with finite net momentum. While in three dimensions the FFLO state is believed to occupy only a small portion of the phase diagram, FFLO correlations are expected to be pronounced in one dimension.

2.3 Quantum statistics

When the temperature of an ideal gas at a given density becomes low and the thermal deBroglie wavelength approaches the interparticle separation, the Boltzmann statistics of classical physics is no longer applicable. At this point, the quantum statistics of the constituent particles comes into play which accounts for the different occupation probabilities of quantum states depending on whether the particles are bosons or fermions. While fermions obey the Fermi-Dirac distribution and the related Pauli exclusion principle, bosons occupy the quantum states according to the Bose-Einstein distribution. In the following sections, we discuss in detail how the distinctive particle statistics of fermions are fundamentally reflected in the noise and correlation properties of an ideal Fermi gas. In particular, we shed light onto the fluctuations of the particle density, both in phase space and in real space. The textbook results of this discussion provide the necessary background to the experiments presented in chapter 6, reporting on the first real-space visualization of the Pauli exclusion principle. For this, it is convenient to recall the quantum statistical description of an ideal quantum gas, the results of which are essential for the further discussion. This short review of the grand canonical ensemble follows loosely the standard discussion as given in a variety of textbooks on statistical mechanics, e.g. [92, 74].

2.3.1 Grand canonical ensemble

The quantum statistics of an ideal quantum gas, i.e. a quantum gas without interactions between the constituents, is most conveniently described in the grand canonical ensemble since this is the only ensemble allowing to exactly derive the Fermi-Dirac and Bose distributions. A Hamiltonian describing a system of N non-interacting particles confined in some potential $V(\boldsymbol{r})$ can be solved in a basis system of N-particle states $|p_1, p_2, ..., p_N\rangle$. Each of these states consists of products of the corresponding single-particle states $|p\rangle$ with eigen-energy ϵ_p that are fully characterized by the quantum number p:

$$|p_1, p_2, ..., p_N\rangle = \aleph \sum_P (\pm 1)^P P |p_1\rangle ... |p_N\rangle \, . \tag{2.15}$$

Here, $\sum_P$ symbolizes a sum over all permutations P of the numbers 1 to N. The scaling factor $\aleph$ reads $\frac{1}{\sqrt{N!}}$ for fermions, respectively $(N! n_{p1}! n_{p2}! ...)^{-1/2}$ for bosons. The total particle number N results from the sum of the occupation numbers n_p of all single-particle states $|p\rangle$ as $N = \sum_p n_p$. The further discussion will be restricted to fermions only to which this thesis is devoted. The partition function Z_G for an ideal gas in the grand canonical ensemble is given by

$$Z_G \equiv \prod_p \sum_{n_p} z^{n_p} e^{-\beta \epsilon_p n_p} = \prod_p \left(1 + z e^{-\beta \epsilon_p}\right) \, , \tag{2.16}$$

where z and β denote Lagrange multipliers which can be identified as $\beta = (k_\mathrm{B} T)^{-1}$, and z to be the fugacity. In analogy to classical statistical mechanics, the grand canonical potential Φ is defined as

$$\Phi = -\beta^{-1} \log Z_G = \sum_{\{n_p\}} n_p e^{-\beta \sum_p n_p (\epsilon_p - \mu)} = -\beta^{-1} \sum_p \log \left(1 + z e^{-\beta \epsilon_p}\right) \, . \tag{2.17}$$

From the grand canonical potential the average total number of particles and also the equation of state can be deduced:

$$\langle N \rangle \equiv N \equiv - \left(\frac{\partial \Phi}{\partial \mu}\right)_\beta = z \frac{\partial}{\partial z} \log Z_G = \sum_p n(\epsilon_p) \, , \tag{2.18}$$

$$\frac{PV}{k_\mathrm{B} T} = \log Z_G = \sum_p \log \left(1 + z e^{-\beta \epsilon_p}\right) \, . \tag{2.19}$$

Here, the occupation number $n(\epsilon_p)$ is equal to the mean occupation number of state $|p\rangle$ and corresponds for fermions to the well-known Fermi-Dirac distribution given in equation (2.1)

$$n(\epsilon_p) \equiv \frac{1}{z^{-1} e^{\beta \epsilon_p} + 1} \, . \tag{2.20}$$

Equation (2.18) in combination with the definition (2.20) determines the fugacity z.

For large confining volumes V, i.e. $V \to \infty$, the sum over different states $\sum_p ...$ in the above expressions can be replaced by the integral over p, normalized by an appropriate scaling factor in front of the integral $\frac{V}{(2\pi\hbar)^3} \int ....dp$. Doing so, we again obtain the equation of state in the grand canonical ensemble

$$\frac{P}{k_{\mathrm{B}}T} = \frac{4\pi}{h^3} \int_0^\infty dp\, p^2 \log(1 + ze^{-\beta\epsilon_p}) = \frac{1}{\lambda^3} f_{5/2}(z)\,, \tag{2.21}$$

and the average particle density $v = V/N$

$$\frac{1}{v} = \frac{4\pi}{h^3} \int_0^\infty dp\, p^2 \frac{1}{z^{-1}e^{\beta\epsilon_p} + 1} = \frac{1}{\lambda^3} f_{3/2}(z)\,, \tag{2.22}$$

where $\lambda = \sqrt{2\pi\hbar^2/mk_{\mathrm{B}}T}$ is the thermal deBroglie wavelength. The last transformation in each of the equations (2.21) and (2.22) results from the definition of the generalized Riemann ζ-function, which hence allows us to rewrite the function $f_{x/2}$ as series expansion of z:

$$f_{x/2}(z) = \sum_{l=1}^{\infty} \frac{(-1)^{l+1} z^l}{l^{x/2}}\,. \tag{2.23}$$

From the average particle density $\langle N \rangle / V$ as defined in (2.22), we finally deduce the average particle number (2.18) as

$$\langle N \rangle = \frac{4\pi V}{h^3} \int_0^\infty dp\, p^2 \frac{ze^{-\beta\epsilon_p}}{ze^{-\beta\epsilon_p} + 1}\,. \tag{2.24}$$

2.4 Density fluctuations

Hitherto, the discussion on quantum gases and quantum statistics has been carried out in the grand canonical ensemble. In general, this ensemble describes a system with constant chemical potential μ, volume V and temperature T, but accounts for variations of the internal energy E and the particle number N via an energy and particle exchange with a surrounding bath. Hence, a finite-size system in thermal equilibrium with its surrounding shows characteristic fluctuations of the particle number and thus the density. These density fluctuations are the subject of investigation in the following discussion and also in the experimental chapter 6 on the local observation of antibunching in a trapped Fermi gas [93].

2.4.1 Fluctuations in phase space

Noise in a quantum system, i.e. the specific fluctuations in a physical observable, is fundamentally governed by quantum statistics and the many-body state of the underlying particles. In order to understand the specific relationship between the particle statistics and density fluctuations of the constituent particles in an ideal gas, we focus on the fluctuations in the occupation numbers of the (quantum) states n_p at first, i.e. we study density fluctuations in phase space.

Distinguishable particles

We first consider a Boltzmann gas of distinguishable particles. According to the formalism of particle statistics discussed in the previous section, the mean occupation number of a state q with energy ϵ_q is defined as the derivative of the grand canonical potential Φ with respect to the energy ϵ_q. With the grand canonical potential of the ideal classical gas,

$$\Phi = -\beta^{-1} \sum_p z e^{-\beta \epsilon_p} , \tag{2.25}$$

we calculate the mean occupation number of a single phase space cell, characterized by the quantum number q,

$$\langle n_q \rangle = \frac{\partial \Phi}{\partial \epsilon_q} = z e^{-\beta \epsilon_q} . \tag{2.26}$$

The second derivative of the grand canonical potential with respect to the energy ϵ_q yields the variance of n_q as

$$\frac{\partial^2 \Phi}{\partial \epsilon_q^2} = -\beta \left(\langle n_q^2 \rangle - \langle n_q \rangle^2 \right) \equiv -\beta (\Delta n_q)^2 , \tag{2.27}$$

and thus the fluctuations of the particle number in state q are given by

$$(\Delta n_q)^2 = -\beta^{-1} \frac{\partial \langle n_q \rangle}{\partial \epsilon_q} = \langle n_q \rangle . \tag{2.28}$$

The notation $\langle \cdot \rangle$ represents the statistical mean of a quantity which results from a large number of independent realizations, or, from an experimental point of view, from repeated measurements. Note that for statistically independent particles with negligible interactions the variance of particles observed in a single phase space cell is equal to the number of particles expected on average. This linear relation between the variance and mean of the particle number is conventionally denoted as classical shot noise or also Poissonian noise.

Indistinguishable particles

As soon as the thermal deBroglie wavelength approaches the interparticle separation at sufficiently low temperatures, the particles become indistinguishable and thus subject to quantum mechanical exchange symmetry. Applying the same derivation for the mean and variances of the particle numbers onto an ideal Fermi gas, the counting statistics of fermions (2.20) now has to be accounted for. For a specific phase space state labeled by the quantum number q, we obtain the mean number of occupying particles via

$$\frac{\partial \Phi}{\partial \epsilon_q} = \frac{\sum_{\{n_p\}} n_q e^{-\beta \sum_p n_p(\epsilon_p - \mu)}}{\sum_{\{n_p\}} e^{-\beta \sum_p n_p(\epsilon_p - \mu)}} = \langle n_q \rangle \, , \tag{2.29}$$

and subsequently the variance as

$$(\Delta n_q)^2 = -\beta^{-1} \frac{\partial \langle n_q \rangle}{\partial \epsilon_q} = \frac{z^{-1} e^{-\beta \epsilon_p}}{(z^{-1} e^{-\beta \epsilon_p} + 1)^2} = \langle n_q \rangle - \langle n_q \rangle^2 \, . \tag{2.30}$$

We find that for the ideal Fermi gas the fluctuations of the particle numbers per phase space cell are reduced below the classical shot noise level. The reduction of the variance for fermions is a direct consequence of the Pauli exclusion principle, which inhibits two identical fermionic particles to occupy the same quantum state and leads to the effect which commonly is denoted as antibunching in literature. In a certain way, one can think of the Pauli principle as giving rise to an interparticle "repulsion", which increases the energy cost for large particle fluctuations. At this point, it is important to note that the sub-Poissonian nature of particle fluctuations in an ideal Fermi gas is a pure quantum mechanical effect, which has no classical analogue. In contrast, the equivalent expression of (2.30) for the particle fluctuations in an ideal Bose gas reads $(\Delta n_q)^2 = \langle n_q \rangle + \langle n_q \rangle^2$. Statistically, bosons are more likely found to occupy a single phase cell than to be spread over several states and thus tend to bunch. However, bunching of bosons can be explained within a classical field description with fluctuating phases, and thus does not require any quantum mechanical argumentation.

Equations (2.26) to (2.30) predict the results for the mean particle number and its variance in a probe volume of $\hbar^3$ containing only a single phase space cell. In phase space, the mean and fluctuations of different cells are statistically independent of each other. Therefore, the summation over a group of Z neighboring states $\{n_k\}$ containing all together $N = \sum n_k$ particles allows us to calculate the mean and variance in a probe volume larger than the single phase space cell. For the classical gas, the individual values of the mean and variance merely add up and the total variance is given by

$$(\Delta N)^2_{Boltzmann} = Z \cdot \langle n \rangle = \langle N \rangle \tag{2.31}$$

For the ideal Fermi gas, the particle fluctuations contained in Z phase space cells follows from $(\Delta N)^2 = \sum \langle n_k^2 \rangle - \langle n_k \rangle^2 = \sum \langle n_k \rangle - \sum \langle n_k \rangle^2$. Given the case, where all phase space cells are occupied by same number $\langle n_k \rangle$ on average, the last equation can be simplified to

$$(\Delta N)^2_{Fermi} = \langle N \rangle - \frac{\langle N \rangle^2}{Z} \, . \tag{2.32}$$

In a realistic experiment, the number of phase space cells occupied by the probe volume, $Z = (\Delta x \, \Delta y \, \Delta z)\,(\Delta p_x \, \Delta p_y \, \Delta p_z)/\hbar^3$, might be very large which suppresses the N^2 term. In order to observe such reduced fluctuations, low temperatures are essential because this reduces the size of $(\Delta p_x \, \Delta p_y \, \Delta p_z)$. In addition, high densities are also favorable, making the N^2 term to enhance itself. Low temperatures and high densities mean a high occupation of individual phase space cells and thus approaching quantum degeneracy. Hence, the effect of antibunching only becomes observable below this fundamental threshold when particles lose their distinctness. In those regions of the phase space volume with unity occupation , i.e. at zero temperature, fluctuations in a Fermi gas even vanish completely.

In contrast, bosons show enhanced fluctuations, scaling like $(\Delta N)^2_{Boson} = \langle N \rangle + \frac{\langle N \rangle^2}{Z}$. This relation was already shown by Albert Einstein in 1909, when he first derived a similar expression for the fluctuation of the energy of black-body radiation in a given frequency interval. Later, he implicated these findings into the theory of the ideal quantum gas in 1925.

Experimental background

Since that time, the effects of bunching and antibunching have been demonstrated experimentally in various systems. The bunching of thermal photons was already verified in 1956 by R. Hanbury Brown and R.Q. Twiss in a famous experiment, commonly named after their last names as Hanbury Brown-Twiss (HBT) experiment [17]. In this experiment, an interferometer was aimed at the star Sirius and the incident photons were collected on two detectors. Due to bunching, the two intensity distributions showed a positive correlation. Later, the super-Poissonian statistics of bosons was also measured in cold atomic system. In 1996, positive density correlations were found by M. Yasuda and F. Shimizu in the first measurement of the auto-correlation function of massive particles. This study was performed on an atomic beam of Neon atoms [94]. More recently, A. Öttl and collaborators in the group of T. Esslinger investigated the counting statistics of an atom laser beam, formed by continuously output coupling atoms from a Bose-Einstein condensate. They probed the second order correlation function and found Poissonian statistics for the mono-energetic atom laser and Bose distributed counting statistics for a pseudo-thermal atomic beam, respectively [18]. Also in 2005, the group of I. Bloch found evidence for positive quantum noise correlations [19] in an expanding cloud of ultracold ^{87}Rb atoms emerging from the Mott insulating phase [95] in an optical lattice. In a similar experiment, the same group was able to study the effect of antibunching in the anti-correlation revealed by a fermionic system of ultracold ^{40}K atoms also confined in an optical lattice [20]. Combining both in one experiment, Jeltes et al. drew a comparison of the Hanbury Brown–Twiss effect [96] for bosons and fermions with metastable Helium (^{4}He and ^{3}He). Moreover, antibunching of fermions also appears in solid state systems and could be reported for electrons, both for a two-dimensional electron gas in the quantum Hall regime [97] as well as in an interferometric experiment with a mesoscopic electron beam splitter device [98].

2.4.2 Fluctuations in real space

All experiments cited in the previous paragraph jointly base on the measurement of the second order correlation function $g^{(2)}(\boldsymbol{r}, \boldsymbol{r'})$ in different variations of Hanbury Brown-Twiss-like experiments. There, the observed effects of bunching and antibunching occur as a result of the constructive or destructive interference of the possible propagation paths that two particles can choose to reach the detector. This interferometric approach intrinsically probes particle correlations in the momentum space. However, the effects of bunching and antibunching also manifest themselves in real space, namely in enhanced and suppressed density fluctuations for bosons and fermions, respectively. We derive this in the following section. Indeed, enhanced density fluctuations have been observed in a quasi one-dimensional Bose-Einstein condensate of ^{87}Rb atoms on an atom chip [26]. Yet, a direct observation of reduced density fluctuations for fermions in real space has not been reported. The following sections treat this relation between the particle statistics, i.e. Fermi and Boltzmann counting statistics, and the density of an ideal gas.

Density fluctuations of an ideal classical gas

The density fluctuations of the ideal classical gas of distinguishable and statistically independent particles can be readily calculated from its Poissonian statistics. Suppose we probe a small subvolume V of an ideal classical gas which is in thermal equilibrium with its surrounding. The probability p_N to find N particles in this subvolume V is given by a binomial distribution

$$p_N = \frac{N_{\text{tot}}!}{N!(N_{\text{tot}} - N)!} \left(\frac{\langle N \rangle}{N_{\text{tot}}}\right)^N \left(1 - \frac{\langle N \rangle}{N_{\text{tot}}}\right)^{N_{\text{tot}} - N} . \tag{2.33}$$

Here, N_{tot} corresponds to the total number of particles in the gas, whereas $\langle N \rangle$ denotes the mean number of particles in the subvolume V. For a large system containing a large number of particles N_{tot}, the binomial function can be approximated by a Poissonian distribution

$$p_N = \frac{\langle N \rangle^N e^{-\langle N \rangle}}{N!} . \tag{2.34}$$

For this Poissonian statistics, the variance of the particle number in the observation volume V is determined by

$$(\Delta N)^2 = \langle N^2 \rangle - \langle N \rangle^2 = \sum_{N=0}^{\infty} N^2 \cdot p_N - \langle N \rangle^2 = \langle N \rangle . \tag{2.35}$$

Dividing the fluctuations of the particle number by the subvolume V yields the density fluctuations of distinguishable particles in the observation volume V

$$(\Delta n)^2_{Boltzmann} = \langle n \rangle . \tag{2.36}$$

We note that in analogy to the particle fluctuations in phase space, a Boltzmann gas also reveals a linear relation between the density fluctuations and the mean density in real space.

Density fluctuations of an ideal Fermi gas

The mean density $\langle n \rangle$ of an ideal Fermi gas in a box potential of length L and volume $V = L^3$ can be directly deduced from the quantity $1/v$ in equation (2.22) since $1/v = N/V$. Taking the derivative of this equation with respect to the fugacity z, we obtain the variance of the density, i.e. the density fluctuations:

$$\langle n \rangle = \frac{4\pi}{h^3} \int_0^\infty dp\, p^2 \frac{z e^{-\beta\epsilon_p}}{z e^{-\beta\epsilon_p} + 1} = \frac{1}{\lambda^3} f_{3/2}(z)\,, \tag{2.37}$$

and

$$\begin{aligned} (\Delta n)^2_{Fermi} &= \langle n^2 \rangle - \langle n \rangle^2 = z\frac{\partial}{\partial z}\langle n \rangle = \frac{1}{\lambda^3} f_{1/2}(z) && (2.38) \\ &= \frac{4\pi}{h^3} \int_0^\infty dp\, p^2 \frac{z e^{-\beta\epsilon_p}}{z e^{-\beta\epsilon_p} + 1} - \frac{4\pi}{h^3} \int_0^\infty dp\, p^2 \frac{(z e^{-\beta\epsilon_p})^2}{(z e^{-\beta\epsilon_p} + 1)^2} \\ &= \langle n \rangle - \frac{4\pi}{h^3} \int_0^\infty dp\, p^2 \left(\frac{z e^{-\beta\epsilon_p}}{z e^{-\beta\epsilon_p} + 1} \right)^2 . && (2.39) \end{aligned}$$

The density fluctuations of an ideal Fermi gas comprise two contributions: the first term which is identical to the mean density, and the second term which strongly depends on the temperature. Referring to equations (2.39) and (2.36), the second term leads to a deviation from the linear scaling of the classical gas. Thus, the quantum statistics of fermions leads to reduced density fluctuations in a Fermi gas, which is a direct manifestation of antibunching in real space. The reduction of density fluctuations is a pure consequence of quantum mechanics without any classical analogue, and only due to the anti-symmetrization of the wave function for fermions.

Fluctuations at low density and high temperature

This effect is even present - at least formally - in the limit of high temperatures and low densities, i.e. for $z \ll 1$, when the Fermi gas approaches the classical limit of a Boltzmann gas. There, all thermodynamic functions reduce to those of a classical ideal gas plus small corrections caused by the Pauli principle. For small fugacities $z \ll 1$, we use the series expansion (2.23) of the generalized $f_{3/2}$-function to expand the density (2.22) as a power law of the fugacity z:

$$\frac{\lambda^3}{v} = z - \frac{z^2}{2^{3/2}} + \mathcal{O}(z^3)\,. \tag{2.40}$$

The density fluctuations result again from $(\Delta n)^2_{Fermi} = \langle n^2 \rangle - \langle n \rangle^2 = z\frac{\partial}{\partial z}\langle n \rangle$. By solving equation (2.40) to give z as a function of v, the density fluctuations $(\Delta n)^2_{Fermi}$ can be re-written as a power law of the mean density $\langle n \rangle$

$$(\Delta n)^2_{Fermi} = \langle n \rangle - \frac{\lambda^3}{2^{3/2}}\langle n \rangle^2 + \mathcal{O}\left(\langle n \rangle^3\right) . \tag{2.41}$$

For small fugacities, the Fermi gas is in a regime where $\lambda^3/v \ll 1$, which implies that the thermal deBroglie wavelength $\lambda = \sqrt{2\pi\hbar^2/mk_\mathrm{B}T}$ is much smaller than the interparticle separation $v^{1/3}$. Therefore, the quantum effect of reduced density fluctuations is expected to be negligible. In contrast, quantum effects become noticeable as soon as the thermal deBroglie reaches the interparticle separation, hence when approaching quantum degeneracy at low temperatures and high densities. Fig. 2.5 visualizes the appearance of reduced density fluctuations in real space. There, a sample of a two-dimensional Fermi gas is considered at two different temperatures, but with equal density in both cases.

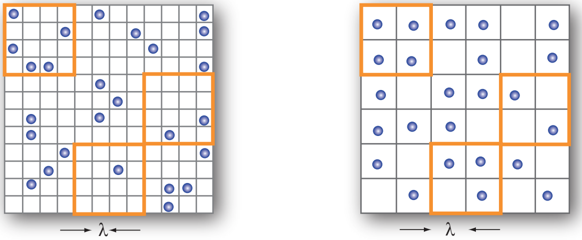

Fig. 2.5: Reduced density fluctuations in real space: Decreasing temperatures imply an increase of the deBroglie wavelength. For each particle, this length scale is associated to its uncertainty in position, represented by the cells of length λ in both panels of this figure. The left one shows the spatial distribution of particles in a classical gas. There, the average distance between the particles, which are randomly distributed, is much larger than λ. The orange box indicates the size of the observation volume. Evaluating the statistics of particles in different observation volumes, no effect of the fermionic nature of the particles is apparent since mean and variance are approximately the same. In contrast, at sufficient low temperatures (right panel), λ becomes of the order of the interparticle separation. Here, the variance of particles numbers over different observation volumes is significantly reduced revealing a direct signature of antibunching in real space.

2.4.3 Density fluctuations in an ultracold Fermi gas of ^{6}Li

So far, we mainly considered the textbook example of an ideal gas in a box potential of length L and volume $V = L^3$. In this section, we investigate the appearance of density fluctuations in the real situation of our experiments: a dilute quantum gas of ultracold ^{6}Li atoms confined in an optical dipole trap. The trapping potential $V(\boldsymbol{r})$ is given by the Gaussian intensity profile of the laser beam which creates the trap.

In this case, the spatial density distribution of the quantum gas is well described by equation (2.7) in general. For simplicity, the Gaussian potential is approximated by a harmonic oscillator potential as given in equation (2.3). The only missing quantity is the chemical potential μ, which is an implicit function of the relative temperature T/T_F. However, for $T \ll T_\mathrm{F}$, the chemical potential is well approximated by the Sommerfeld expansion

$$\mu(T) = E_\mathrm{F}\left(1 - \frac{\pi^2}{3}\left(\frac{T}{T_\mathrm{F}}\right)^2\right) . \tag{2.42}$$

According to this, the spatial density profile can be qualitatively understood in terms of the local density approximation (LDA) which assigns to each point in the cloud a local chemical potential $\mu(\boldsymbol{r})$ defined as

$$\mu(\boldsymbol{r}) = \mu_0 - V(\boldsymbol{r}) . \tag{2.43}$$

Here, μ_0 is the chemical potential which corresponds to the Fermi energy E_F. In order to apply the local density approximation to a bulk system of ultracold fermions in a harmonic trap, the condition of validity requires that the Fermi temperature is much larger than the harmonic oscillator energies $k_\mathrm{B}T_\mathrm{F} \gg \hbar\omega_i$. This condition is reasonably fulfilled for ultracold atoms in optical dipole traps. Hence, the fugacity $z = e^{\beta\mu}$ also becomes a local quantity $z(\boldsymbol{r}) = e^{\beta(\mu_0 - V(\boldsymbol{r}))}$. For a known trapping potential, the mean density profile is fully characterized, and we can determine the spatial distribution of the density fluctuations via (2.39)

$$k_\mathrm{B}T\frac{\partial}{\partial\mu}\langle n\rangle = \langle n\rangle - \frac{4\pi}{h^3}\int_0^\infty dp\left(\frac{p}{e^{-\beta\mu(\boldsymbol{r})}e^{\beta p^2/2m} + 1}\right)^2 . \tag{2.44}$$

With the substitution $\widetilde{p} = p/\sqrt{2m\,k_\mathrm{B}T}$ the last equation turns into

$$k_\mathrm{B}T\left(\frac{\partial\mu(\boldsymbol{r})}{\partial x}\right)^{-1}\frac{\partial\langle n\rangle}{\partial x} = \langle n\rangle - \frac{4\pi}{\sqrt{\pi}\lambda^3}\int_0^\infty d\widetilde{p}\left(\frac{\widetilde{p}}{z^{-1}(\boldsymbol{r})e^{\widetilde{p}^2} + 1}\right)^2 . \tag{2.45}$$

In Fig. 2.6 we show simulated data of the mean density and density fluctuations of a trapped Fermi gas. The simulation describes an ensemble of ^{6}Li atoms confined in an anisotropic harmonic oscillator potential with trapping frequencies of $\omega_x = \omega_y = 2\pi\times 400\,\mathrm{Hz}$ and $\omega_z = 2\pi\times 25\,\mathrm{Hz}$. We assume a Fermi energy of $E_\mathrm{F} = k_\mathrm{B}\,T_\mathrm{F} = k_\mathrm{B}\times 500\,\mathrm{nK} \simeq h\times 10\,\mathrm{kHz}$ and a temperature of $T = 100\,\mathrm{nK}$. For these parameters, the local density approximation is well justified. Fig. 2.6(a) presents the spatial profiles of the mean density (black solid line) and the corresponding variance (black dashed line) along the radial axis for $y = 0$ and $z = 0$ at a relative temperature of $T/T_\mathrm{F} = 0.2$. While the variance profile is nearly equal to the mean profile at the wings, the variance shows a strong suppression at the center. Here, we expect the highest occupation of single quantum states on average, and therefore the effect of the Pauli principle to be

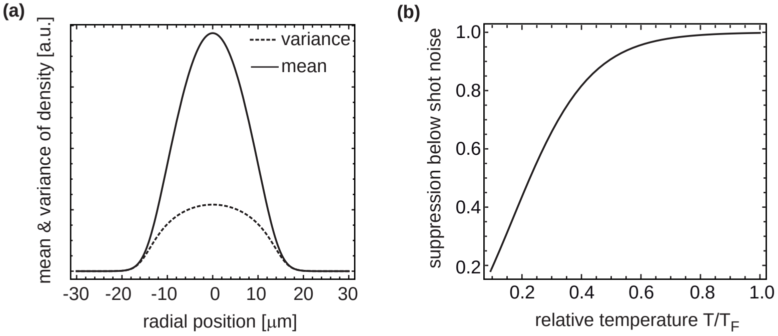

Fig. 2.6: (a) Simulated profiles of the mean density and density fluctuations in a trapped ideal Fermi gas. The data show the simulation of an ensemble of ultracold ^{6}Li atoms at $T/T_\mathrm{F} = 0.2$, trapped in a harmonic oscillator potential with cylindrical symmetry . The black solid line shows the mean density in radial direction for $y = 0$ and $z = 0$. The corresponding variance is plotted as dashed black line. (b) Suppression of fluctuations in a Fermi gas a function of the relative temperature T/T_F. The ordinate axis is defined by the ratio between the second term of equation (2.45) and the mean density, both at the center position of the cloud.

strongly pronounced leading to a clear decrease of fluctuations. The reduction of the variance is strongly dependent on the temperature and can also be interpreted as a measure of the local quantum degeneracy. The second term in equation (2.45) reveals the temperature and space dependent reduction of the fluctuations with respect to shot noise. In Fig. 2.6(b) we plot the sub-Poissonian suppression of fluctuations defined by "second term/mean density" as a function of the temperature T at the center position of the trap. Here, the chemical potential μ_0 in the LDA (2.43) has also to be scaled with the temperature according to the Sommerfeld expansion (2.42). The lower the relative temperature T/T_F, the stronger the quantum degeneracy and the larger the suppression of density fluctuations becomes.

2.5 Fluctuation-dissipation theorem

The temperature dependence of the density fluctuations can be used in the experiment to determine the temperature of the system in absolute units. In general, thermometry in a Fermi gas is delicate. The standard procedure for the temperature determination relies on the fitting of a model function to the mean density profile, either *in-situ* or after a certain time of flight. However, this has to be taken with caution since the information about the temperature is contained mainly in the wings of the distribution, but the profile of a degenerate Fermi gas hardly changes as a function of the temperature for high degeneracy.

2.5.1 Fluctuations and susceptibilities

In contrast, fluctuations of the density decrease almost linearly for low temperatures. At this point, equation (2.44) can be interpreted in terms of the fluctuation-dissipation theorem, which was established by H.B. Callen and T.A. Welton in 1951. The fluctuation-dissipation theorem (FDT) states a general concept in thermodynamic and particle statistics, that can be applied to both, classical and quantum systems. It relates the fluctuations of a given quantity to the product of the temperature and a corresponding susceptibility. In terms of linear response theory, the theorem defines a general relationship between the response (dissipation) of a system to an external disturbance on the one hand and the internal fluctuations of the system in absence of the disturbance on the other hand. Thereby, the fluctuation-dissipation theorem relies on the assumption that a system in thermodynamic equilibrium responds to a small applied force in an equivalent way as it responds to spontaneous fluctuations. These fluctuations are characterized by a specific correlation function for the relevant physical quantity in thermal equilibrium.

A prominent textbook example of the fluctuation-dissipation theorem is its application to the fluctuations of the internal energy U in a canonical ensemble with constant volume. Here, the FDT relates the fluctuations of the internal energy to a susceptibility which is identified to be the isochore specific heat $C_V = \left(\frac{\partial U}{\partial T}\right)$. In this case, the FDT is specified by $k_\mathrm{B}T\ C_V = \frac{1}{T}(\Delta U)^2$. In an analogue way, similar relationships can be deduced for other thermodynamic susceptibilities and their corresponding fluctuations, two of which are discussed in detail in the further course.

Particle number fluctuations and compressibility

The corresponding susceptibility for fluctuations of the particle number in a grand canonical ensemble is the isothermal compressibility κ_T, which is defined by

$$\kappa_T = \frac{1}{V}\left(\frac{\partial V}{\partial P}\right)_{T,N} = \frac{V}{N^2}\left(\frac{\partial N}{\partial \mu}\right)_{T,V}, \tag{2.46}$$

where an appropriate Maxwell relation has been used for the last transformation [74]. By definition, $\left(\frac{\partial N}{\partial \mu}\right)_{T,V} = \beta(\Delta N)^2$, and hence the fluctuation dissipation theorem for fluctuating particle numbers reads

$$k_\mathrm{B}T\frac{\partial\langle N\rangle}{\partial\mu} = (\Delta N)^2\,. \tag{2.47}$$

Applying the local density approximation, the compressibility also becomes a locally defined quantity, $\frac{\partial\langle N\rangle}{\partial\mu} = \frac{\partial\langle N\rangle}{\partial r}\left(\frac{\partial\mu}{\partial r}\right)^{-1}$. Experimentally, it is possible to determine the compressibility $\frac{\partial\langle N\rangle}{\partial\mu}$ directly from the density profile via the spatial derivative [27]. In chapter 6, we demonstrate the *in-situ* measurement of the mean and variance of particle numbers in a non-interacting Fermi gas. Referring to equation (2.47), the ratio of the measured mean and variance density profiles provides a universal measurement of the temperature, which circumvents the disadvantages of the model-dependent fitting procedure, but only relies on the exact knowledge of the trapping potential to apply the local density approximation. This fluctuation-based thermometry will also be presented in chapter 6.

So far, the previous discussion of quantum statistics and fluctuations has only been related to single-component Fermi gases. However, in our experiments we typically work with an incoherent spin mixture of the two lowest hyperfine sub-states of ^{6}Li. In the absence of interactions between the two spin states, the fluctuation-dissipation theorem for fluctuations of the particle number applies to each spin component independently.

Spin fluctuations and magnetic susceptibility

Including strong interactions, a two-component gas of ultracold atoms offers unique opportunities for the realization of strongly correlated quantum systems and especially a wide class of spin Hamiltonians. An important thermodynamic quantity for the characterization of a two component quantum gas is the magnetic susceptibility χ_{mag} as it provides clear signatures for the onset of pairing or of magnetic ordering. In linear response theory, the magnetic susceptibility states a response function of a system which implicates specific fluctuations in the relative density of the two spin components $(n_\uparrow - n_\downarrow)$. Both quantities are related by a corresponding fluctuation-dissipation theorem [16]

$$\frac{k_{\mathrm{B}} T \chi_{\mathrm{mag}}(T)}{n} = \frac{\big(\Delta(N_\uparrow - N_\downarrow)\big)^2}{N} \tag{2.48}$$

Here, n is the density of the sample and $N_\uparrow$ and $N_\downarrow$ are the numbers of fermions in the two spins states denoted by $|\uparrow\rangle$ and $|\downarrow\rangle$, respectively. Both add up to the total atom number $N = N_\uparrow + N_\downarrow$. Very recently, relation (2.48) has been employed to determine the magnetic susceptibility from the measured fluctuations in the relative density of a two-component Fermi gas along the BEC-BCS crossover [99].

2.5.2 Fluctuations and correlations

In the framework of the fluctuation-dissipation theorem, fluctuations are characterized by correlations. In that sense, the right hand side of equation (2.39) can be expressed in terms of the density correlation function $\langle\widehat{n}(\boldsymbol{r})\widehat{n}(\boldsymbol{r}')\rangle$ as shown in [100]

$$\begin{aligned} (\Delta n)^2(\boldsymbol{r}) \quad &= \quad k_{\mathrm{B}} T \frac{\partial}{\partial \mu} \langle \widehat{n}(\boldsymbol{r}, T, \mu)\rangle = \frac{\mathrm{Tr}\ \widehat{n}(\boldsymbol{r}) e^{-\beta(\widehat{p^2}/2m + \widehat{V} - \mu\widehat{N})}}{\mathrm{Tr}\ e^{-\beta(\widehat{p^2}/2m + \widehat{V} - \mu\widehat{N})}} \\ &= \quad \int d\boldsymbol{r}'^{\,3} \left[\langle\widehat{n}(\boldsymbol{r})\widehat{n}(\boldsymbol{r}')\rangle - \langle\widehat{n}(\boldsymbol{r})\rangle\langle\widehat{n}(\boldsymbol{r}')\rangle\right] . \end{aligned} \tag{2.49}$$

According to the standard formalism of quantum mechanics in second quantization, the density operators $\widehat{n}(\boldsymbol{r})$ are defined by the field operators $\widehat{\Psi}(\boldsymbol{r})$ and $\widehat{\Psi}^\dagger(\boldsymbol{r})$ (see for example [29])

$$\widehat{\Psi}^\dagger(\boldsymbol{r}) = \sum_i \Psi_i^*(\boldsymbol{r})\,\widehat{a}_i^\dagger \qquad \text{and} \qquad \widehat{\Psi}(\boldsymbol{r}) = \sum_i \Psi_i(\boldsymbol{r})\,\widehat{a}_i\,. \tag{2.50}$$

The wave functions Ψ_i are energy eigenfunctions of the particle wave field associated with the energy level i. The operators $\widehat{a}_i$ and $\widehat{a}_i^\dagger$ annihilate or create a particle in state i, and define the particle number operator $\widehat{N}_i = \widehat{a}_i^\dagger \widehat{a}_i$. For fermions, the creation and annihilation operators obey the following anti-commutation relations: $\{\widehat{a}_j, \widehat{a}_k^\dagger\} = \delta_{jk}$ and $\{\widehat{a}_j^\dagger, \widehat{a}_k^\dagger\} = \{\widehat{a}_j, \widehat{a}_k\} = 0$. Correspondingly, the field operators $\widehat{\Psi}^\dagger(\boldsymbol{r})$ and $\widehat{\Psi}(\boldsymbol{r})$ create and annihilate a particle at position $\boldsymbol{r}$, and they also obey the anti-commutation relations $\{\widehat{\Psi}(\boldsymbol{r}), \widehat{\Psi}^\dagger(\boldsymbol{r}')\} = \delta(\boldsymbol{r} - \boldsymbol{r}')$ and $\{\widehat{\Psi}^\dagger(\boldsymbol{r}), \widehat{\Psi}^\dagger(\boldsymbol{r}')\} = \{\widehat{\Psi}(\boldsymbol{r}), \widehat{\Psi}(\boldsymbol{r}')\} = 0$. The density operator $\widehat{n}(\boldsymbol{r})$ is defined as $\widehat{n}(\boldsymbol{r}) = \widehat{\Psi}^\dagger(\boldsymbol{r})\widehat{\Psi}(\boldsymbol{r})$. We now show that for a homogeneous system equation (2.49) involves the first and second order correlation function, which by definition read

$$\begin{aligned} g^{(1)}(\boldsymbol{r} - \boldsymbol{r}') &= \langle \widehat{\Psi}^\dagger(\boldsymbol{r})\widehat{\Psi}(\boldsymbol{r}')\rangle \quad \text{and} \\ g^{(2)}(\boldsymbol{r} - \boldsymbol{r}') &= \langle \widehat{\Psi}^\dagger(\boldsymbol{r})\widehat{\Psi}^\dagger(\boldsymbol{r}')\widehat{\Psi}(\boldsymbol{r}')\widehat{\Psi}(\boldsymbol{r})\rangle \end{aligned} \tag{2.51}$$

$$\begin{aligned} &= \langle \widehat{\Psi}^\dagger(\boldsymbol{r})\widehat{\Psi}(\boldsymbol{r})\widehat{\Psi}^\dagger(\boldsymbol{r}')\widehat{\Psi}(\boldsymbol{r}')\rangle - \delta(\boldsymbol{r} - \boldsymbol{r}')\langle \widehat{\Psi}^\dagger(\boldsymbol{r})\widehat{\Psi}(\boldsymbol{r}')\rangle \\ &= \langle \widehat{n}(\boldsymbol{r})\widehat{n}(\boldsymbol{r}')\rangle - \delta(\boldsymbol{r} - \boldsymbol{r}')g^{(1)}(\boldsymbol{r} - \boldsymbol{r}')\,. \end{aligned} \tag{2.52}$$

Transforming (2.51) into (2.52), we have used the fermionic anti-commutation relation of the field operators and the definition of the first order correlation function. For a homogeneous Fermi gas of single-spin-component, non-interacting particles with total density n, the correlation functions $g^{(1)}(\boldsymbol{r} - \boldsymbol{r}')$ and $g^{(2)}(\boldsymbol{r} - \boldsymbol{r}')$ can be explicitly calculated (see for example [29]). At $T = 0$, they are determined by the following equations

$$g^{(1)}(\boldsymbol{x}) = \frac{3n}{2}\,\frac{\sin(k_\mathrm{F}x) - k_\mathrm{F}x\cos(k_\mathrm{F}x)}{(k_\mathrm{F}x)^3}\,, \tag{2.53}$$

$$g^{(2)}(\boldsymbol{x}) = n^2\left(1 - \frac{9}{(k_\mathrm{F}x)^6}\left[\sin(k_\mathrm{F}x) - k_\mathrm{F}x\cos(k_\mathrm{F}x)\right]^2\right)\,, \tag{2.54}$$

where $x = |\boldsymbol{r} - \boldsymbol{r}'|$ and $k_\mathrm{F} = (3 \cdot 2\pi n)^{1/3}$. Fig. 2.7 shows the second order correlation function $g^{(2)}(\boldsymbol{r} - \boldsymbol{r}')$, also called pair correlation function, as a function of the particle separation $|\boldsymbol{r} - \boldsymbol{r}'|$, scaled in units of the Fermi wave number k_F. Due to the Pauli principle, even non-interacting fermions of the same spin are correlated. The Pauli principle causes that two fermions with equal spin must not have the same spatial wave function, and thus they tend to avoid each other. Therefore, the pair correlation function drops down from one to zero for particle separations below k_F^{-1}. Here, the

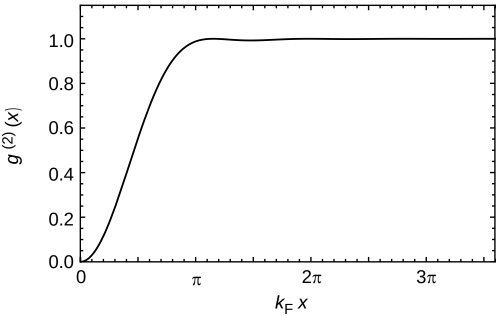

Fig. 2.7: Second order correlation function $g^{(2)}(\boldsymbol{r}-\boldsymbol{r}')$ of a homogeneous Fermi gas.

probability to find two fermions with the same spin is strongly suppressed, for which reason this region is also denoted as exchange hole.

From equation (2.52), we identify the relationship between the density correlation function $\langle\widehat{n}(\boldsymbol{r})\widehat{n}(\boldsymbol{r}')\rangle$ and the pair correlation function $g^{(2)}(\boldsymbol{r}-\boldsymbol{r}')$. The density correlations consists of two parts, the pair correlation function plus a "δ-peak" which marks the presence of a particle at zero separation. This means that the region around a single fermion is depleted for distances smaller than k_{F}^{-1}. In a non-interacting Fermi gas, it is the Pauli principle which causes the only "interaction" between the particles. This exchange interaction is only of short range ($< k_{\mathrm{F}}^{-1}$) and therefore, densities at large separations ($> k_{\mathrm{F}}^{-1}$) are uncorrelated: $\lim_{|\boldsymbol{r}-\boldsymbol{r}'|\to\infty}\langle\widehat{n}(\boldsymbol{r})\widehat{n}(\boldsymbol{r}')\rangle = \langle\widehat{n}(\boldsymbol{r})\rangle\langle\widehat{n}(\boldsymbol{r}')\rangle$. Going back to the starting point of this section, we notice that the difference within the integral over $d\boldsymbol{r}'^{\,3}$ in equation (2.49) disappears for large particle separations $|\boldsymbol{r}-\boldsymbol{r}'| > k_{\mathrm{F}}^{-1}$. In an ideal Fermi gas, only the volume of radius $R = k_{\mathrm{F}}^{-1}$ thus contains the full information about the density fluctuations at a given position $\boldsymbol{r}$. Using equation (2.52), we convert equation (2.49) into

$$\begin{aligned}(\Delta n)^2 &= \int d\boldsymbol{r}'^{\,3}\left[g^{(1)}(\boldsymbol{r}-\boldsymbol{r}')\delta(\boldsymbol{r}-\boldsymbol{r}') + g^{(2)}(\boldsymbol{r}-\boldsymbol{r}') - \langle\widehat{n}(\boldsymbol{r})\rangle\langle\widehat{n}(\boldsymbol{r}')\rangle\right] \\ &= \langle n(\boldsymbol{r})\rangle - \int d\boldsymbol{r}'^{\,3}\left[\langle\widehat{n}(\boldsymbol{r})\rangle\langle\widehat{n}(\boldsymbol{r}')\rangle - g^{(2)}(\boldsymbol{r}-\boldsymbol{r}')\right]. \qquad (2.55)\end{aligned}$$

The expression in the lower line of equation (2.55) reveals again the suppression of density fluctuations in an ideal Fermi gas with respect to a classical ideal gas. As can be shown, at $T = 0$ the area of the exchange hole corresponds to the mean density $\langle n(\boldsymbol{r})\rangle$, which implies that $\langle n(\boldsymbol{r})\rangle$ is equal to the difference of the areas under the $g^{(2)}$-function and $\langle\widehat{n}(\boldsymbol{r})\rangle\langle\widehat{n}(\boldsymbol{r}')\rangle$. Hence, fluctuations in an ideal Fermi gas at zero temperature are totally suppressed and disappear as it is also stated by the left hand side of the fluctuation-dissipation theorem, which is directly proportional to the temperature T. Qualitatively, the area under the $g^{(2)}$-function and $\langle\widehat{n}(\boldsymbol{r})\rangle\langle\widehat{n}(\boldsymbol{r'})\rangle$ assimilate as the temperature T increases and reaches the Fermi temperature. At $T = T_{\mathrm{F}}$, the integral in equation (2.55) vanishes and the density fluctuations reach the shot noise level.

3 Experimental setup

This chapter is devoted to the description of the experimental setup used for the experiments performed in the scope of this thesis. Most of the apparatus has been designed and built during the first and second year of this PhD project. The design as well as the assembly of the setup was carried out in close collaboration with my PhD predecessor Bruno Zimmermann, our project leader Dr. Henning Moritz and my PhD colleague Jakob Meineke, who joined the group after the first year. Before describing the different parts of our apparatus in detail, we will first discuss some general design considerations.

3.1 General design considerations

At the time when our project was launched, the creation of quantum degenerate Fermi gases with ultracold alkali atoms started to become a widely spread experimental technique. Only a few years ago, Bose-Einstein condensation of molecules and high temperature superfluidity in degenerate atomic Fermi gases had been demonstrated for the first time [50, 51, 52, 61]. Simultaneously, the ability to tune the interatomic interaction strength via magnetic Feshbach resonances initiated the exploration of the BEC-BCS crossover and paved the way for studying strongly correlated many-body systems in a very controlled way. Based on this former experimental progress in the research field of ultracold fermions, we wanted to reach out for a new level of control on quantum gases, namely to gain direct local access to these systems on a microscopic length scale, including optical probing as well as optical manipulation, both with very high spatial resolution. This approach was very timely as also a few other groups in the cold atom community were about to implement the ability of high-resolution imaging into their experiments [4, 5, 6, 7]. Mainly motivated by the desire for single-site resolution in optical lattice systems, all of these experiments, however, explore samples of bosonic atoms without exception, and to our knowledge, there exists no other apparatus addressing fermionic systems with high resolution yet.

For the technical development, all effort has been aimed at the design of an apparatus that combines high-resolution microscopy with well-established technologies for the preparation of a quantum degenerate Fermi gas. This objective has been accomplished by transferring an ultracold Fermi cloud into an octagonal glass cell with exceptional optical access. There, the atomic sample is sandwiched between a pair of identical, high-resolution microscope objectives, the essential tool of our experimental setup. One microscope objective is placed below the glass cell and allows local imaging of the trapped Fermi gas with a maximum resolution of 660 nm. The other microscope objective is mounted above the glass cell and represents the main component of a sophisticated optical setup that enables the generation of arbitrary optical dipole potentials on the same length scale. In the following paragraphs we will specify some of the above design considerations more precisely:

Proper isotope The group of alkali-metals in the periodic table of elements offers only two stable fermionic isotopes which are suitable for our purposes and which had already been cooled to quantum degeneracy. These are ^{6}Li and ^{40}K, both exhibiting accessible Feshbach resonances [48, 47, 101, 102]. We chose ^{6}Li for several reasons. First, it has a lower mass and thus favors faster tunneling and transport dynamics. This is preferable with respect to limited lifetimes of the cold sample and also allows larger and hence eventually spatially resolvable separations in the projected optical potential landscape. Second, technical reasons supported our choice as the availability of feasible laser sources and the recent progress in the all-optical cooling of ^{6}Li.

All optical approach In contrast to bosons, samples of fermionic atoms are by nature difficult to cool to quantum degeneracy since the Pauli principle suppresses elastic collisions between identical particles at low temperatures. There are two possibilities to circumvent this constraint. Spin-polarized Fermi gases may become quantum degenerate by sympathetic cooling in thermal contact to a cold Bose gas [103, 104]. Alternatively, one can prepare the sample in an incoherent superposition of two spin states, for which standard evaporative cooling is applicable because spin mixtures are not subject to the Pauli suppression. For the latter method, optical dipole traps are ideally suited because they intrinsically avoid conflicts which otherwise may occur by using the alternative of magnetic trapping: First, trapping of different spins is no issue for optical traps, and second, magnetic Feshbach resonances become easily applicable. Hence, we decided to follow an all-optical cooling approach which additionally allows for short experimental duty cycles [50].

Microscope setup In a fermionic system, a fundamental length scale is given by the Fermi wavelength λ_{F}, which for instance determines the interparticle distance and the scaling of density-density correlations as we have seen in the previous chapter. Probing ultracold Fermi gases on this natural length scale is one motivation aspect for the construction of our new apparatus since by this we expect to gain deeper insight into the mechanisms governing strongly correlated systems. In ultracold atomic Fermi gas, λ_{F} is typically of the order of one micrometer which sets the upper bound for the maximum resolution of the microscope system. In addition, the microscopes should desirably be deployable for at least three different wavelength: resonant light at 671 nm for imaging, red-detuned light at 761 nm to generate attractive optical dipole potentials and also blue-detuned light at 532 nm for repulsive potentials. Moreover, the construction of the apparatus, especially the opto-mechanics of the microscope setups, has to be extremely stable.

The remainder of this chapter is organized in two main parts. The first part, including sections 3.2 to 3.6, treats those components of the apparatus and experimental methods which contribute to the preparation of a quantum degenerate Fermi gas. This covers the description of the vacuum system, the laser setup, magnetic coils for the magneto-optical trap and Feshbach fields as well as the discussion of different imaging techniques. Most of these subjects, in particular the construction of the apparatus, are presented in great detail in the thesis of my PhD colleague Bruno Zimmermann [105]. Here, we restrict ourselves to a summary of the most relevant and important information. In the second part of this chapter, we addresses the experimental cycle and demonstrate the preparation of a quantum degenerate Fermi gas and a molecular Bose-Einstein condensate. The high-resolution optical system is presented in great detail in a separate chapter (see chapter 4). There, particular attention is paid to the microscope objectives and the performance of our high-resolution imaging setup. The generation of arbitrarily shaped optical micro-potentials is shown in chapter 5.

3.2 Overview of the experimental setup

We start the first part of this chapter with a general overview of the experimental setup, presenting a sketch of the cooling procedure and the vacuum system. Our experimental apparatus consists of four sections which are depicted in Fig. 3.1: the oven chamber, the Zeeman slower, the main ultra-high vacuum (UHV) chamber containing a high finesse optical resonator, and the octagonal UHV glass cell laterally attached to the main vacuum chamber.

3.2.1 Cooling strategy

Fig. 3.1 also illustrates the general cooling procedure of our experimental cycle which is similar to [50]. The cooling strategy bases on a combined procedure of laser cooling in a magneto-optical trap and a subsequent two-stage evaporative cooling process in optical dipole traps: ^{6}Li atoms emanating from an oven are decelerated by a Zeeman slower and subsequently captured in a magneto-optical trap (MOT) at the center of the main UHV chamber. In the MOT, we reach the limit of laser cooling given by the Doppler limit at some hundred micro-kelvins. We then proceed with evaporative cooling in optical traps. First, the trapped atoms are transferred into a large-volume standing-wave optical dipole trap realized by the high-finesse optical resonator inside the main vacuum chamber. This resonator trap serves as intermediate trapping potential [106], which maximizes the particle transfer from the MOT into the final trapping configuration, a tightly focused optical tweezer. After having been evaporatively pre-cooled in the resonator and finally transferred into the optical tweezer, the trapped cloud is optically moved [107] into an octagonal glass. Here, optical

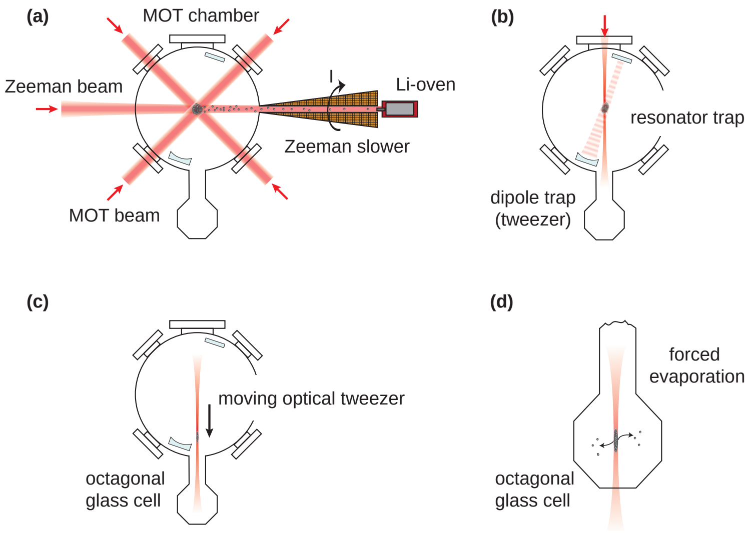

Fig. 3.1: Experimental cycle: (a) ^{6}Li atoms, emerging from the oven, are decelerated by a Zeeman slower and captured in a magneto-optical trap. (b) The trapped atoms are then transferred into a deep, large volume optical dipole trap that is created using an optical resonator. In the next step, the atoms are transferred into a tightly focussed optical tweezer. (c) By moving a lens, the atoms in the optical tweezer are transported into the octagonal glass cell which offers exceptional optical access. (d) Here, final forced evaporative cooling is performed leading to the formation of an ultracold fermionic quantum gas.

evaporation is performed by decreasing the power in the optical tweezer, resulting in the formation of an ultracold Fermi gas.

3.2.2 Vacuum system

Prerequisite for any experiment with ultracold atoms in the nano-kelvin regime is an ultra-high vacuum (UHV) environment with a background pressure of less than 10^{-11} mbar. Any contact to the 'hot' surrounding or collisions with the residual background gas reduces the lifetime of the sample and would eventually make reasonable experimentation impossible. Fig. 3.2 presents an isometric view of our apparatus. There, the above mentioned segmentation into oven, Zeeman slower, main UHV chamber and glass cell can be recognized. Vacuum-wise, our machine is separated into two sections: the main chamber with the glass cell and the vacuum pipe of the Zeeman slower on the one side, and the oven complex on the other side. At the oven-sided end of the Zeeman slower, both sections are connected by an all-metal gate valve (*VAT, Mod. 48124*, CF16) and a differential pumping stage of 145 mm length and 3 mm diameter. The valve enables a refilling of the oven without break-

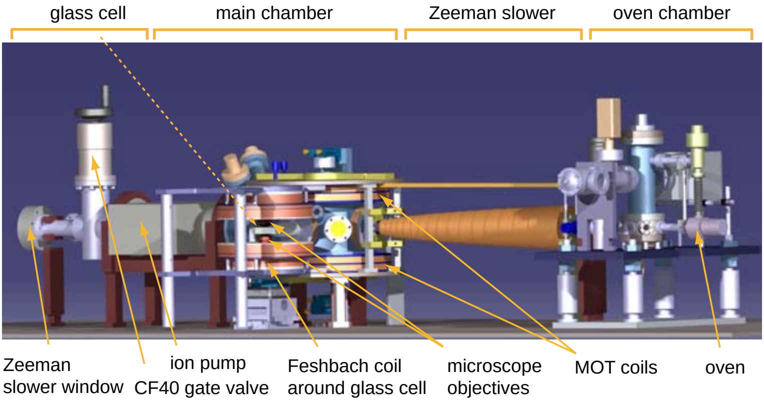

Fig. 3.2: Overview of the experimental apparatus subdivided into four sections: the oven chamber, the Zeeman slower, the main UHV chamber, and the octagonal UHV glass cell laterally attached to the main vacuum chamber. A detailed description of all parts is given in the text.

ing the vacuum in the main chamber. The differential pumping section allows to maintain ultra-high vacuum conditions ($\sim 10^{-12}$ mbar) in the main chamber, while at the same time the oven is operated at 400°C which limits the vacuum in the oven complex to $0.5 \cdot 10^{-10}$ mbar. In both vacuum sections of our apparatus, ion-getter pumps sustain the very low UHV background pressure (*Gamma Vacuum 20S TiTan DI*, 20 l/s in the oven chamber; *Gamma Vacuum 100L TiTan 30*, 100 l/s in the main chamber). In addition, we employ titanium sublimation pumps in each section to further reduce the background pressure of H_2 (Mini ball-point sublimation pump, *VARIAN, Mod. 916-0009* in the main chamber; filament *MCD MFG., 3 filaments* in the oven chamber).

Main UHV chamber

The main chamber (MOT chamber) of the apparatus is a self-designed cylindrical chamber made of electro-polished stainless steel. It offers multiple optical access through various view ports of different size as illustrated in the Fig. 3.3(b). Cooling and repumper light for the MOT (see section 3.3.3) enter the chamber through four CF40 anti-reflection coated (671 nm) view ports along the diagonals of the $x-y$-plane. The top and bottom CF200 flanges of the main chamber are specially designed, featuring a hollow-cylindrical recess for the Feshbach magnetic coils (see section 3.5). The inner core of the recess holds the view ports for the vertically MOT beams. Since for these windows anti-reflection (AR) coating was not applicable for technical reasons, we attached an AR coated substrate on top of each viewport using index matching oil as adhesive bonding. A CF63 fused-silica viewport along the y-axis provides the entrance port for the large optical dipole trap used for the transport and

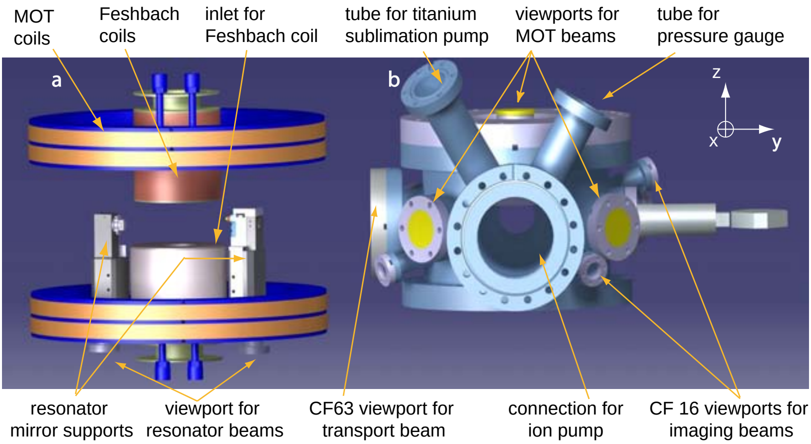
MOT coils
Feshbach coils
inlet for Feshbach coil
tube for titanium sublimation pump
viewports for MOT beams
tube for pressure gauge
a
b
z
x
y
resonator mirror supports
viewport for resonator beams
CF63 viewport for transport beam
connection for ion pump
CF 16 viewports for imaging beams

Fig. 3.3: Overview of the main chamber: (a) Inner and surrounding components of the main UHV chamber showing the setup of the optical resonator trap and solenoids for various magnetic fields used during the experimental cycle. (b) Main UHV stainless steel chamber housing the magneto-optical trap and the resonator trap. To the right, the octagonal glass cell is attached via a CF40 flange.

final evaporative cooling of the atomic sample. In addition, the main chamber exhibits two pairs of opposing CF16 view ports which are located orthogonal to each other in a skew plane (see Fig. 3.3(b)). These ports are mainly used for imaging purposes at the center of the MOT chamber. The technically most challenging component of the main vacuum chamber is the in-vacuo optical resonator, illustrated in Fig. 3.3(a). It consists of one flat and one curved high-reflection mirror (radius of curvature: 0.15 m) in hemi-spherical configuration, separated by about 15 cm. Both resonator mirrors are mounted in a corresponding rugged tower-like mechanical support, each of which is directly attached to the bottom flange of the main chamber. Light for the resonator trap enters and leaves the chamber vertically through two CF16 view ports in the bottom of the base flange and gets redirected to the resonator axis by another two mirrors in the head of the mechanical supports. More details about the resonator are given in section 3.4.1.

Octagonal glass cell

The UHV-compatible octagonal glass cell is the final science chamber for the microscopic detection and manipulation of ultracold fermions. This custom-made cuvette, which was manufactured by *Hellma® Analytics*, is laterally attached to the main chamber along the y-axis. It is made of single fused-silica plates, thermally contacted to each other. In order to achieve the best possible optical performance of the microscope setup, the thickness, especially those of the bottom and top windows, is unconditionally regular and lies within the range of 4 ± 0.005 mm. A specimen of the glass cell material was used for the assembly of the microscope objectives, whose design is adapted for a view through the glass window. All outside surfaces of the glass cell are AR coated for 532 nm, 671 nm, 761 nm and 1064 nm. A coating of the inner surfaces is impossible for technical reasons. To avoid problems caused by reflections from the inner surfaces, the octagonal core is rotated by 3° in the x/y-plane with respect to the z-axis (see Fig. 3.4). The cylindrical tube of the glass cuvette is attached to a rotatable CF40 flange via a non-magnetic glass-metal transition that allows an adjustable mounting of the glass cell to the main chamber. The pumping speed for the glass cell is about 7 l/s, mainly limited by the rectangular feed through between the octagonal core and the glass tube. After evacuating all UHV components, a comparative test measurement with a Hartmann-Shack sensor could not detect any disturbing stress or bending effects on the glass plates, which is indispensable for the quality of the high-resolution optical system.

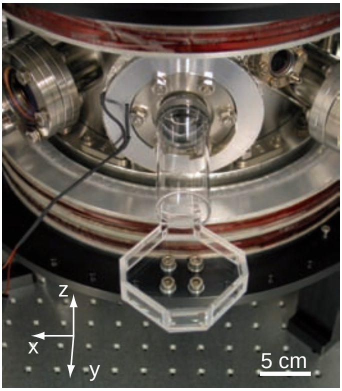

Fig. 3.4: Photo of the mounted UHV glass cell. The given coordinate system defines the main axes of the experiment. The octagonal main body of the glass cuvette is rotated counterclockwise by 3° with respect to the z-axis.

Oven

At room temperature, lithium exists in the solid phase and only becomes liquid at temperatures of about 453 K (see appendix B.1). Even at that temperature the vapor pressure of lithium is still too low to load a magneto-optical trap, which hence can not be loaded from the background pressure as in the case of rubidium [108]. We therefore use an oven emitting an atomic beam of ^{6}Li atoms that is subsequently decelerated by a Zeeman slower and finally captured in the MOT. The oven setup is depicted in Fig. 3.5 and consists of two components, the actual oven and the pumping chamber that interconnects the oven and the differential pump section (see Fig. 3.2). The oven itself is a cylindrical monolithic stainless steel chamber (steel type 1.4429) with a conical diminution towards the oven nozzle (3 mm diameter). This special design realizes the concept of a reflux oven [109]. Initially filled with about 4 g of enriched ^{6}Li (purification to 95%, natural abundance of ^{6}Li: 7.5%) the cylindrical reservoir is permanently heated to about 400°C, causing an increase of the

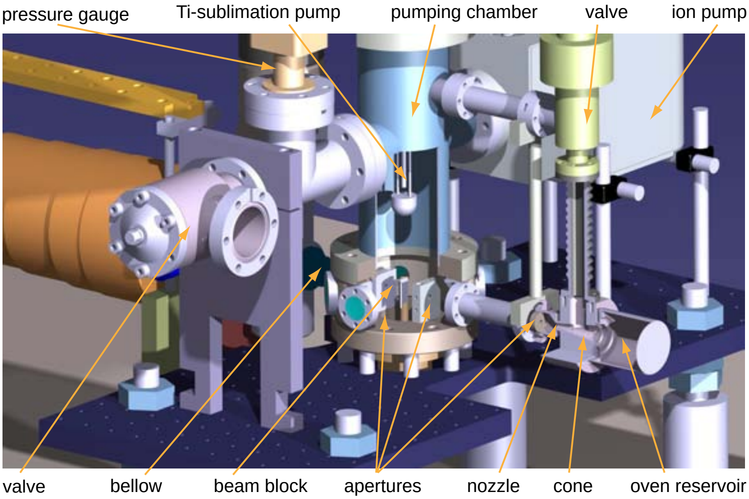

Fig. 3.5: Overview of the oven setup: The oven complex subdivided into two sections, the heated reservoir containing enriched ^{6}Li, and the pumping chamber. Details of the oven are discussed in the text.

lithium vapor pressure to $\sim 5 \cdot 10^{-5}$ mbar. Both, reservoir and nozzle are heated via a corresponding copper sleeve, around which a heating wire (*Thermocoax*) is wound. By tuning the temperature of the reservoir and the nozzle, the flux of atoms emanating from the oven nozzle can be controlled and matched to the velocity threshold of the Zeeman slower. The oven nozzle is set to a lower temperature (200°C) with respect to the reservoir chamber, just above the melting point of lithium. While this nozzle temperature is still high enough to avoid obstructions of the nozzle by deposits of condensed lithium, the reduction helps to keep the temperature of the pumping chamber nearly at room temperature and thus guarantees very good UHV condition. Notches at both ends of the cone enhance the temperature gradient between the oven and the pumping chamber. Evaporated atoms which do not pass the oven nozzle condense in the conical reflux region which is also set to a lower temperature (300°C) than the reservoir. Eroded capillary races along the cone lead the liquid lithium back to the reservoir. Furthermore, the inner walls of the reservoir and the entrance of the cone are faced with a thin mesh that facilitates the reflux and leads to all-around moistening of the hot reservoir walls for a homogeneous evaporation. Since lithium and cooper start to form an alloy at about 300°C, we employ nickel gaskets for all UHV flange connections which may become contaminated with lithium. Along its path to the differential pumping section, the emanating lithium beam is collimated by in total three apertures (3 mm diameter). The first one is placed about 4 cm after the nozzle and casually serves as a protection barrier for superfluous liquid lithium spilling from the oven nozzle. The other two apertures are attached to the bottom flange of the pumping chamber. In between them, a mechanical beam block can be inserted to stop the atomic beam. This block is held at the vacuum-sided end of a mechanical vacuum feed through, which is externally operated by a servo motor. Experimentally, a continuous atom beam does not disturb the performance of the MOT or the operation of the resonator, and therefore we only block the beam when the experiment is set on hold. The atomic beam can be adjusted in position and angle. For this, the entire oven complex is mounted on an movable breadboard. A short vacuum below between the oven complex and the Zeeman slower pipe provides the necessary flexibility of the vacuum system for the adjustment. The oven reservoir is not only evacuated via the nozzle aperture, but also through an additional CF16 tube connection between the oven and the pumping chamber, which increases the pumping of H_2. More technical details of the oven design can be found in [105].

3.3 Laser cooling

The mechanism of laser cooling relies on the action of dissipative light forces caused by resonant light scattering [108, 110]. Atoms propagating in opposite direction to a red-detuned laser beam resonantly scatter photons at a certain velocity due to the Doppler effect. During the stimulated absorption, the photon momentum of $\hbar\boldsymbol{k}$ is transferred onto the atom along the direction of the photon wave vector $\boldsymbol{k}$. In contrast, the spontaneous re-emission of the photons occurs randomly distributed in all directions, and therefore the average momentum transfer caused by spontaneous emission is zero. This results in a net momentum transfer in the direction of the laser beam and thus to a deceleration of the atoms. This effect is exploited in the Zeeman slower for decelerating the atomic beam emanating from the oven nozzle, and in the magneto-optical trap for final trapping and further cooling of the decelerated atoms.

Before describing the implementation of laser cooling in our setup, we will first present the laser system that provides the near resonant light at 671 nm for the Zeeman slower and the MOT.

3.3.1 Laser system

The laser system, a schematic of which can be found in [105], is set up on a separate optical table (laser table) in the laboratory. Single-mode polarization maintaining fibers are used to transfer the light to the experimental apparatus set up on a second optical table (experiment table). For all applications, i.e. laser cooling and imaging, the linewidth of the lasers has to be significantly smaller than the linewidth of the respective atomic transitions. In appendix B.2, we have attached the atomic level structure of ^{6}Li, highlighting all relevant transitions involved in the experiment. Without exception, only transitions along the D2-line of ^{6}Li are driven, which has a natural linewidth of about $\Gamma = 6\,\mathrm{MHz}$ (see appendix B.1). In atomic physics, grating stabilized diode lasers have proven to be an excellent laser light source in order to manipulate the internal and external degrees of freedom of atoms. They offer a sufficiently small linewidth of the order of one MHz, while in addition their wavelength can be tuned with the external cavity by up to some GHz [111]. Their output power varies between 15 mW and 25 mW, depending on the wavelength and the specific laser diode type.

Reference laser For our experiments, we employ such a diode laser as reference for all other near-resonant light sources. Using Doppler-free frequency modulation spectroscopy [112], its absolute frequency is stabilized to the crossover feature of the $F = 3/2$ transition along the D2-line at 670.977 nm (see appendix B.2). The spectroscopy is carried out with a custom-made vapor cell consisting of an evacuated vacuum tube with CF16 view ports at both ends. Like the oven chamber, it is filled with purified ^{6}Li and heated to about 400°C, thus producing a sufficiently high vapor pressure for the spectroscopy. The design and installation of our vapor cell is extensively described in the Diploma thesis of Ch. Zipkes [113].

Zeeman slower light The cooling light for the Zeeman slower is generated with a tapered amplifier (TA), based on a home-made design. The special geometric design of the semiconductor chip imparts a broad gain profile extending more than ±5 nm around the center wavelength. TAs inherit the single frequency mode characteristic from the seeding laser. Here, we use about 10 mW light power of the reference laser for the seeding. Hence, the Zeeman slower light is also resonant to the crossover of the $F = 3/2$ transition, which corresponds to a detuning of 114 MHz to the red for the cooling transition (see appendix B.2). In total, the Zeeman slower TA achieves an output power of 500 mW, about 200 mW of which are directly transferred to the experiment table through an optical fiber.

MOT light Light for the MOT is supplied by a commercial tapered amplifier system (*TOPTICA, TA 100*), which provides an output power of about 500 mW. The internal master laser is stabilized to the reference laser using a standard offset locking technique [114]. The MOT requires a cycling transition for repeated absorbtion and spontaneous re-emission, which for alkali atoms implies a cooling and repumper process (see section 3.3.3). Hence, the MOT light is split into two parts after the TA, one for the cooling, the other for the repumper transition. The respective frequency shifts of ±114 MHz, and also the intensity for both transitions, are adjusted by individual acousto-optical modulators (AOM) in each optical path. Coupled into different fibers, the two beams are separately sent to the experiment table, where they are overlapped on polarizing beam splitter cubes (PBS) and finally redivided in three different paths for the three orthogonal principal axes of the MOT.

Imaging light One additional home-made diode laser provides the resonant laser light for imaging. It is also offset-locked with respect to the reference laser. This specific offset lock enables us to tune the frequency over a wide range ($\sim$ 1 GHz) which is necessary for resonant imaging at different magnetic fields (see appendix B.3). The output line of the imaging laser is split in two independent pairs of optical paths, each pair having the same frequency. One pair travels through a single-path AOM setup shifting the frequency by +80 MHz, while the other pair passes through a double-path

AOM setup giving rise to an additional frequency shift of +80 MHz, hence +160 MHz in total. The two imaging AOMs allow a fast switching of the imaging light. Overall, four transfer fibers allocate the imaging light at any place on the optical table.

3.3.2 Zeeman slower

Due to the oven temperature of 400°C, lithium atoms leave the oven nozzle with a thermal mean velocity of more than 1000 m/s towards the main chamber. However, the MOT can only capture atoms with a maximum velocity of 60 m/s. In our experiment, the required deceleration of the atomic beam is accomplished by a Zeeman slower [110] as depicted in Fig. 3.6. Light from the Zeeman slower TA enters the apparatus through a sapphire viewport at the left hand side of Fig. 3.2 and travels counter-propagating to the atomic beam towards the oven nozzle. The resulting net force from the resonant photon absorption and re-emission effectively decelerates the atoms. Due to the Doppler effect, the slowing atoms would rapidly tune themselves out of resonance with the cooling light halting the deceleration process. Overcoming this problem, a Zeeman slower exploits the Zeeman effect to compensate for the Doppler shift: a spatially varying magnetic field shifts the transition frequency of the cooling cycle in such a way that the atomic beam is kept in resonance on its journey towards the MOT. For this, the spatial profile of the magnetic field $B(x)$ has to fulfill the following condition [108]

$$\frac{\Delta m\, \mu_{\mathrm{B}} B(x)}{h} = \frac{2\pi}{\lambda_{\mathrm{L}}} \left[v(x) - v_{\mathrm{end}} \right] . \tag{3.1}$$

Here, Δm denotes the difference in the magnetic moment between the ground and excited state of the cooling transition, μ_{B} is Bohr magneton, λ_{L} is the resonant laser wavelength at zero magnetic field, and v_{end} and $v(x)$ correspond to the final velocity

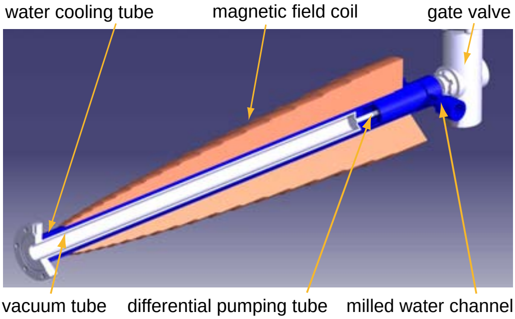

Fig. 3.6: Cut through the Zeeman slower. The decreasing field design allows to slow down the atomic beam from an initial velocity of about 1000 m/s at the oven nozzle to about 60 m/s at the MOT position. In total, the cone of the coil has a maximum length of 571 mm and a maximum radius of 55 mm.

at the MOT position and the velocity profile, respectively.

For our experiment, we built and use a Zeeman slower in decreasing field configuration, i.e. the magnetic field along the beam axis monotonously decreases towards the MOT. For the exact calculation of the required field profile, the magnetic quadrupole field of the MOT coils has also been considered ensuring that the atomic beam is also decelerated efficiently at the very end. A sketch of our Zeeman slower is given in Fig. 3.6. In order to avoid acoustic transmission of mechanical vibrations onto the vacuum system, the wires of the Zeeman slower coil are not directly wound around the drift tube between oven and main chamber, but around a separate spool carrier. This carrier is a double-walled copper tube, which also provides a sufficient water cooling of the Zeeman slower realized by a sophisticated water channel between the outer and inner tube [105]. The Zeeman coil itself consists of 17 double layers and one final single layer of high temperature doubly enameled copper wire ($1 \times 3\,\mathrm{mm}^2$). The glueless winding was done with the help of the company *Bruker*. The different layers are paired, whereas each double layer starts at a different point such that the step like layer configuration adapts to the required, square root like magnetic field profile of equation (3.1). Each double layer is conductively connected to a plug board, where the various pairs are connected in series. This special wiring configuration enables to overleap an eventually broken double layer in the series connection.

Applying a current of 8 A at 50 V, the on-axis magnetic field reaches a maximum of 929 G at the oven side. This value sets the maximum initial beam velocity to 910 m/s, above which atoms cannot be decelerated anymore. The profile of the decelerating laser beam is matched to the divergent profile of the atomic beam by means of telescope optics. With an entrance Gaussian waist ($1/e^2$-radius) of 10 mm at the sapphire viewport, the Zeeman slower beam is focussed down to about 3 mm at the position of the differential pumping tube. Typically, we apply 30 mW light power, which corresponds to more than half of the saturation intensity at any position along the atomic beam. Experimentally, it turned out that the Zeeman slower even works without any repumping light [115], for which reason we only drive the transition $(2\,^2S_{1/2}, m_j = 1/2) \longrightarrow (2\,^2P_{3/2}, m_j = 3/2)$ with circularly polarized light (see appendix B.2). Considering all above settings, about 17% of the atoms emanating from the oven nozzle are decelerated, thereby yielding an estimated flux of about 10^9 atoms/s.

3.3.3 Magneto-optical trap

The Zeeman-slowed atoms are finally captured and further cooled in the magneto-optical trap, right at the center of the main chamber. Here, three orthogonal pairs of counterpropagating, red-detuned laser beams intersect at the center of a magnetic quadrupole field as illustrated in Fig. 3.7(a). The red-detuned laser beams alone form a so-called optical molasses [108], whose velocity dependent forces slow down the atomic motion and thus lead to a compression in momentum space due to laser cooling. In addition, the inhomogeneous quadrupole field causes a spatially dependent Zeeman shift of the cooling transition and thus a spatially varying detuning. If the co- and counter-propagating laser beams show opposite circular polarizations, the combination of both gives rise to spatially varying dissipative and confining forces. Laser cooling in a magneto-optical trap, especially in the case of ^{6}Li, owing to its hyperfine splitting in the excited state (see appendix B.2), is fundamentally limited to the so-called Doppler temperature [116], which is given by the stochastic nature of the absorption and emission process. For ^{6}Li, the Doppler temperature amounts to $140\,\mu$K. For further information about the theory of magneto-topical traps, we refer to [108, 110, 117].

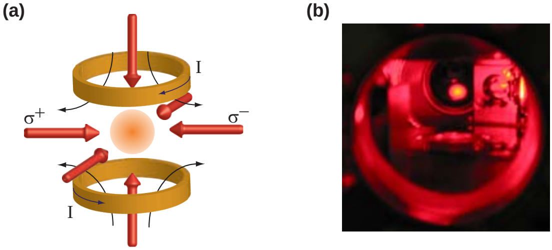

Fig. 3.7: (a) Schematic of the magneto-optical trap: The combination of a magnetic quadrupole field and six counterpropagating laser beams leads to the trapping and cooling of neutral atoms in the center of the quadrupole field. (b) Photo of fluorescing ^{6}Li atoms captured in the MOT of the presented apparatus. The shown atomic cloud contains about 10^9 atoms at a temperature of some hundred microkelvins.

The pair of magnetic coils, that is used to generate the magnetic quadrupole field in our experiment, is illustrated in Fig. 3.3(a). Its design was chosen such that the magnetic field of the MOT is smoothly matched to the magnetic field of the Zeeman slower, thereby optimizing the loading efficiency of the MOT. A single coil consists of two sub-coils in series, each of them built up of 45 windings of high-temperature, doubly enameled copper wire ($1 \times 5\,\mathrm{mm}^2$). The wire is wound on a double-walled aluminum carrier which supports an internal water channel for sufficient cooling of the coils. We operate the MOT coil pair in anti-Helmholtz configuration, giving rise to the required magnetic quadrupole field. Applying a current of 30 A, we achieve a magnetic field gradient of 6.75 G/cm along the x- and y-axis, and -13.5 G/cm along the z-axis respectively.

For the laser cooling, we use the transition from the $F = 3/2$ manifold of the $2\,^2S_{1/2}$ ground state to the $2\,^2P_{3/2}$ excited state . However, this is not a closed transition as excited atoms can also decay to the $F = 1/2$ manifold of the ground state. Therefore, we also apply repumper light along all MOT axes which drives the $(2\,^2S_{1/2}, F = 1/2) \longrightarrow (2\,^2P_{3/2})$ transition. For loading the MOT, both repumper and cooling light are detuned by 39 MHz to the red, which corresponds to $-6.5\,\Gamma$. In contrast to ^{87}Rb, samples of ^{6}Li atoms trapped in MOT are rather dilute. This allows us to operate the MOT in retro-reflected configuration, i.e. only three laser beams have to be employed, each along one of the orthogonal principal axis of the MOT. After once having passed the MOT, each beam is retro-reflected by a mirror with a $\lambda/4$ retardation plate in front, which generates the corresponding counter-propagating beam with the appropriate polarization. In order to maximize the trapping volume of the MOT, we use the full aperture of the CF40 viewports for transmitting the cooler and repumper light through the MOT. At this size, we drive both transitions at about saturation intensity. Fig. 3.7(b) shows a photo of a ^{6}Li atomic cloud captured in the MOT. The lifetime of the atoms in the MOT is of the order of 20 minutes, indicating a very low background pressure.

3.4 All-optical evaporative cooling

The temperature ($140\,\mu$K) and phase space density (10^{-6}) achievable in a magneto-optical trap do by far not meet the conditions of quantum degeneracy. We overcome this by evaporative cooling in the conservative potential of an optical dipole trap, which is realized by a focused, off-resonant laser beam. For the evaporative cooling process, the depth of the dipole trap is slowly reduced by lowering the laser power in the trapping beam. As a result, the most energetic particles of the sample are allowed to escape from the trap causing a truncation of the high-temperature tail of the Boltzmann-distribution. If the lowering of the trap depth is sufficiently slow for re-thermalization to occur, interparticle collisions continuously restore the Boltzmann distribution, yet at a lower average temperature, which implies an effective cooling of the gas accompanied by a noticeable particle loss. The speed with which the potential depth can be reduced and hence the cooling can be driven depends on the collision rate of the atoms. Experimentally, we control this parameter by means of a Feshbach resonance as discussed in chapter 2.2.

Optical dipole force

The capability of trapping neutral particles in a spatially inhomogeneous light field of frequency ω, which is detuned by $\Delta = \omega - \omega_0$ from an atomic transition with frequency ω_0, owes to the conservative interaction between off-resonant light and matter. This process can be understood in a semi-classical picture: the electric field of the light induces an electric dipole moment $\boldsymbol{d}$ in the atom that is proportional to the electric field strength $\boldsymbol{d} = \alpha\,\boldsymbol{E}$, where α is the complex polarizability of the atom. Averaged over time, the induced dipole moment, in turn, experiences a potential U in the electric field due to the dispersive real part of α,

$$U_{\mathrm{dip}} = -\frac{1}{2}\langle \boldsymbol{d}\cdot\boldsymbol{E}\rangle = -\frac{1}{2}\langle \alpha\,\boldsymbol{E}^2\rangle = -\frac{1}{2\epsilon_0 c}\mathrm{Re}(\alpha)\,I\,, \tag{3.2}$$

where I is the intensity distribution of the light. The sign of the polarizability depends on the detuning of the trapping beam from the atomic resonance. For red detuning, α is positive and the atoms are attracted towards regions of high intensity. Even though the trapping light is far detuned from any atomic transition, there also exists a non-vanishing probability for the atom to absorb and re-emit a photon out of the light field. This spontaneous scattering rate is related to the absorptive imaginary part of the polarizability by

$$\Gamma_{\text{dip}} = -\frac{1}{\hbar\omega}\langle \boldsymbol{d}\cdot\boldsymbol{E}\rangle = -\frac{1}{\hbar\epsilon_0 c}\text{Im}(\alpha)\, I\,, \tag{3.3}$$

For a moderate detuning, one can derive an analytic expressions for the trapping potential and the scattering rate of photons [31]:

$$U_{\text{dip}}(x,y,z) \quad = \quad -\frac{3\pi c^2}{2\omega_0^3}\left(\frac{\Gamma}{\omega_0-\omega}+\frac{\Gamma}{\omega_0+\omega}\right) I(x,y,z) \tag{3.4}$$

$$\Gamma_{\text{dip}}(x,y,z) \quad = \quad -\frac{3\pi c^3}{2\hbar\omega^3}\left(\frac{\omega}{\omega_0}\right)\left(\frac{\Gamma}{\omega_0-\omega}+\frac{\Gamma}{\omega_0+\omega}\right)^2 I(x,y,z)\,. \tag{3.5}$$

As the dipole potential scales like $U_{\text{dip}} \sim I/\Delta$, whereas the scattering rate scales like $\Gamma_{\text{dip}} \sim I/\Delta^2$, it is most preferable for a given dipole potential depth to work with larger detunings and higher intensities in order to avoid unwanted spontaneous scattering events. From this derivation it can be also seen that optical dipole traps offer the advantage to confine any ensemble of neutral atoms without restrictions to the internal magnetic state, which casually enables the untroubled employment of magnetic Feshbach resonances.

In our experiment, we use a combination of two different dipole traps operated with far off-resonant light (1064 nm) to finally reach quantum degeneracy in the trapped Fermi gas. The first trap is a standing-wave dipole trap, realized by the in-vacuo optical resonator in the main UHV chamber. This trap provides a deep, large-volume trapping potential allowing to transfer a large number of atoms from the MOT into the second optical dipole trap, a tightly focussed optical tweezer. After having been transferred, the trapped sample is subsequently transported into the glass cell by moving a lens in the optical path of the tweezer. Besides the ability for the optical transport, the tweezer offers the advantage that its power can be precisely controlled over 4 orders of magnitudes. This eventually allows us to efficiently cool the trapped particles down to some tens of nanokelvins.

3.4.1 Resonator trap

In principle, particles could be directly transferred from the MOT into a running wave dipole trap (optical tweezer) as realized in other experiments [49, 118]. Following this approach, an efficient transfer requires very high optical powers for the dipole trap, amounting to at least some tens of Watts employing e.g. a commonly used Nd:YAG laser at 1064 nm. Apart from laser safety reasons, these high powers are accompanied by further issues, such as thermal lensing when light of high intensity passes for example through a vacuum viewport. We therefore decided to use an optical resonator as intermediate trapping potential that supports a convenient atom transfer from the MOT into the final trapping configuration, the above mentioned running wave dipole trap. On the one hand, the resonant enhancement of light power eases to attain potential depths which exceed the mean kinetic energy of particles trapped in the MOT. Thus, only moderate input powers (fairly below 5 W) have to be applied. On the other hand, the geometry of the resonator mode can additionally be chosen in such a way that it provides a good spatial overlap with the confining volume of the MOT. Although the resonator will be operated with low injection powers, the enhanced light field in between the two mirrors nevertheless has to exceed some hundred Watts, providing a trapping potential which at least surpasses the Doppler temperature of 140 μK. This almost presupposes to place the resonator into the vacuum chamber in order to avoid serious damages of the mirror surfaces caused by high light intensities, and also to minimize loss processes which otherwise would occur when the resonator mode had to pass through the vacuum viewports (about 2% per round trip).

Geometry

As briefly mentioned in section 3.2.2, we use a linear resonator in hemi-spherical configuration. It consists of one planar mirror M_1 and one curved mirror M_2 with radii of curvature $R_1 = \infty$ and $R_2 = 150$ mm, respectively. The mirrors are placed symmetrically around the MOT position at the center of the main chamber as illustrated in Fig. 3.8. The resonator axis is horizontally oriented in the x/y-plane on a level with the MOT, and turned by 72° with respect to the Zeeman slower axis. The planar mirror is located in the oven-sided half of the MOT chamber close to the CF60 viewport, whereas the curved mirror is placed in the opposite half close to the glass cell (see Fig. 3.1). The mechanical setup of the mirror mountings will be discussed separately later on. We operate the resonator slightly below the stabilization limit, i.e. the resonator length L has been chosen to be only marginally smaller than the radius

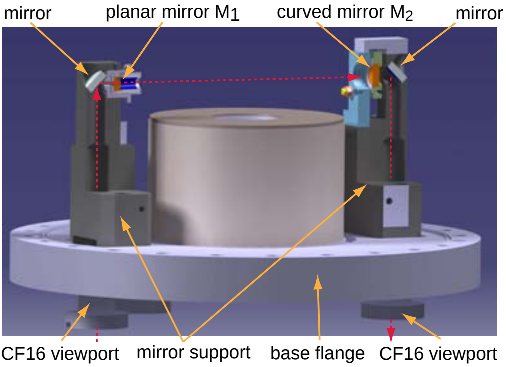

Fig. 3.8: Cut through the optical resonator which is operated inside the main UHV vacuum chamber. The two massive mechanical supports holding the resonator mirrors are rigidly mounted onto the CF200 base flange of the main UHV chamber, ensuring a high passive stability of the resonator mode.

of curvature R_2. The injected light field and the resonator have been aligned with respect to each other in such a way that only the lowest transversal mode TEM_{00} is excited. Here, the choice of the resonator length L allows us to adjust the waist of the resonator mode $w(y_r)$ along the resonator axis y_r [119]. The actual resonator length has been determined in a separate measurement of the frequency separation between different transversal and axial modes [105], yielding $L = 14.975\,\mathrm{cm}$. Correspondingly, the resonator has a free spectral range of $FSR = \frac{c}{2L} \simeq 1\,\mathrm{GHz}$, which is equal to the inverse of the round trip time of a single photon. Light is coupled into the resonator through the planar mirror, where the resonator mode has the smallest waist. There, the waist of the injection beam has been estimated to be $w_0 = (45 \pm 5\,\mu\mathrm{m})$, resulting in a waist of the resonator mode at the MOT position $y_r \simeq L/2$ of about $w_{L/2} \simeq 550\,\mu\mathrm{m}$.

Power enhancement - mode and impedance matching

Light injected to the resonator travels back and forth between the two high-reflection mirrors, in this way building up a standing-wave light pattern whose intensity strongly depends on the number of round trips per photon, and thus on the quality of the mirrors. In general, the power enhancement S of a resonator is fully characterized by the reflectivity (r_1, r_2) and transmission (t_1, t_2) of both mirrors, as well as the amplitude losses l of the resonator:

$$S = \frac{t_1 t_2}{(1 - r_1 r_2 l)^2}\,. \tag{3.6}$$

In order to maximize the potential depths of the resonator trap, we matched the mode of the injected laser beam to the mode of the resonator by an accurate choice and alignment of the optical components in front (telescope optics). In addition, we demanded for specific reflectivities of both mirrors such that the injected power approximately compensates the losses process of the resonator owing to absorption and scattering losses of the mirrors. Both mirrors were manufactured and characterized by *ATFilms*, exhibiting a reflectivity of $99.98 \pm 0.005\%$ and a transmission of 0.015%. The loss process and hence the quality of the resonator is commonly reflected in its finesse F. This quantity is directly proportional to the number of round trips a photon can carry out on average before the energy inside the resonator drops by a factor of $1/e$. We determined the finesse F of our resonator by measuring the so-called cavity-ring-down time, after the injection power has been suddenly switched off. The measurement yields $F = 10200$ and allows us to estimate the resonator losses via $F = (\pi\sqrt{r_1 r_2 l})/(1 - r_1 r_2 l)$. Inserting all parameters into equation (3.6), our resonator provides a power enhancement of $S = 1580$. To feed the resonator trap, we use an ultra-stable, diode-pumped Nd:YAG laser (*InnoLight, Mephisto 2000*) with a nominal output power of 2 W at 1064 nm, about 600 mW of which are typically injected into the resonator. Hence, the power of the standing-wave light field building up between the two resonator mirrors can easily exceed 1 kW, again emphasizing the need to set up the resonator inside the main UHV chamber.

Trapping potential

Using equation (3.8), we can calculate the depth of the resonator trap for ^{6}Li atoms that are confined in the standing light field right in between both mirrors at the position of the MOT:

$$U_{resonator} \simeq k_{\mathrm{B}} \cdot (800\,\mu\mathrm{K/W}) \cdot P\,. \tag{3.7}$$

Here, P denotes the injected power of the trapping light. Typically, we work with an initial trapping depth of $k_{\mathrm{B}} \cdot 500\,\mu$K when transferring the atoms from the MOT into the resonator. As a result, the trapped atoms spread out over approximately 6000 individual potential wells of the standing wave.

Mechanical setup

Placing a high-finesse optical resonator operated close to the stability limit into an UHV vacuum setup is a rather challenging task as a re-alignment of the resonator mode is of course impossible after having closed the vacuum chamber. Moreover, the alignment necessarily has to survive a backing out of the whole setup up to 180 °C. These conditions already make high demands on the opto-mechanics of the resonator and the mirrors themselves. On the one side, the mounting should enable a convenient and tunable alignment of the mirror geometry, while on the other side it has to guarantee a long-term passive stability allowing an untroubled operation in close vicinity to strong magnetic fields under UHV.

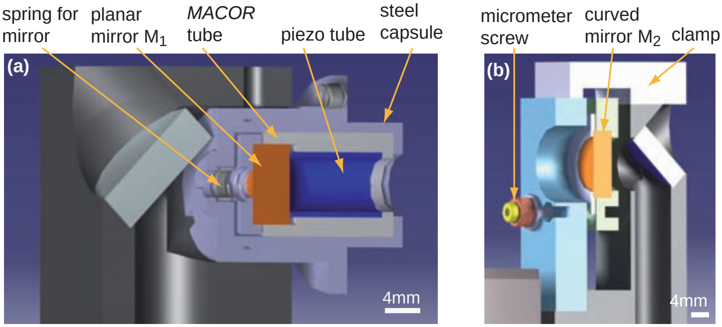

Fig. 3.9: Cut through the mirror mounts of the resonator setup revealing details of the opto-mechanics used to align and stabilize the resonator mode. (a) shows the piezo-driven holder of the planar resonator mirror enabling a fine adjustment of the axial resonator length. (b) illustrates the kinematic mount of the curved resonator mirror allowing a tilting along two perpendicular axes.

In our apparatus, each of the two resonator mirrors is mounted in a separate collar-like mechanical support made of stainless steel, both of which are shown in Fig. 3.8.

The UHV-compatible, massive construction is directly attached to the CF200 bottom flange of the main chamber. The latter features two vertical CF16 viewports for each mirror mount, through which the resonator light is coupled in and out. Trapping light, vertically injected into the support of the planar mirror, is transmitted upwards through a light channel in the interior of the collar, horizontally reflected by a rigidly mounted 45° mirror (*CVI Melles Griot*, 1/2 inch, HR 1064 nm), and finally coupled into the resonator through M_1. At the opposite end of the resonator, the trapping light is coupled out through the curved mirror M_2 and leaves the vacuum chamber in the same manner, but reversed order. The actual mirror holders enabling the alignment of the resonator mode are housed in the top of each resonator collar. Details are presented in Fig. 3.9(a)-(b). The planar mirror (diameter 7.75 mm, thickness 4 mm) is embedded in a sophisticated capsule-like holder that allows both, a coarse and fine adjustment of the resonator length L. For the coarse adjustment, the whole capsule is axially guided by a cylindrical feedthrough in the main collar and can be moved back and forth by turning three spring loaded screws (M2.5) with corresponding threads in the collar corpus. The fine adjustment is accomplished by a hollow piezo-cylinder that presses the planar mirror against a spring-loaded counter bearing inside the stainless steel capsule. To improve the slippage of the piezo and the mirror, both are inserted in a ceramic tube made of *MACOR* (see Fig. 3.9(a)). The curved mirror (diameter 10 mm, thickness 4 mm) is mounted in a two-component kinematic mirror holder. Its tiltable back plate contains the mirror itself, while the rigid front plate is directly attached to a protruded pedestal of the main support as illustrated in Fig. 3.9(b). The mirror is fixed by a flat steel ring that helps to distribute the clamping forces uniformly on the mirror surface, thus minimizing unwanted birefringent side effects. Two spring-loaded micrometer screws (lockable) between front and rear plate enable an adjustable tilt of the curved mirror along two perpendicular axes.

Locking technique

Trapping light only enters the resonator if the resonator length L is an integer multiple of the light wavelength λ, i.e. $2L = n\lambda$ with $n \in \mathbb{N}$. This resonance condition has to be necessarily fulfilled within the spectral linewidth of the excited resonator mode $\Delta\nu_{\mathrm{res}}$, which is solely determined by the finesse F and the free spectral range FSR of the resonator through $\Delta\nu_{\mathrm{res}} = FSR/F$. For our resonator, the linewidth of the TEM$_{00}$ amounts to 98 kHz, corresponding to a change in the resonator length of $5.3 \cdot 10^{-11}$ m. However, the resonator length as well as the frequency of the injection light are intrinsically affected by short and long term drifts, which have to be compensated for by stabilizing at least either of them. In our experiment, we stabilize the frequency of the injection laser via a Pound-Drever-Hall lock [120, 121]. This technique employs a phase-modulation of the injection light and uses the fact that light reflected from the in-coupling mirror M_1 acquires a phase shift with respect to the transmitted light. We accomplish the the phase-modulation of the carrier frequency ν_{mod} via an electro-optical modulator (EOM), generating side bands at $\nu_{\mathrm{L}} \pm \nu_{\mathrm{mod}}$ with a modulation frequency of $\nu_{\mathrm{mod}} = 228\,\mathrm{MHz}$. Experimentally, the beat signal occurring between the sidebands and the carrier frequency of the reflected beam is detected on a photodiode (PD) and demodulated by frequency-mixing with a local oscillator of the same frequency. Close to resonance, the resulting signal is proportional to the phase shift, which we subsequently convert into an appropriate error signal $\delta\nu_{\mathrm{error}}$ by means of electronics. This error signal, is fed back to a custom-made PID (Proportional-Integral-Derivative) device, whose output control signal ν_{control} is sent to two regulation devices in order to stabilize the injection light onto the resonator mode. On the one hand, the control signal is sent to a piezo-electric device in the Nd:YAG laser allowing to adjust the laser frequency with a regulation bandwidth of 100 kHz. However, a voltage divider in the feedback line for the piezo reduces the bandwidth to 300 Hz. On the other hand, the integrated part of the PID loop is used to regulate long-term drifts of the laser frequency via the temperature feedback of the Nd:YAG crystal. In order to correct for deviations on a fast time scale, we directly apply the error signal from the demodulation onto an acousto-optical modulator (AOM) in the optical path of the injection light. Without significantly changing the coupling efficiency to the resonator due to the slightly varying deflection angle of the injection beam, the AOM loop allows for a regulation bandwidth up to 200 kHz. An overview of the locking scheme and also the below described intensity stabilization is given in Fig. 3.10.

Intensity stabilization

Experimentally, the intensity of the resonator has to be precisely controllable for two reasons. First, the number of atoms transferred from the MOT into the resonator

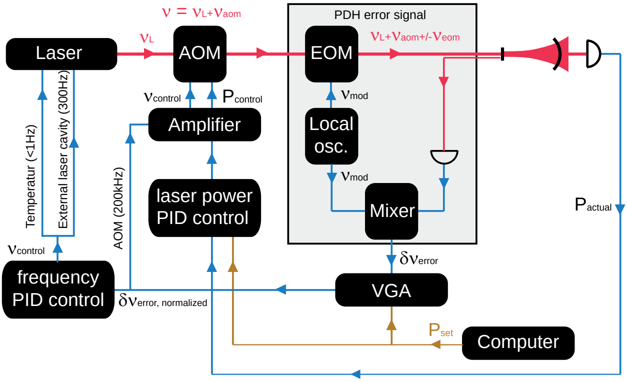
ν = νL+νaom
PDH error signal
νL
Laser
AOM
EOM
νL+νaom+/-νeom
νcontrol
Pcontrol
νmod
Amplifier
Local osc.
Temperatur (<1Hz)
External laser cavity (300Hz)
AOM (200kHz)
laser power PID control
νmod
Mixer
Pactual
νcontrol
δνerror
frequency PID control
VGA
δνerror, normalized
Pset
Computer

Fig. 3.10: Schematic of the Pound-Drever-Hall locking scheme used to stabilize the trapping light onto the in-vacuo resonator. Part of this setup also illustrates the PID control loop for the intensity stabilization of the resonator trap.

strongly depends on the stability of the initial trap depth during the transfer. And second, the trapped sample is evaporatively pre-cooled in the standing wave potential since a reduced temperature enhances the efficiency of the final transfer into the running wave dipole trap. For the cooling process, we lower the optical power inside the resonator down to 20% of its initial trap depth following a slow exponential ramp. In order to stabilize the intensity during the ramp, we measure the trapping power by monitoring the resonator transmission on a photodiode (PD). This signal is fed into a servo loop (PID controller) that regulates the light intensity using an AOM in the optical path of the injection light. When the intensity in the resonator trap is reduced for evaporation, the error signal in the closed loop feedback system is correspondingly reduced, and the lock becomes less stable. To solve this problem, we electronically normalize the error signal by the set value of the feedback loop through a variable gain amplification (see VGA in Fig. 3.10), making the error signal independent of the actual trap power.

3.4.2 Running wave dipole trap

For the final evaporative cooling below quantum degeneracy, the trapped sample is transferred from the resonator trap into a running wave dipole trap that is readily provided by a focused, red-detuned laser beam at 1064 nm. On the one hand, this Far Off-Resonance Trap (FORT) allows an effective and more convenient evaporative cooling than the resonator trap because its intensity can be reliably regulated to very low values during the final stage of the evaporation ramp. On the other hand, the running wave trap offers a simple and technically practicable possibility to transport the trapped sample to a location with enhanced optical access, the octagonal glass cell in our setup.

Trap setup

As light source for the FORT, we use a fiber amplifier stage (*NUFERN, SFA-PM1064-10W-0*) emitting light of 10 W at a wavelength of $\lambda = 1064\,\text{nm}$. This fiber amplifier stage needs to be seeded by about 100 mW light power at the same wavelength, for which we sideline a small portion of the Nd:YAG light used to run the resonator. To do forced evaporative cooling, the power of the trapping light has to be reduced tremendously, which we accomplish by an AOM. After passing through the latter, the output beam of the fiber laser is sent through a single mode optical fiber for transversal mode cleaning. In addition, the cleaning fiber enables an easy replacement of the laser source without altering the orientation of the beam path after the fiber, and thus without affecting the position of the FORT[1]. A lot of care has been taken for the setup of the optical path after the cleaning fiber aiming at un undisturbed Gaussian beam profile in the focal position of the FORT where the atoms are trapped. Using the out-coupling optics of the cleaning fiber and another achromatic lens, the expanded FORT beam is collimated to have a waist of about 25 mm. The actual focussing of the FORT is done by a second achromatic lens with a focal lens of $f = 1000\,\mathrm{mm}$ (*THORLABS, AC508-200-B*). It is this lens, which is mounted on an air bearing translation stage, and by this enables to transport the atoms from the center of the main chamber into the glass cell. For a sufficient passive pointing stability of the FORT, the opto-mechanics of all optical components along the beam path is rigidly constructed, in particular the mounts of the 3 inch mirrors guiding the FORT beam towards the atoms.

---

[1] The specific type of the cleaning fiber used is not suited for optical powers about 3.5 W, above which the transmitted power saturates. This currently limits the maximum trap depth of the FORT. It should be replaced by a high-power optical fiber.

Trap parameters

A measurement of the axial and transversal beam profile of the FORT in the vicinity of the focal position provides all information to characterize the confining potential of the optical dipole trap, which can be expressed in terms of the Gaussian intensity distribution of the trapping beam [31, 122]:

$$U_{\mathrm{dip}}(r,z) = -C(w)I(r,z) = -C(w)\,\frac{2P}{\pi w^2(z)}\,e^{-2r^2/w^2(z)}\,. \tag{3.8}$$

Here, P denotes the power of the trapping light and w is the beam waist as a function of the axial position z. In the focal position, we measure a beam waist of $w_0 = (22{\pm}1)\,\mu\mathrm{m}$. The exact knowledge on this parameter is of great importance since it strongly affects the experimental determination of other physical quantities, such as the temperature or the number of particles trapped in the FORT (see chapter 6.4). The maximum depth of the potential is given by $U_0 = 2P/\pi w_0^2$. In axial direction, the theoretical Rayleigh length is readily calculated to be $z_R = \pi w_0^2/\lambda = 1.3\,\mathrm{mm}$. However in our case, the measured axial beam profile deviates from the standard relation $w(z) = w_0\sqrt{1+(\frac{z}{z_R})^2}$, due to a truncation of the trapping beam by the finite aperture of the final achromatic lens. However, at very low trapping powers, the overall trapping potential is not only determined by the intensity distribution of the optical dipole trap, but also by residual magnetic field gradients (Feshbach field, see section 3.5) and gravity. In particular, the weak axial confinement is affected by these distortions. For the forced evaporative cooling, we typically apply a homogenous magnetic field to tune the interparticle collision properties by means of Feshbach resonances. Indeed, the magnetic Feshbach field applied at the final position in the glass cell exhibits some residual curvature B'' giving rise to an additional harmonic trapping potential in axial direction:

$$U_{\mathrm{mag}}(z) = -\frac{1}{2}\,\mu_{\mathrm{B}}\,B'' z^2\,. \tag{3.9}$$

For the pair of Feshbach coils above and below the glass cell (see section 3.5), the curvature of the magnetic field has been estimated to be $B'' = 0.048\,\mathrm{cm}^{-2}\cdot B$ in the horizontal plane (x/y-plane). For low optical trapping powers at the end of the evaporation process, the magnetic trapping potential is the dominating contribution to the axial confinement. The corresponding harmonic trapping frequency is given by

$$\omega_{\mathrm{mag}} = \sqrt{\frac{\mu_{\mathrm{B}} B''}{m}}\,. \tag{3.10}$$

In contrast, the magnetic confinement due to the magnetic Feshbach field in the main chamber does not need to be taken into account, because there, the FORT is operated at full power and thus the optical confinement dominates over the magnetic contribution.

Intensity stabilization

As for the resonator trap, evaporative cooling in the FORT also requires precise control of the intensity of the trapping laser. For the intensity stabilization, we again monitor a small portion of the trapping light on a photodiode and use a PID servo loop that acts on an AOM placed in front of the cleaning fiber of the FORT. This task, however, turns out to be even more challenging since the FORT intensity needs to be regulated over more than three orders of magnitude from 3.5 W down to below 10 mW. In order to achieve a nearly constant PID gain over the full regulation power, we employ logarithmic amplifiers for the power detection. Details of the logarithmic power control can be found in [105].

3.4.3 Optical transport

Exploiting the principle of optical tweezers, atoms confined in the FORT follow the focal position when it is moved in space. We use this mechanism to transport the pre-cooled atomic sample over a distance of 268.8 mm from the MOT position in the main chamber to the center of the octagonal glass cell. The corresponding shift of the focus is done by moving the final achromatic lens ($f = 1000\,\mathrm{mm}$) in the optical path of the FORT. For this, the achromatic lens is mounted on a linear air bearing stage (*AEROTEC, Model AERABL20030-M-10-NC*) that provides a maximum travel of 300 mm and whose translation profile can be precisely controlled with a position accuracy of better than 1 μm. For the transport, we drive a smooth velocity profile with moderate accelerating and decelerating forces which must not exceed the restoring forces of the dipole trap in axial direction. During the transport, the FORT is operated at a power of about 2.0 W, corresponding to a trap depth of about $U_{\mathrm{dip}} = k_{\mathrm{B}}\,300\,\mu\mathrm{K}$. In total, the transport takes 500 ms, for which we do not observe a significant heating or spilling of the cold atomic sample. Experimentally, even shorter transport times with accelerations above the gravitational acceleration g are possible and would not lead to higher particle loss rates, but cause vibrations on the experimental table which we want to avoid for other technical reasons. We also checked that the continuous air flow of the translation stage does not influence the performance of our apparatus.

To obtain reliable and reproducible experimental data, the transport rate has to be reproducible over many experimental cycles. For this, the position of the dipole trap in the glass cell - given by the maximum of the magnetic Feshbach field inside the glass cell - is actively stabilized. A quadrant photodiode measures the actual position of the optical dipole trap, whereupon a PI loop corrects for deviations via a piezo-driven mirror placed along the optical path of the dipole trap. With this stabilization scheme, we achieve a standard deviation in the FORT position of less than 1 μm. The PI loop is realized with a field programmable gate array (National Instruments, NI 9264/9205/9401), details of which are given in [123, 124].

3.5 Magnetic fields

Our experimental setup involves an elaborate system of several magnetic coils for different tasks: for laser cooling, magneto-optical trapping, gradient fields, levitation and for tuning the scattering properties of the lithium gas. An overview of all magnetic coils, except the Zeeman slower, is given in Fig. 3.11. For the design of our solenoid system, we paid attention that the mounting of the coils does not have contact to the vacuum setup and the optical system. Fig. 3.11 also shows the rigid construction of the coil holders, robust against disturbing influences of mechanical vibrations caused by switching the magnetic fields. A detailed characterization of the coil setup can be found in the PhD thesis of Bruno Zimmermann [105]. Here, we restrict ourselves to a summarizing description, providing only the most essential technical information.

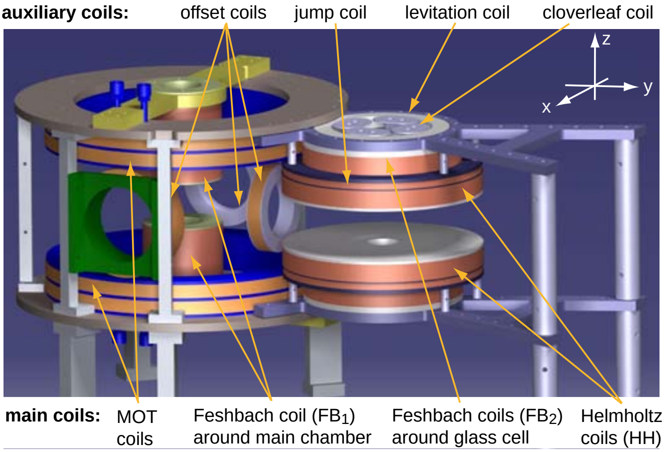
auxiliary coils:
offset coils
jump coil
levitation coil
cloverleaf coil
z
y
x
main coils:
MOT coils
Feshbach coil (FB$_1$) around main chamber
Feshbach coils (FB$_2$) around glass cell
Helmholtz coils (HH)

Fig. 3.11: Overview of the magnetic coil system. The setup can be divided into main and auxiliary coils, depending on the current at which they are operated. All main coils are driven with a current of more than 10 A provided by a single power supply. The auxiliary coils are operated by less than 2 A, each driven by a separate power supply.

3.5.1 Main coils

As main coils we denote those solenoids of our apparatus which are driven by currents of more than 10 A, and therefore need to be actively cooled. Apart from the Zeeman slower coil, they are all operated by a single power supply (*EA Elektro-Automatik, EA PA-PS-9080-300*, $I_{\mathrm{max}} = 300\,\mathrm{A}$, $U_{\mathrm{max}} = 80\,\mathrm{V}$). The active current stabilization in each of the main coils is accomplished by a PID feedback loop that measures inductively the actual current and reports deviations from the set value to a regulation unit. The latter is realized by a self-designed switch box based on insulated gate bipolar transistors (IGBT), allowing to branch and precisely control the driving current for the different coils [105].

Zeeman slower and MOT coils For the field configuration and design of the Zeeman slower and MOT coils, we refer to the preceding sections 3.3.2 and 3.3.3, where we have already presented the corresponding technical details.

Feshbach coils around main chamber The scattering length of ^{6}Li atoms vanishes at zero magnetic field. However, evaporative cooling requires sufficient rethermalization mediated by collisions. Thus, we apply a constant magnetic offset field to tune the scattering properties by means of the ^{6}Li Feshbach resonance. For the evaporative pre-cooling in the resonator trap, we usually work at a magnetic field of 300 G, yielding an s-wave scattering length of about $-300\,a_0$. To achieve this field strength at the position of the atoms using moderate currents, the Feshbach coils FB_1 are embedded in the inlets of the top and bottom CF200 flanges of the main chamber, as close as possible to the atoms (see also Fig. 3.3). Each coil is made up of 99 windings (4 layers) of $4 \times 4\,\mathrm{mm}^2$ copper wire, providing a magnetic field of 3.5 G/A. The square profile is hollow, with an inner diameter of 2.5 mm, through which we run cooling water for efficient removal of resistive heat.

Feshbach coils around glass cell Similarly, another pair of Feshbach solenoids (FB_2) is mounted in close vicinity of the glass cell, allowing us to tune the scattering properties of a spin-mixture Fermi gas over the full range of interest, i.e. from zero scattering length at zero magnetic field to beyond the BEC-BCS crossover regime above 1000 G (see Fig. 2.3). Each coil is composed of 146 windings in total, exhibiting a T-shaped cross-section profile. We used the same hollow copper wire as for FB_1 for water cooling. The FB_2 solenoids generate a magnetic field of 8.629 G/A at the center of the glass cell. However, the separation of the two coils is larger than for a Helmholtz configuration, giving rise to a field curvature of $B'' = 0.048\,\mathrm{cm}^{-2} \cdot B$ in the horizontal plane and twice this value in vertical direction. The resulting magnetic confinement caused by this field curvature (see equation (3.9)) becomes more and more relevant when the optical confinement is decreasing. This harmonic magnetic trap is the dominating confinement along the axial direction of the FORT for very shallow optical trap depths, as has already been discussed in section 3.4.2.

Helmholtz coils around glass cell An additional pair of coils is wound around the Feshbach coil FB_2 that provides a nearly homogeneous magnetic field of 5.42 G/A at the center of the glass cell. We denote this solenoid as Helmholtz coil (HH), whose 55 windings per solenoid are also made up of the same hollow copper wire.

3.5.2 Auxiliary coils

Besides the main solenoids, several small auxiliary coils were installed at our apparatus, disposed for various additional tasks. The windings of these coils are made of enameled round cooper wire (∅1 mm). As current source, we use three power supplies from *STATRON* (Mod. 3240.2, remote controlled by computer). Another switching board based on MOS-FETs branches the current for the different auxiliary solenoids. The offset coils around the MOT are not actively cooled by water and can thus only be operated for a few seconds within the experimental cycle. In contrast, the other auxiliary coils are thermally coupled to the main coils, providing sufficient cooling.

MOT offset coils Experimentally, the position of the MOT center is set by the minimum of the magnetic quadrupole field and the Zeeman slower axis. Actually, this point does not coincide with the mode volume of the running wave dipole trap, which in turn is spatially fixed by the position of the resonator mirrors. Offset coils along the x-, y- and z-axis of the main chamber allow us to shift the position of the trapped atoms after the MOT loading to any position of the resonator mode within a range of a few centimeters. The windings for the two offset coils along the Zeeman slower axis and for the single offset coil along the x-axis are supported by separated holders, whereas the wire for the offset field in vertical direction is wound on top of the cylindrical shell of the Feshbach coils FB_1. For each coil, we wound as much wire as possible according to the amount of available space. The exact number of spooled windings is unknown, but also irrelevant. The required driving currents of about 2 A, to shift the MOT into the right position, have been determined experimentally.

Levitation coils Each spool carrier of the solenoid system above and below the glass cell supports about 80 windings of ∅1 mm copper wire that are driven by 2 A in opposite direction. The resulting magnetic field gradient in vertical direction is used to compensate for gravitation by levitating the atomic sample.

Jump coils A similar coil pair, driven in Helmholtz configuration, produces a homogenous magnetic field of up to 300 G. Due to the small dimensions, their small inductance allows a fast switching of the overall homogenous magnetic field if rapid changes are needed.

Cloverleaf coils Each spool carrier above and below the glass cell contains four small solenoids arranged in cloverleaf configuration as shown in Fig. 3.11. This system is designed to generate magnetic field gradients in the focal plane of the microscope setup. Details are given in [125].

3.6 Imaging techniques

The majority of diagnostic techniques for ultracold quantum gases relies on optical probing. Owing to a very diversified spectrum of applications, the different methods can be classified into several categories: photon-counting and imaging, *in-situ* and time-of-flight (TOF), destructive and non-destructive, absorptive and dispersive. A very comprehensive introduction to optical probing tools for cold atoms is given in [126]. Among these, destructive absorption imaging is the most commonly applied method to image ensembles of ultracold atoms, which provides important information about the atom number N and the density distribution $n(x, y, z)$. Absorption imaging is also the standard imaging tool for all experiments throughout this thesis. In addition, we developed a new interferometric detection method making use of the dispersive interaction between atoms and light. In the following, we treat these two methods. For other techniques, like phase-contrast, dark ground or fluorescence imaging, we refer the reader to [126].

3.6.1 Absorption imaging

Absorption imaging bases on the idea to image the intensity profile of a resonant laser beam that has been partially absorbed by the atomic cloud. From the recorded light intensity profile, one can then deduce the column integrated atomic density $\widetilde{n}(x, y) = \int n(x, y, z)\, dz$. When passing the cloud, the intensity I of the imaging beam is reduced according to the law of Lambert-Beer:

$$\frac{dI}{I} = n(x, y, z)\, \sigma(z)\, dz\,, \tag{3.11}$$

where $n(z)$ is the particle density and $\sigma(z)$ the scattering cross section. In general, the scattering cross section depends on the light intensity and therefore on the position within the cloud via

$$\sigma(x, y, z) = \sigma_0 \frac{1}{1 + \frac{I(x,y,z)}{I_{\mathrm{sat}}} + \left(\frac{\omega - \omega_0}{\Gamma/2}\right)^2}\,. \tag{3.12}$$

Here, $\sigma_0 = \frac{3\lambda^2}{2\pi}$ is the polarization averaged scattering cross section of a closed imaging transition with resonance wavelength λ, saturation intensity I_{sat}, and natural linewidth Γ. The detuning of the probe laser frequency ω from the resonant transition frequency ω_0 is given by $\omega - \omega_0$. For imaging with resonant light, equation (3.11) can be exactly solved in the two limiting cases of low ($I \ll I_{\mathrm{sat}}$) and high ($I \gg I_{\mathrm{sat}}$) saturation.

Low saturation

At very low saturation ($I \ll I_{\mathrm{sat}}$), the scattering cross section becomes independent of the intensity, $\sigma(x, y, z) = \sigma_0$, which results in

$$I(x,y) = I_0(x,y) \cdot e^{-\sigma_0 \int n(x,y,z)\,dz} \,. \tag{3.13}$$

For absorption imaging during one experimental cycle, we typically take three pictures of the probe light intensity in series. The first corresponds to the actual absorption image I_{atoms}, where probe light has passed through the cloud, the second is a reference picture recording the intensity distribution I_{bright} of the probe beam without atoms present, and the third monitors the background I_{bg} in the absence of atoms and imaging light. From these images, we determine the relative transmission $T(x,y)$ for the further analysis:

$$t(x,y) = \frac{I_{\text{atoms}} - I_{\text{bg}}}{I_{\text{bright}} - I_{\text{bg}}} \,. \tag{3.14}$$

Experimentally, these different intensity distributions are mapped on the chip of a CCD (charged coupled device) camera by means of a lens imaging system with a certain magnification factor M. According to (3.13) and (3.14), the number of atoms, contained in the probe volume along the line of sight of one camera pixel of size A is then given by

$$N_{\text{pix}}(x,y) = -\frac{A}{\sigma_0 M^2} \ln\, t(x,y). \tag{3.15}$$

The quantity $-\ln\, T(x,y)$ corresponds to the optical density *OD* of the atomic sample which contains all information about the particle density.

High saturation

For a highly saturating imaging beam ($I \gg I_{\text{sat}}$), the scattering cross section can be approximated by $\sigma(z) = \frac{\sigma_0 I_{\text{sat}}}{I(z)}$, and equation (3.11) is solved by

$$I(x,y) = I_0(x,y) - I_{\text{sat}} \cdot \sigma_0 \int n(x,y,z)\,dz \,, \tag{3.16}$$

providing in a similar way the detected atom number per camera pixel

$$N_{\text{pix}}(x,y) = -\frac{A}{\sigma_0 M^2} \frac{I_0}{I_{\text{sat}}} (1 - T(x,y)). \tag{3.17}$$

Further information on experimental techniques for strong saturation absorption imaging of dense clouds of ultracold atoms can be found in [127].

Remarks on absorption imaging

Although analytical solutions exist for the two intensity limits, the exact determination of the atom number by means of absorption imaging is still delicate. Here, we summarize some remaining issues, in particular with respect to ^{6}Li:

- Typically, a quantum degenerate Fermi gases trapped in the FORT reaches a peak density of $10^{12} - 10^{13}$ atoms/cm^3, which makes *in-situ* measurements of the atom number rather susceptible to errors, even in the above cases of very low and high imaging intensities. In [128], critical values of the imaging intensities I_{crit} are given, beyond which the relative error between the measured and the actual atom number is lower than 5%. However, this error can usually only be kept small at the expense of a bad signal to noise ratio. For low saturation ($I_{\text{crit}} < 0.4 \cdot I_{\text{sat}}$), the optical density becomes so high that most of the photons are absorbed in the cloud. In contrast, high saturation ($I_{\text{crit}} > 25 \cdot I_{\text{sat}}$) results in low optical densities (<0.25) and hence in rather faint absorption images.
- In general, imaging of ^{6}Li atoms is more challenging and delicate than imaging of other alkali atoms. Due to its low mass, ^{6}Li atoms acquire a large recoil energy $E_{\text{recoil}} = \frac{\hbar k^2}{2\,m} = \hbar\,(2\pi \cdot 73.7\,\text{kHz})$ per scattered photon of the resonant wavelength $\lambda = 2\pi/k = 670.971\,\text{nm}$. Hence, by scattering only a few photons, the Doppler shift $\Delta\omega_{\text{DS}} = \frac{\hbar k^2}{m}(1 + \cos\theta)$ already drives the atoms out of resonance even for low saturation. Here, θ denotes the angle of the re-emission of a spontaneous photon in a random direction with respect to the imaging axis. In the experiments on density fluctuations presented in chapter 6, we apply absorption imaging with a light intensity equal to $(15 \pm 1)\%$ of the saturation intensity. In a simulation we could show that the Doppler effect then leads to a reduction of the absorption cross section to about 0.9, which has been necessarily accounted for in the data analysis.
- Alternatively, the density distribution can also be measured in time-of-flight, after ballistic expansion. However, this method only works for weakly interacting Fermi gases, because strong interactions preclude the sample from free ballistic expansion, but rather alter the density distribution during time of flight. Hence, there exists no analytical scaling expressions (see section 2.1.1) that allows to relate the experimentally accessible column density back to the in-trap three-dimensional density distribution [3, 126].

Summarizing the above remarks, we usually aim to perform absorption imaging of ^{6}Li at low saturation intensities. In order to attain a still reasonable signal to noise ration, we trade off shorter imaging times (illumination times) against higher imaging intensities.

3.6.2 Dispersive probing

In the previous discussion, we have only considered the absorptive part of atom-light interactions. A light field E_0 that enters and exists the atomic cloud does not only experience an attenuation t, but also acquires a phase shift ϕ due to the real part of the complex index of refraction. For weak probe light, both processes change the output light field E according to

$$E = t \cdot E_0 \cdot e^{i\phi}\,, \tag{3.18}$$

depending on the column density n_{col} as well as on the scattering cross section σ_0:

$$t = \exp\left(\frac{n_{\mathrm{col}}\sigma_0}{2}\frac{1}{1+s+4\delta^2}\right) \tag{3.19}$$

$$\phi = -\frac{n_{\mathrm{col}}\sigma_0}{2}\frac{2\delta}{1+s+4\delta^2} \tag{3.20}$$

Here, $\delta = \frac{\omega-\omega_0}{\Gamma}$ is the detuning of the laser in units of the linewidth Γ. On resonance, the imaging light is only absorbed and does not acquire a phase shift. In contrast, for an increasing detuning dispersion occurs while the imaged object becomes more and more transparent. Experimentally, we use a CCD camera to detect the scattered and unscattered light, which is only sensitive to the light intensity $\propto |E|^2$. In order to encode the information stored in the acquired phase shift, it has to be converted into intensity information which is the purpose of dispersive imaging. In general, any dispersive imaging technique aims to separate unscattered and scattered components of the probe light and to manipulate both independently. In phase-contrast [129, 130] and dark-ground [130] imaging, this separation is accomplished by spatially filtering both components in the Fourier plane of the imaging system. An overview of these two imaging techniques is given in [126]. Another method, so-called polarization-contrast imaging [131, 132] relies on the different phase shifts for orthogonal polarizations of the probing light. By placing a polarizer in the imaging path after the transmission through the atoms, both polarizations can first be separated and subsequently be re-combined to interfere with each other. The resulting interference signal eventually contains the desired information about the phase shift.

In chapter 7 of this thesis, we present a new interferometric imaging technique based on the principle of dispersive polarization-contrast imaging. As any other dispersive imaging, this method is advantageous because the amount of heat deposited into the atoms by the probing light is about 300 times lower than it would be the case for an equivalent absorption image. This huge decrease in heat transfer gives us the ability to repeatedly probe the atomic sample in a nearly non-destructive way.

3.6.3 Optical setup for standard imaging

Most of our experiments are performed at magnetic fields well above 150 G as there the tunability of the interparticle scattering length by external magnetic fields enters the experimentally most interesting regime (see Fig. 2.3). At these fields, ^{6}Li atoms are in the Paschen-Back regime, where the nuclear spin is completely decoupled from the electron spin. Typically, we work with a two-component quantum gas in an incoherent spin mixture of the two lowest lying hyperfine sub-states of the $F = 1/2$ manifold which differ only in the nuclear spin orientation m_I. For both ground states with $(m_s = -1/2, m_I = \pm 1/2)$, there exists an almost closed transition to the $m_j = -3/2$ state of the $2\,P_{3/2}$ excited state, preserving m_I. Due to the splitting of about 80 MHz between both ground states, which is moreover nearly constant over the full range of the Feshbach resonance, both spin states - denoted as $|1\rangle$ and

$|2\rangle$ - can be selectively addressed and imaged. The optical transition frequency of this σ^--transition varies by more than 1 GHz over the whole width of the Feshbach resonance (-1.4 MHz/G), from zero magnetic field to above 1100 G. For the imaging laser we thus use an offset lock that allows us to tune the imaging light over a range of 900 MHz (see section 3.3.1).

In the experiments throughout this thesis, we use two different imaging systems to probe the atomic ensemble at the final position in the glass cell. Both of them are sketched in Fig. 3.12. One is the high resolution imaging setup along the vertical axis, which employs one of the two high numerical aperture microscope objectives. This key feature of our apparatus will be separately addressed in chapter 4. Here, we will briefly describe our standard imaging system, probing the atomic cloud parallel to the x-axis in the horizontal plane. This imaging system consists of two achromatic lenses (f_1 = 100 mm and f_2 =150 mm) mapping the magnified image ($\sim \times 1.5$) of the homogenously illuminated atoms onto a CCD camera (*Point Grey, Flea2 Grasshopper*, pixel size 6.45 μm). The optical resolution of the imaging system has been estimated to be about $4 \pm 1\,\mu$m. The polarization of the imaging beam is chosen to be perpendicular to the homogeneous magnetic field generated by the Feshbach coils defining the quantization axis for the atomic system. This reduces the absorption cross section by a factor of two compared to a properly circular polarized beam along the quantization axis ($\sigma = \sigma_0 = 2$ in the low intensity limit).

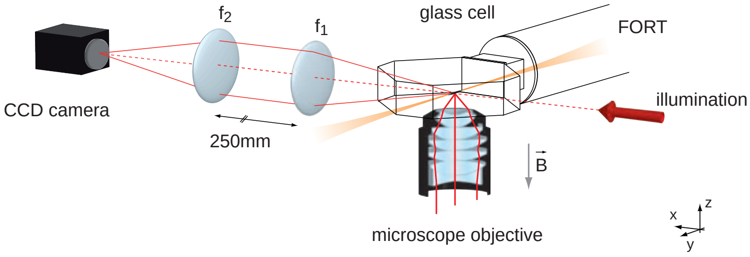

Fig. 3.12: A collimated imaging beam with a waist of about 1 mm homogenously illuminates the atomic cloud. In absorption imaging, this probe light, resonant with the lowest hyperfine state of the $|2S_{1/2}\rangle$ to $|2P_{3/2}\rangle$ transition, is collected by the two lens imaging system and mapped on the chip of the CCD camera. The microscope below the glass cell belongs to the high-resolution imaging setup described in chapter 4.

3.7 Experimental sequence towards quantum degeneracy

After having introduced the technology and methods employed in our apparatus, this section briefly summarizes the experimental procedure used to prepare the object under investigation of this thesis, an ultracold quantum gas of ^{6}Li atoms. In the first paragraph, we discuss the different stages of the experimental cycle step by step, and subsequently present the creation of a quantum degenerate Fermi gas as well as the formation of a molecular Bose-Einstein condensate.

3.7.1 Experimental cycle

In the introduction of this chapter, we have already roughly outlined the experimental cycle. The corresponding pictorial illustration is given in Fig. 3.1(a)-(d). The experiment is operated periodically with a cycle time of approximately 12 s. In each run, we prepare a new sample of ultracold fermions which is finally probed by optical means at the end of each cycle. The robust construction of the apparatus ensures a reliable and reproducible formation of the quantum gas from run to run, exhibiting only small fluctuations of the total atom number below 6% over several hours of operation. Each procedure in the experimental cycle is precisely controlled by several computers. In total, we use 32 analog and 64 digital output channels to synchronously operate all devices involved in the sequence. The employed software for the experiment and camera control was developed by our former group member Thilo Stöferle [133], which enables a clear and adaptable implementation of the experimental sequence and also an automatic data acquisition.

MOT loading Each experimental cycle starts with loading the magneto-optical trap (MOT): ^{6}Li atoms emanating from the oven with an initial velocity of about 1000 m/s are decelerated by the Zeeman slower below 70 m/s and subsequently captured in the MOT at the center of the main UHV chamber (see Fig. 3.1(a)). After 4 s of loading and cooling, the MOT typically contains 10^9 atoms at a temperature of about 200 μK, which is slightly above the Doppler limit of 140 μK for ^{6}Li.

Transfer from the MOT into the resonator trap The temperature limit of laser cooling is overcome by all-optical evaporative cooling. For this, the atoms in the MOT are transferred into the standing-wave optical dipole trap. The transfer efficiency of the atoms from the MOT into the standing wave optical dipole trap strongly depends on the final density and temperature achieved in the MOT. For the transfer, we thus apply a Doppler cooling scheme during the final MOT phase. After having switched off the Zeeman slower, the loading process of the MOT stops and we spatially compress the trapped atomic sample by detuning the cooler and repumper laser from -6.5 Γ to -2.0 Γ within 10 ms. At the same time, the intensity of the cooling laser is reduced to 40% of its initial value used for the MOT loading, while the repumper intensity is even further decreased to 0.2%. All values have been optimized experimentally to result in the best transfer efficiency. The difference in the final intensity levels of cooling and repumping light causes an optical pumping of the sample into the $F = 1/2$ manifold, which eventually is completed by driving the cooling transition for another 6 ms after the repumper has been switched off. This optical pumping is necessary since elastic collisions of atoms in the $F = 3/2$ state would otherwise significantly shorten the lifetime of the sample in the resonator trap. After this procedure, both $m_F = \pm 1/2$ states are populated with approximately equal probability. During the entire transfer process, the resonator is operated at its maximum trap depth of about $500\,\mu$K (MOT position). Under these conditions, we typically transfer up to $9 \cdot 10^7$ atoms from the MOT into the resonator trap.

Evaporative pre-cooling in the resonator trap In the resonator trap, the atomic sample is evaporatively pre-cooled: Using a first order exponential ramp (time constant $\tau = 1.5\,$s) of 2.5 s duration, the power of the injection light for the resonator is reduced to 20% of its initial value. During the evaporation, we apply a magnetic field of 300 G to set the s-wave scattering length for the interstate collisions between the two hyperfine sub-states $|1\rangle$ and $|2\rangle$ to -300 a_0, allowing an efficient re-thermalization.

Transfer from the resonator trap into the running wave dipole trap During the evaporative pre-cooling in the resonator trap, the running wave dipole trap (FORT), whose focal position overlaps with the atoms trapped in the resonator, is already turned on to the maximum trap depth of about $150\,\mu$K, corresponding to 3.5 W light power (see Fig. 3.1(b)). Consequently, the FORT is continuously loaded during the evaporation [134]. At the end of the evaporation ramp, the resonator is suddenly switched off and typically about 1.5×10^6 atoms in each sub-state have been transferred into the running wave optical dipole trap. We again like to note that loading the FORT directly from the MOT yields much lower numbers of transferred atoms and thus the employment of the resonator is indeed essential.

Optical transport into the glass cell For the transport into the glass cell, the magnetic Feshbach field in the main chamber is turned off, and the power of the FORT light is decreased to 2 W in order to reduce resonant light scattering. Finally, the atoms in the optical tweezer are transported into the glass cell by moving the lens mounted on the translation stage [107] (see Fig. 3.1(c)).

Forced evaporative cooling to quantum degeneracy At the final position in the glass cell, forced evaporation is performed by decreasing the power in the optical tweezer from 2 W down to a few mW (see figure 3.1(d)). For this, we use a first order exponential ramp of 2.5 s duration with a time constant of $\tau = 4\,$s. This procedure assures a fast and effective evaporation with a nearly constant $\eta \simeq 10$ [135, 136], where $\eta = U/k_\mathrm{B}T$ is defined by the ratio between the trap depth U and the temperature T of the sample in the trap. Depending on the magnetic field applied during cooling, the evaporation process either results in the formation of a quantum degenerate Fermi gas or a molecular Bose-Einstein condensate. In the following two paragraphs, we present the experimental demonstration of both.

3.7.2 Quantum degenerate, non-interacting Fermi gas

For the formation of a quantum degenerate, non-interacting Fermi gas, we apply a magnetic field of 300 G during the final evaporation, corresponding to a scattering length of -300 a_0 between state $|1\rangle$ and $|2\rangle$. When the final trap depth is reached, the atomic ensemble is allowed to thermalize for 160 ms. We then ramp the magnetic field to 528 G in 150 ms, where the scattering length is approximately zero [81]. At the same time the power of the trapping beam is slightly increased to avoid further particle losses due to free evaporation. This procedure finally results in the formation of a quantum degenerate Fermi gas of typically a few times 10^5 atoms in each of the two lowest hyperfine sub-states. For the determination of the particle number and final temperature, the atomic ensemble is released from the trap. After 1.5 ms of TOF, the expanded cloud is imaged by means of absorption imaging. As described in chapter 2.1.1, the total particle number and the temperature can be determined by fitting an appropriate function (see equation (2.7)) to the recorded column density. Fig. 3.13(a) and Fig. 3.13(b) show the absorption images (insets) and the vertically integrated column density distribution of the expanding Fermi gas for two different final evaporation levels. We intentionally chose low atom numbers for this measurement, achieving low optical densities, which justifies the assumption that the atomic column density is proportional to the optical density doing absorption imaging. Moreover, we approximate the Gaussian shape of the dipole trap by a harmonic oscillator, which is typically possible for these low atom numbers and temperatures. Therefore, equation (2.8) can be applied to determine the relative temperature T/T_F. The temperature of the sample shown in Fig. 3.13(a) is about 0.15 T/T_F, while it is 0.23 T/T_F in Fig. 3.13(b). Such an ultracold Fermi gas with nearly negligible interactions is the starting point for the investigation of density fluctuations in chapter 6.

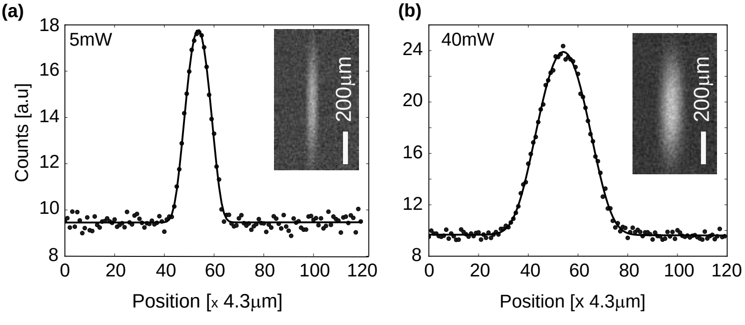

Fig. 3.13: (a)and (b): Vertically integrated density profiles of a non-interacting Fermi gas for two different evaporation levels, resulting from absorption images (insets) of the expanding atom cloud after 1.5 ms time of flight. The images only show one spin component, here state $|1\rangle$. From a fit (black line) according to equation (2.7), we obtain the corresponding atom numbers, which are 10,000 and 30,000 in (a) and (b), respectively.

3.7.3 Bose-Einstein condensate of molecules

Alternatively, a molecular Bose-Einstein condensate (BEC) of two composite fermions in the two spin states $|1\rangle$ and $|2\rangle$ can be created when the final forced evaporative cooling is performed near the Feshbach resonance of ^{6}Li, at a magnetic field of about 790 G. At this field, the inter-state scattering rate amounts to $9100\,a_0$. There, a large number of bosonic dimers are formed by three-body recombination. Note that three-body recombination in a two-component Fermi gas is actually expected to be strongly suppressed. However, it was shown that three-body recombination close to a Feshbach resonance nevertheless exists and scales like the sixth power of the scattering length [137], and thus is strongly enhancing the molecule production. During evaporation, the thermal energy of the atoms falls below the binding energy of the weakly bound molecules (see chapter 2.2.2), and the atom-molecule equilibrium favors the molecular state. These molecules are stable [75, 76, 138, 139], although the intermolecular scattering length is still large, being 0.6 times the value for free atoms [87]. In addition, the polarizability of the molecules is twice as large as compared to free atoms, and thus they experience twice the trap depth, whereas the trapping frequencies are the same for molecules and atoms. Hence, evaporative cooling first makes only free atoms to leave the FORT, while the molecules stay in the trap. Further reduction of the trapping potential leads to the evaporation of molecules and finally causes the bosonic molecules to condense into a molecular BEC when the phase space density exceeds unity [50, 51, 52].

Bose-Einstein condensation in dilute gases of weakly interacting particles can be theoretically treated in the framework of the Gross-Pitaevskii equation (GPE), a non-linear Schrödinger equation of the form

$$\left(-\frac{\hbar^2}{2m}\nabla^2 + V(\boldsymbol{r}) + gN_0|\psi(\boldsymbol{r})|^2\right)\psi(\boldsymbol{r}) = \mu\,\psi(\boldsymbol{r})\,. \tag{3.21}$$

Here, $V(\boldsymbol{r})$ denotes the external trapping potential, N_0 the total number of bosonic particles, μ the chemical potential, and $g = 4\pi a\hbar^2/m$ the coupling constant determined by the s-wave scattering length as defined in chapter 2.2. In general, the Gross-Pitaevskii equation is hard to solve and in most cases only numerical solutions can be found. However, the Gross-Pitaevskii equation can be simplified for systems with large particle numbers in which in addition the kinetic energy is negligible compared to the mean field interaction energy. For BECs of ^{6}Li$_2$ molecules of about 10^5 particles in our case, this so-called Thomas-Fermi approximation is reasonably applicable and yields

$$\left(V(\boldsymbol{r}) + gN_0|\psi_{\mathrm{TF}}(\boldsymbol{r})|^2\right)\psi_{\mathrm{TF}}(\boldsymbol{r}) = \mu_{\mathrm{TF}}\,\psi_{\mathrm{TF}}(\boldsymbol{r})\,, \tag{3.22}$$

which has the solution

$$n_{\mathrm{TF}}(\boldsymbol{r}) = |\psi_{\mathrm{TF}}(\boldsymbol{r})|^2 = \max\left(\frac{\mu_{\mathrm{TF}} - V(\boldsymbol{r})}{g}, 0\right) \tag{3.23}$$

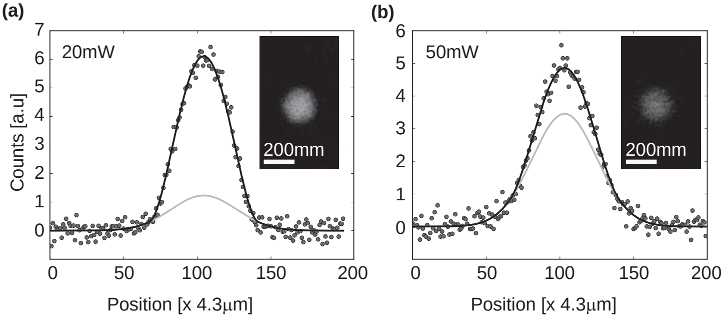

Fig. 3.14: Molecular Bose-Einstein condensation (a) and (b): Absorption image (insets) and vertically integrated column densities for two different final evaporations levels. In (a) the condensate fraction amounts to 0.72, whereas in (b) it is below 0.3. The absolute temperatures are 260 nK and 310 nK respectively. Note that both figures only reveal the absorption signal from one spin component, whereas the imaging transition frequency for the second component is detuned by about 80 MHz.

For an harmonic trapping potential, the density distribution of the BEC thus has the shape of an inverted parabola. Further information about the theory and also experimental aspects of Bose-Einstein condensation is given for instance in [72, 73].

One standard method for detecting the onset of Bose-Einstein condensation is the observation of a bimodal density distribution which the expanded cloud reveals after a certain time of flight (TOF): while the condensed fraction of molecules exhibits a parabolic profile, thermal, non-condensed molecules give rise to a Gaussian density distribution. From the ratio between both contributions, we can deduce the condensate fraction N_0/N, the number of condensed molecules N_0 and the temperature of the gas. In the experiment, the cloud is released from the FORT and expands at a magnetic field of 776 G, corresponding to a scattering length of 5900 a_0. The magnetic field has been reduced during TOF to decrease the mean field energy and thus the expansion of the condensed fraction which makes the bimodal distribution more pronounced. After a TOF of 3.5 ms, the molecules are resonantly imaged at the given magnetic field of 776 G. The corresponding column density profiles and absorption images for two different final trap depths are shown in Fig. 3.14(a) and Fig. 3.14(b). A bimodal fit (black line) yields the total atom number N, the condensate fraction N_0/N and the absolute temperature. Both distributions show a deviation from the thermal distribution (gray line) indicating partial condensation at different condensate fractions.

4 Microscope setup

Pursuing the object of this thesis to advance a local access to ultracold quantum gases, this and the following chapter are devoted to the main feature of our apparatus, the high-resolution optical system which is schematically illustrated in Fig. 4.1. Key element of this optical setup is a pair of identical, high-resolution microscope objectives facing each other above and below the glass cell. While the lower microscope objective allows to locally probe the trapped quantum gas with a maximum resolution of 660 nm, the upper microscope is an essential part of a versatile optical system used to generate microscopically tailored optical dipole potentials on the same length scale.

Here, we provide a detailed technical description of the microscope objectives and the supporting opto-mechanics. The remaining sections then focus on the experimental characterization of the optical performance, in particular on the precise determination of the optical resolution and the magnification of the high-resolution imaging system. The experimental realization of the optical micro-potentials as well as the preparation and detection of fermionic atoms trapped therein will be separately discussed in chapter 5.

Parts of this and the following chapter are published in [140]: B. Zimmermann*, T. Müller*, J. Meineke, T. Esslinger, and H. Moritz, 'High-resolution imaging of ultracold fermions in microscopically tailored optical potentials', *New Journal of Physics* **13**(4), 043007 (2011). *These authors contributed equally to the presented work.

4.1 Microscope objectives

The development of a microscope objective, which meets the demanded requirements listed in the general design considerations at the beginning of the previous chapter, needs a wide experience in optical engineering. This becomes immediately evident when looking at the various parameters that can be exploited to match all specifying demands. Already the multitude of different glass materials or the total number of involved lenses with different possible shapes suggest the size of the full parameter range. For this reason, we decided for a professional custom-made design, provided and manufactured by *SPECIAL OPTICS*.

4.1.1 Objective design

Each of the two identical, long-working-distance microscope objectives is based on a system of 7 lenses as depicted in Fig. 4.2(a). The infinite-conjugate configuration is designed for three operating wavelengths at 532 nm, 671 nm and 770 nm, correcting aberrations of all three wavelengths. Furthermore, the objectives are corrected for a view through the 4 mm thick quartz window of the glass cell. Each objective has an effective focal length of $f_{\mathrm{eff}} = 18\,\mathrm{mm}$, and covers a numerical aperture of $NA = 0.53$. This yields a theoretical diffraction limit of 650 nm (full-width at half-maximum, FWHM) for an imaging wavelength of 671 nm (see section 4.2.2). All optical surfaces are anti-reflection coated for the above wavelengths (reflectivity $<$ 0.75%) and additionally for 1064 nm (reflectivity $<$ 2%).

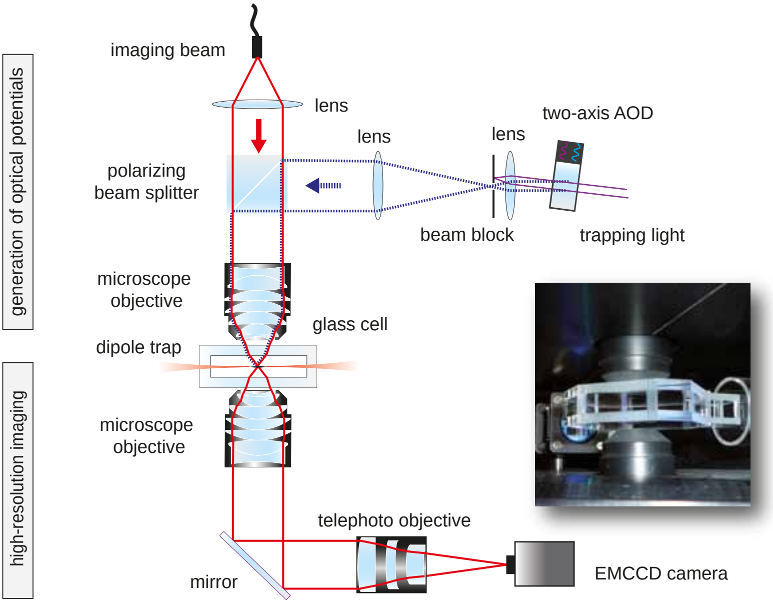
generation of optical potentials
high-resolution imaging
imaging beam
lens
lens
lens
two-axis AOD
polarizing beam splitter
beam block
trapping light
microscope objective
glass cell
dipole trap
microscope objective
telephoto objective
mirror
EMCCD camera

Fig. 4.1: Two identical microscope objectives represent the heart of the high-resolution optical system: The microscope objective below the glass cell and the telephoto objective belong to the high-resolution imaging setup. Probe light, resonant to the $|2S_{1/2}\rangle$ to $|2P_{3/2}\rangle$ transition of ^{6}Li, is collected by the microscope objective and imaged on an electron-multiplying CCD camera (EMCCD). The second microscope objective is part of the optical system for generating arbitrary optical micro-potentials. A two-axis acousto-optical deflector generates several, far off-resonant laser beams in a programmable way. Each of those beams is focussed by the microscope objective, resulting in a controllable pattern of multiple optical tweezers in the focal plane. The inset shows a real photo of the glass cell with the two microscope objectives.

The lens system is mounted in a custom-made housing manufactured from Ultem 2300 (see Fig. 4.2(b)). The fiber-enforced plastic material is non-magnetic and non-conducting, thus ensuring an undisturbed operation of the microscopes in the vicinity of the magnetic coils around the glass cell. Both, the fabrication of the housing as well as the mounting of the lenses was carried out by *SPECIAL OPTICS*. The assembling of all parts requires extraordinary accuracy for a maximum performance, for which reason a test specimen of the glass cell window was also involved during the assembly of the objective. The relative position of all lenses is fixed by precisely fabricated spacers in between, while the whole lens stack is clamped into the housing by a retaining ring.

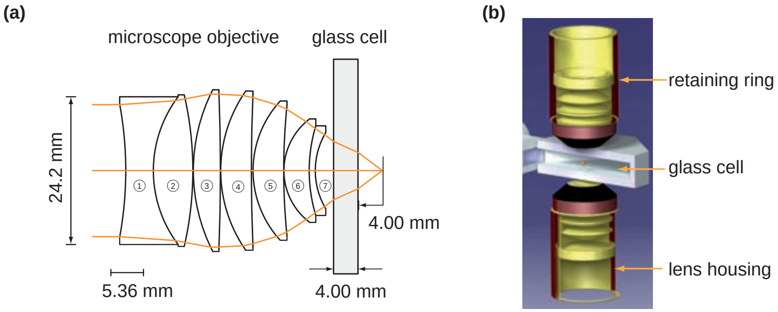

Fig. 4.2: Design and housing of the microscope objective. (a) Sectional drawing of the lens stack, reflecting the dimensions of the microscope objective and its close distance to the glass cell window (shortest distance 1.5 mm). The orange lines indicate the beam trace when exploiting the full numerical aperture of $NA = 0.53$. Lenses 2 to 5 are made of CaF_2, whereas lens 1 consists of O-S-BSM81 and lens 7 of SFL56 (b) Sectional model of the non-magnetic lens housing and the glass cell, showing details on the mounting of the 7 lenses with spacers and a retaining ring.

4.1.2 Objective mounting

We achieve the specified maximum optical performance at the diffraction limit (RMS wavefront error $< 7\%$ of the wavelength) by an accurate alignment of each microscope objective. From a ray tracing simulation with *OSLO (Optics Software for Layout and Optimization, Lambda Research)*, we computed the required constraints for the absolute position accuracy. According to the simulation, the constraints only allow a displacement from the optical axis by less than 1 mm, a de-focussing smaller than $3\,\mu$m, and a tilt of the microscope axis with respect to the normal of the glass cell below $0.1°$. To meet these conditions, the mounting of the microscope objective includes a coarse and fine adjustment along five axes. The tilting along two perpendicular axes can be adjusted with a goniometer (*NEWPORT, M-TTN80*) without altering the height of the mount along the central axis. This tilt platform has a centrical aperture with an inside thread holding the microscope tube made of machinable glass-ceramic (*MACOR*). This thread permits a coarse focussing of the microscope objective in axial direction (750 μm per revolution). The transverse coarse adjustment is performed by a two-axis translation stage (*OWIS, KT90*), also with a centrical aperture. For the fine adjustment in transverse and axial direction, we use a compact, piezo-driven three-dimensional translation stage (*Piezo Jena, Tritor 102 SG EXT*) with a maximum translation distance of 100 μm and a resolution of 3 nm. This device includes a strain gauge to measure the absolute position along each axis. Via a digital proportional-integral controller based on a field programmable gate array (*National Instruments, NI 9264/9205/9401*) [123, 124], the error in position is

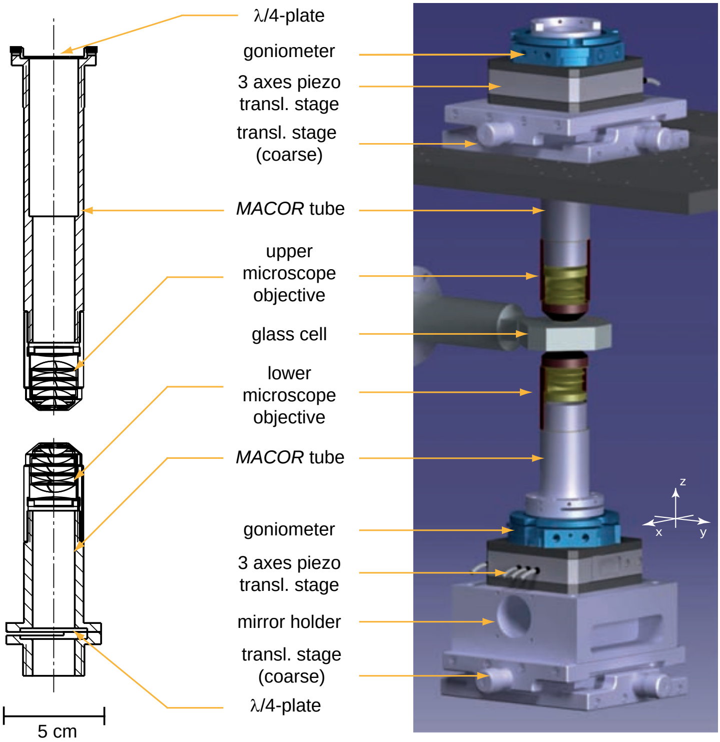
λ/4-plate
goniometer
3 axes piezo transl. stage
transl. stage (coarse)
MACOR tube
upper microscope objective
glass cell
lower microscope objective
MACOR tube
goniometer
3 axes piezo transl. stage
mirror holder
transl. stage (coarse)
λ/4-plate
5 cm
z
x
y

Fig. 4.3: Opto-mechanics of the microscope objectives: The left figure is a sectional drawing of the microscope objectives attached to the respective ceramic holding tubes. Both tubes support $\lambda/4$ retardation plates (*LENS-Optics*, multiple order, free aperture 28 mm) to change the polarization of the probe and trapping light. The lower *MACOR* tube consists of two parts to facilitate the installation of the microscope (see appendix E). The right figure is an isometric view of the full opto-mechanics involved to mount the microscopes. Not shown are the magnetic coils below and above the glass cell.

fed back to the piezo stage to actively stabilize the transverse and axial position of the setup. The passive stability of the goniometer is sufficient to keep the tilt angles within the constraints.

4.2 High-resolution imaging

The new apparatus presented in this thesis offers for the first time the ability to observe an ultracold atomic Fermi gas on a sub-micron length scale, an experimental challenge which to our knowledge has only been met for bosonic systems so far. The employed high-resolution imaging system is sketched in the lower part of Fig. 4.1, underneath the glass cell. It consists of three components along the optical axis: The lower microscope objective, a telephoto objective and an electron-multiplying CCD camera (EMCCD). In the following, we first give a brief description of the telephoto objective and the CCD camera, followed by the characterization of the high-resolution imaging setup.

4.2.1 Optical setup

Fig. 4.1 illustrates the configuration of the different components involved in the high-resolution imaging setup. Probe light coming from above is collected by the microscope objective, reflected by a 2" mirror (high-reflective for 532 nm, 671-780 nm, and 1064 nm) into the horizontal plane and finally focussed onto the CCD camera by the telephoto objective. This special configuration, in particular the employment of the telephoto objective, helps to meet two opposing demands on the imaging system: a high magnification factor on the one hand, and sufficient geometrical stability on the other hand. By definition, the theoretical magnification factor of a microscope setup is given by the ratio of the focal lengths of the imaging ocular and the microscope objective. With an effective focal length of 18 mm for the microscope objective, the demanded magnification implies a focal length of at least 720 mm. However, such a long focal length of the ocular may impair the pointing stability of the projected image on the CCD camera from shot to shot, which in contrast is indispensable as our measurements in many cases rely on a high reproducibility of repeated data acquisition. This issue is overcome by the telephoto objective which produces an effective system focal length longer than the back focal distance [141]. While the effective focal length defines the magnification, the back focal distance determines the separation between the telephoto objective and the detection device (camera). In our setup, the microscope objective is mounted 1.2 mm below the glass cell, followed by the telephoto objective at a distance of about 430 mm. The EMCCD camera is placed in the focal plane of the telephoto objective, about 450 mm (back focal distance) behind its last lens.

Telephoto objective

The telephoto objective was also designed and fabricated by *SPECIAL OPTICS* which allowed the optical engineer to model the telephoto objective for an optimum joint operation with the microscope objective at the diffraction limit. A sectional drawing of the telephoto objective is given in Fig. 4.4. The infinite-conjugate 3-lens design has an effective focal length of 975 mm and also corrects aberrations at the wavelengths of 532 nm, 671 nm and 770 nm. Similar to the microscope objectives, the 3 lenses are mounted in a non-magnetic and non-conducting housing (Ultem 2300) using spacers and a retaining ring. All lens surfaces are AR-coated for the same wavelengths as the microscope objective.

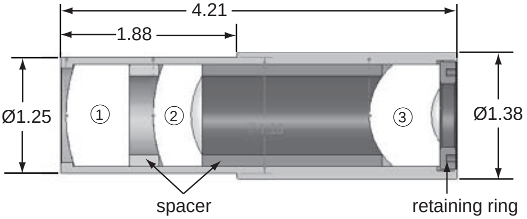

Fig. 4.4: Cross-sectional drawing of the telephoto objective. The given numbers indicate length scales in units of inch. Lenses 1 and 3 are made of CaF_2, and lens 2 of SF6.

The constraints for the accurate alignment of the telephoto objective are less restrictive than for the microscope objective. Without significant reduction of the resolution, the adjustment of the telescope objective tolerates a tilt angle of ±0.5° and a displacement of ±1 mm, both with respect to the main optical axis. The axial position is even less critical. Here, a de-focussing of 60 mm towards the microscope objective and 30 mm towards the camera are still within the constraints. For the alignment of the telephoto objective, we use a 4-axis positioner (*SPECIAL OPTICS, Mod. 60-10-100*) and a linear translation stage for the focussing in axial direction (*NEWPORT, Mod. M-UMR12.40A*). Due to the less restrictive constraints, the passive stability of the opto-mechanics for the telephoto objective is sufficient.

EMCCD camera

For the detection of the imaging light, we use a back-illuminated EMCCD camera (*ANDOR, iXon 897*, quantum efficiency > 0.9). Due to the magnification factor of about 54 (see next section), each pixel ($16\,\mu\text{m} \times 16\,\mu\text{m}$) thus corresponds to about $300\,\text{nm}\times300\,\text{nm}$ in the object plane. Using the electron multiplier detected signals on the level of a few incoming photons are amplified well above the read-out noise of the CCD camera.

4.2.2 Optical performance

The optical performance of the imaging setup was characterized in a separate test setup similar to the original setup in Fig. 4.1. Here, the glass cell was replaced by two specimen of the glass cell window, mounted with exactly the same separation as the top and bottom plate of the glass cell. Right in between the two glass windows, we mounted a test target that enabled us to determine the magnification and the resolution of the imaging setup, i.e. the combination of microscope objective and telephoto objective. As test target we used a gold foil grating consisting of holes with a diameter of 650 nm and a relative distance of 20 μm, which we got on loan from the group of M. Oberthaler, Heidelberg. A SEM (scanning electron microscope) micrograph of the target can be found in [142]. For the characterization of the microscope setup, we homogeneously illuminated the gold foil with laser light at $\lambda = 671$ nm from above and analyze the recorded images of the hole pattern.

Magnification

Theoretically, the magnification factor M of our microscope system is defined by the ratio between the effective focal lengths of the telephoto objective $f_{\text{tele}} = 975$ mm and the microscope objective $f_{\text{mic}} = 18$ mm,

$$M = \frac{f_{\text{tele}}}{f_{\text{mic}}} \simeq 54.2\,. \tag{4.1}$$

Experimentally, we determined the magnification by fitting the hole pattern in the image of the gold foil with a multiple-spot 2D Gaussian function yielding the hole separation in the image ($(1080 \pm 4)\,\mu$m). Comparing this value with the SEM measurement of the separation in the actual object ($(20 \pm 0.04)\,\mu$m) [142], we obtain a magnification factor of 54.0 ± 0.2, in good agreement with the estimated value.

Resolution

Physically, the resolution of our imaging system is fundamentally limited by diffraction. Even a point-like object gives rise to a blurred image which corresponds to the specific diffraction pattern known as Airy disk. In general, the resolution of an imaging system is defined by the minimum distance between two points at which they are still distinguishable in the image. Various criterions can be found in literature quantifying the definition of 'spatially distinguishable' in different ways. Most commonly, the Rayleigh criterion is applied. According to this, two adjacent point-like sources at distance Δr are still resolvable when the first minimum of the Airy disc in the diffraction limited image of one source coincides with the maximum of the other. The Rayleigh criterion directly connects the resolution Δr to the numerical aperture NA of the imaging system and the imaging wavelength λ [141]:

$$\Delta r_{\text{Rayleigh}} = 0.61\,\frac{\lambda}{NA}\,. \tag{4.2}$$

The manufacturer specified the NA of our imaging system to be 0.53, yielding a theoretical resolution of about $\Delta r_{\text{Rayleigh}} = 770\,\text{nm}$ at a wavelength of 670 nm. Experimentally, the gold foil test target allows a convenient way to determine the actual resolution of the imaging system. Since the diameter of the holes is smaller than the expected optical resolution, a single uniformly-illuminated hole can be considered to be a point-like light source. Assuming aberration free imaging, Fourier optics [143] states that the diffraction limited image of a given object corresponds to the convolution of the object with the so-called point spread function (PSF) of the imaging system. For a diffraction limited imaging system, the latter can be expressed in terms of the first order Bessel function $J_1(r)$ containing the resolution $\Delta r_{\text{Rayleigh}}$ as argument:

$$\mathrm{PSF}(r) = \frac{2\ J_1\left(1.22\pi \frac{r}{\Delta r}\right)}{1.22\pi \frac{r}{\Delta r}}\,. \tag{4.3}$$

We determine the resolution of our imaging system comparing the real image of a single hole in the gold foil with a simulation of the expected image [142]. The real image is taken with the imaging system focussed onto the target. Experimentally, the exact focal position follows from a Gaussian fit to the intensity distribution of the imaged hole upon variation of the axial positions of the microscope objective. The axial position related to the smallest fitted waist identifies the correct focussing of the microscope. For the simulated image, we approximate the hole in the gold foil by a circle with a diameter of 650 nm, and then do a coherent convolution of the circle with the Airy-like PSF given in (4.3). Subsequently, we calculate the RMS (Root Mean Square) deviation between the real and simulated image. Thereby, we vary the assumed resolution of the PSF as well as the relative position of the overlap between both images. The optimum combination of position and resolution showing the smallest RMS deviation determines the resolution. For our imaging system, this two-dimensional best-fit analysis yields a maximum resolution of $780 \pm 5\,\text{nm}$ at a wavelength of $\lambda = 671\,\text{nm}$. This is also in very good agreement with the expected value for a diffraction limited imaging system according to the Rayleigh criterion equation (4.4).

The FWHM (full-width at half-maximum) criterion defines the resolution in a different way than the Rayleigh criterion. Here, the resolution is defined by the minimum FWHM spot size resulting from the diffraction limited imaging of a point-like source. It is given by

$$\Delta r_{\text{FWHM}} = 0.5145 \frac{\lambda}{NA} \tag{4.4}$$

Applying this definition, our imaging systems offers a maximum resolution of about 660 nm (FWHM) for a wavelength of 671 nm. Expressing the resolution in terms of the FWHM criterion enables a direct comparison to [6] and [7].

Depth of field

With the focussing procedure for the microscope as described above, it is also possible to deduce the depth of field of the imaging system. This procedure yields the Gaussian waist fitted to the image of a single hole as a function of the axial position of the microscope objective. Due to the well calibrated strain gauge of the piezo translation stage, the relative position of the microscope objective can be expressed in absolute units of micrometers. As a standard, the depth of field is defined as twice the range in which the fitted waist is increased by a factor of $\sqrt{2}$. For our imaging system, this amounts to about $3.5\,\mu$m at maximum resolution. At the expense of a reduced resolution, the depth of field can be increased by artificially decreasing the numerical aperture of the imaging system. We typically do this by putting an iris in between the microscope objective and the telephoto objective.

Chromatic shift

We also measured the chromatic axial focal shift for the three operating wavelengths by determining the corresponding focal position of the microscope for each wavelength. We obtained an overall chromatic axial focal shift below 500 nm.

Field of view

According to the specifications of the manufacturer and verified by a computational ray trace analysis, our high-resolution imaging system spans a field of view of $100\,\mu\text{m} \times 100\,\mu$m. Here, this number is physically motivated by the contrast and defined as the region in the object plane, in which a sharp picture of the object is acquired. Due to the finite size of the CCD chip (512×512 pixels, pixel size $16\,\mu$m) and the large magnification, the region of the object plane which is captured by our optical

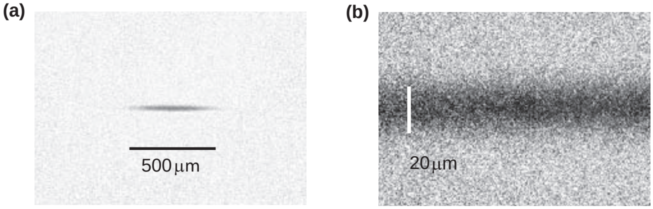

Fig. 4.5: (a) Standard absorption image of the in-trap density distribution of a non-interacting Fermi gas confined in the FORT. The magnified ($\sim \times 1.5$) picture is recorded with the imaging system along the x-axis of the experiment (see Fig. 3.12), offering a resolution of the order of $4\,\mu$m. (b) *In-situ* image of an identical prepared cloud, taken through the microscope along the z-axis with a magnification factor of 54 and a spatial resolution of about 700 nm. In both images, the black/white bars indicate absolute length scales in the object plane.

system is limited to $150\,\mu\mathrm{m} \times 150\,\mu\mathrm{m}$. As a result, our microscope imaging setup only records a small sub-part of the full atom cloud. When it is trapped in the FORT, the cloud typically has an extension of $20 - 30\,\mu m$ in the radial direction and about $500\,\mu m$ in the axial direction. Fig. 4.5 illustrates this situation. There, we contrast a standard absorption image of a trapped, non-interacting Fermi gas (a), recorded by the setup shown in Fig. 3.12, with a high-resolution *in-situ* image as seen through the microscope setup (b). These kind of highly resolved absorption images of the in-trap density distribution will be investigated in chapter 6 to deduce the density fluctuations of a weakly interacting Fermi gas.

5 Microscopically tailored optical potentials

It is due to the development of sophisticated tools and techniques to manipulate the external degrees of freedoms that by now ultracold atoms have become one of the best controllable quantum systems. In particular, appropriate methods for the storage and trapping of particles play a crucial role as the confinement directly influences the atomic motion and also the dimensionality of a system. In particular, optical traps have proven to offer versatile opportunities to control and manipulate atomic quantum gases. Among those, optical lattices constitute a very prominent and successful example [32, 34]. As pointed out in the introduction of this thesis, ultracold atoms in optical lattices have paved the way into the strongly interacting regime and moreover provide an almost ideal experimental realization of the Hubbard model with highly tunable parameters [35]. Very recently, even single site resolution imaging has been achieved for bosonic systems [7, 36, 37]. Yet, the concept of optical lattices created by interfering laser fields is by design restricted to the investigation of periodic systems with a high degree of symmetry. Various approaches towards more flexible and locally controllable geometries for optical potentials have been reported, for example double wells [144, 145], ring traps [146, 147], ring lattices [147, 148], box potentials [149] and finite lattice patterns [147, 148, 150]. Most of these realizations technically employ special optical devices to shape and deflect Gaussian laser beams such as phase plates [151], acousto-optical deflectors [147] and spatial light modulators [146]. However, most realizations so far still lack the ability to shape optical potentials on length scales comparable to the interatomic distance. Hence, tunneling processes and dynamics are correspondingly very slow. In addition, all experiments mentioned above have been performed with bosonic atoms, and to our knowledge, experiments with fermions have not been reported yet.

Here, we present the first experimental realization of ultracold fermions in microscopically tailored optical potentials. The key tool for this is the upper part of our high-resolution optical system which employs one of the microscope objectives and a two-axis acousto-optical deflector. In the following, we first describe the basic concept and the experimental setup used to create static as well as time-averaged optical dipole potentials on the sub-micrometer length scale. We then demonstrate the site-by-site creation and characterization of several trapping geometries including a tightly focussed single optical dipole trap, a 4x4-site two-dimensional optical lattice and a 8-site ring lattice configuration. In the last part, we show the ability to load and detect a small number of fermions in these projected trapping potentials.

5.1 Generation of optical micro-potentials

5.1.1 Basic concept

Like in other work [147, 148, 152, 153], we employ a two-axis acousto-optical deflector (AOD) to tailor optical dipole potentials. In principle, the AOD deflects and frequency shifts a red-detuned laser beam proportional to the radio-frequency (RF) fed into the AOD, while at the same time the beam intensity can be controlled via the amount of applied RF power. The deflected beam - enlarged by telescope optics - is then focussed by the upper microscope objective to form a single, small volume optical dipole trap with a waist on a sub-micron length scale.

Different deflection angles caused by different RF input frequencies result in different positions of the tweezer in the focal plane of the microscope objective because the latter works as a Fourier transformer. The speciality of a two-axis AOD is that it is able to deflect the tweezer along two orthogonal axes and, moreover, can be driven by multiple RF frequencies along each axis at the same time. Doing so, a bunch of laser beams, resulting from the convolution in the two-dimensional deflection process, leaves the AOD, and gives rise to versatile two-dimensional multiple spot patterns in the focal plane of the microscope. Fig. 5.1 illustrates this principle, showing the formation of a 2x2 tweezer system overlapped with a trapped cloud of cold atoms. Alternatively, a single tweezer can be rapidly scanned in the focal plane of the microscope which allows to - nearly literally taken - paint arbitrary time-averaged trapping potentials in two dimensions. In section 5.2 we demonstrate experimental examples of both, static as well as time-averaged potentials.

5.1.2 Optical setup

The optical setup used to create the micro-potentials is depicted in the upper part of Fig. 4.1, above the glass cell. In detail, we use a two-axis deflector from *IntraAction Corp.* (*Model A2D-603AHF3A*, center frequency 60 MHz, 3 mm aperture) which incorporates a special acoustic phased-array beam-steering design in order to maintain a uniform diffraction efficiency (80%) across the deflection bandwidth of 30 MHz (values for operation on only one axis). Additionally, the short access time (∼276 ns/mm beam diameter) of the AOD readily allows for time-averaged potentials. As a RF-source we employ a *Universal-Software-Radio-Peripheral-2* (USRP-2), a computer-hosted hardware originally intended to make software radios. It is controlled via the *gnuradio software* [154, 155] and enables a flexible generation of arbitrary wave forms with a bandwidth of 25 MHz around a central frequency (60 MHz). A detailed description of the design will be presented in the PhD-thesis of my co-worker J. Meineke [156], who set up the USRP-2 system for our experiment.

As trapping light, we use red-detuned light at a wavelength of 767 nm, provided by a tapered amplifier laser. A collimated beam at this wavelength, with a waist of 1.2 mm, enters the AOD and is deflected into the (-1$^{\text{st}}$/-1$^{\text{st}}$)-order for each applied RF frequency. Subsequently, the deflected beams are expanded by a two-lens telescope to a maximum waist of 12.5 mm to exploit the full numerical aperture of the optical system. The microscope objective finally focusses each of these collimated beams to a diffraction limited spot size of about 730 nm. Using the opto-mechanical mounting for the microscope objective described in section 4.1.2, the resulting micro-trap pattern can be precisely aligned and position-stabilized onto the atomic sample in the transport dipole trap (see Fig. 4.1), which serves as a reservoir to load the micro-traps.

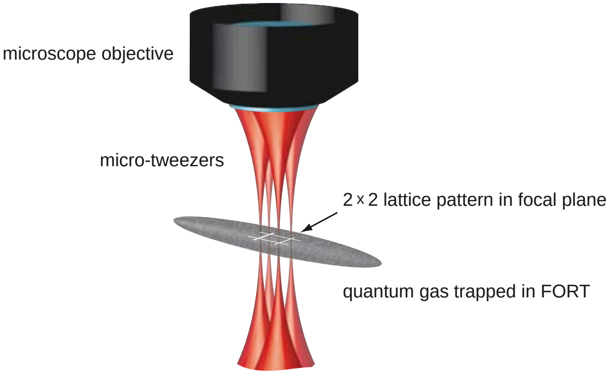
microscope objective
micro-tweezers
2 x 2 lattice pattern in focal plane
quantum gas trapped in FORT

Fig. 5.1: Basic principle to create multiple-spot micro-traps exemplarily demonstrating a square lattice configuration. A two-axis acousto-optical deflector provides four laser beam that are focussed by the microscope objective to form a 2x2 array of optical tweezers. By overlapping these tweezers with a cold atomic cloud trapped in the FORT, the micro-trap pattern can be loaded with atoms. Note: This illustration is not to scale. In particular, due to the high numerical aperture of the microscope objective, the strongly focussed beams diverge in a much stronger way than it is drawn. Depending on the relative separation, the individual beam profiles may already overlap within the atomic cloud.

5.2 Optical micro-potentials

As a unique feature of our optical system, the special configuration of the two identical microscopes in line allows us to directly monitor the optical potential landscape. In particular, the high-resolution imaging setup below the glass cell accurately maps the position, dimensions and intensity distribution of the trapping light pattern shaped by the optical setup above the glass cell. Using this information, we are able to characterize the trap geometry in terms of waists, spacings, trap depths and trap frequencies. Moving the imaging setup out of the focus of the upper microscope also provides insight into trap parameters along the beam propagation direction. In the following we exemplarily demonstrate the characterization of a single spot Gaussian micro-trap.

5.2.1 Single spot micro-trap

Fig. 5.2(a) shows the focal, two-dimensional intensity distribution of a single spot created by the upper microscope and imaged with high resolution onto the EMCCD camera by the lower microscope. Fitting a Gaussian function to the measured intensity profiles along the x- and y-axis yields a spot size with a waist ($1/\mathrm{e}^2$-radius) of $w_x = 734\,\mathrm{nm}$ and $w_y = 726\,\mathrm{nm}$, respectively (see Fig. 5.2(b)). By moving the imaging system along the beam propagation direction we measure the longitudinal intensity profile which allows us to extract the Rayleigh length of the micro-trap. For the given example in Fig. 5.2(a), we obtain a Rayleigh length of $\sim 2.1\,\mu\mathrm{m}$.

With these parameters and a light power of $0.1\,\mathrm{mW}$, an optical dipole trap with a calculated depth of $18.6\,\mu\mathrm{K}$ for $^6\mathrm{Li}$ atoms is created (see equation (3.8)). The bottom

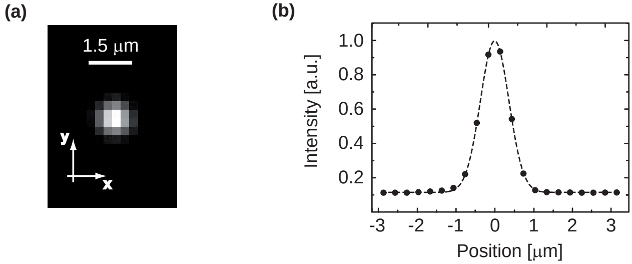

Fig. 5.2: (a) High-resolution image of a single-spot dipole trap in its focal plane (wavelength 767 nm), illustrating the capability of the optical system to map and characterize the optical potential landscape. For the imaging, a bandpass filter for 671 nm light in front of the CCD camera is removed which normally blocks the trapping light in the infra-red (767 nm) when only the atoms trapped in the optical potential are to be imaged. (b) Intensity profile of the single spot along the x-axis. A Gaussian fit to the two-dimensional intensity distribution yields the corresponding waists of the micro-trap.

of such a Gaussian trap is well approximated by a harmonic potential up to about 20% of the trap depth. Doing so, the corresponding trapping frequencies for the above example amount to $\omega_x = 2\pi \cdot 69.5\,\text{kHz}$ and $\omega_y = 2\pi \cdot 70.2\,\text{kHz}$ in radial direction, and $\omega_z = 2\pi \cdot 16.5\,\text{kHz}$ along the axial confinement. The total number of states in a harmonic trapping potential at zero temperature with energy less than ε is given by $G(\varepsilon) = \frac{1}{6}\frac{\varepsilon^3}{\hbar^3 \omega_x \omega_y \omega_z}$ (see for example [72]). According to this, for 0.1 mW light power the single-spot dipole trap only offers approximately one available state up to the energy level equal to 20% of the trap depth. Experimentally the situation is different. When we load atoms into the micro-potential (see section 5.3), nearly all energy levels up to the edge of the trap depth are populated, where the density of states is strongly increased. For the given parameters, an interpolating expression [122] for the number of single particle eigenstates of a Gaussian trap yields about 700 available states up to 99% of the trap depth.

5.2.2 Multiple spot micro-traps

Fig. 5.3 and Fig. 5.4 illustrate a selection of possible multiple-spot potential patterns realized with our setup. The first one represents an example for a static micro-trap system, whereas the latter is due to a time-averaged projection of two static configurations. In both cases, the presented images are again direct maps of the potentials in their focal plane, imaged onto the EMCCD camera.

Two-dimensional finite optical lattice

Applying four RF frequencies to each axis of the 2D AOD at the same time results in a static 4x4 beam diffraction pattern in the (-1$^{\text{st}}$/-1$^{\text{st}}$)-diffraction order. In the focal plane of the upper microscope, this pattern yields a square array of 4x4 dipole traps, realizing a finite-size, two-dimensional optical lattice system. In particular, this lattice configuration is homogeneous, in contrast to optical lattices created by interfering laser beams, for which the Gaussian profile of the interfering laser beams gives rise to an extra overall confinement. Often, this additional confinement causes challenges in the comparison between theory and experiment. In Fig. 5.3(a), we present the experimental realization of a static 4x4-site square lattice configuration. In detail, the four applied RF frequencies are symmetrically arranged around the center frequency of 58 MHz, separated by 7 MHz. In real space, this corresponds to a lattice site separation of approximately $3\,\mu$m in the focal plane.

Smaller lattice spacings can be achieved with smaller RF frequency separations (see Fig. 5.3(b-e)). Due to the spatial resolution of the imaging system, we are able to resolve lattice spacings down to one micrometer as can be seen in Fig. 5.3(e). The spacing can be changed dynamically even during one experimental cycle, thus enabling for instances the tuning of tunneling dynamics within one experiment. Increasing the number of applied RF frequencies easily enlarges this two-dimensional lattice pattern to a maximum size of 8x8 sites, limited by the finite RF deflection bandwidth of the AOD.

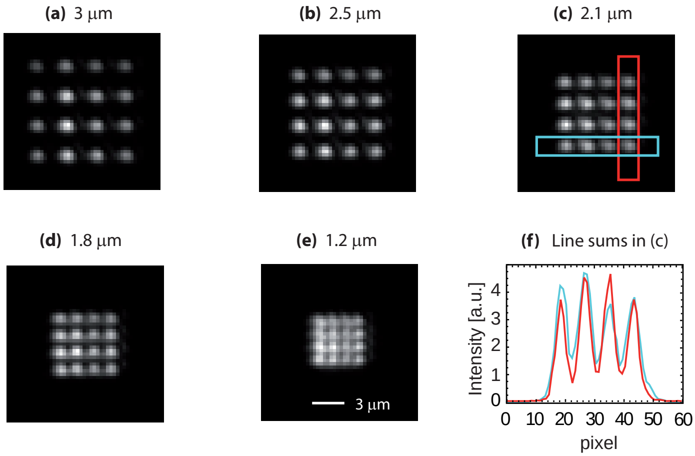
(a) 3 μm

(b) 2.5 μm

(c) 2.1 μm

(d) 1.8 μm

(e) 1.2 μm

(f) Line sums in (c)

Fig. 5.3: High-resolution images of a 4x4 site 2D lattice configuration with different lattice spacings: (a) 3 μm, (b) 2.5 μm, (c) 2.1 μm, (d) 1.8 μm, and (e) 1.2 μm. Each lattice site has a Gaussian spot size of approximately 800 nm (1/e^2-radius). This spot size is slightly larger than for the single spot shown in figure 5.2 since here, as well as for the ring lattice shown in figure 5.4, the numerical aperture of the upper microscope was reduced facilitating the alignment for this first demonstration. (f) Vertical and horizontal line sum profiles of the selected region in (c), marked in blue and red, respectively. The partial inhomogeneity in the intensity of different lattice sites results from an inhomogeneous diffraction efficiency within the RF bandwidth of the two-axis AOD. This inhomogeneity can be minimized, since the RF power for each RF frequency can be individually controlled, independently for both axes.

The tunneling rates for ^{6}Li atoms populating the lowest Bloch band of the lattice pattern can be estimated using [157]. For this, we approximate the 4x4 spots by an appropriate two-dimensional sinusoidal potential whose periodicity λ_{latt} corresponds to the spot separation. According to [157], the tunneling rate t to a nearest neighbor lattice site is given by

$$t = \frac{4}{\sqrt{\pi}} V_0^{3/4} \exp\left(-2\sqrt{V_0}\right) , \tag{5.1}$$

where V_0 corresponds to the lattice depth in units of the lattice-related recoil energy $E_{\text{recoil}} = \frac{h^2}{2m\lambda_{\text{latt}}^2}$. For the given configuration in Fig. 5.3(e), with a lattice spacing of 1.2 μm and 10 μW light power per lattice site, equation (5.1) predicts a tunneling rate of about 800 Hz. In combination with the ability to tune the interparticle interactions via Feshbach resonances, these already substantial tunneling rates provide a prospect for the realization of Hubbard-model like physics in such finite-size, homogenous lattice systems.

Ring lattice

Apart from static potentials, our setup also enables the generation of time-averaged optical potentials by alternately projecting different trapping geometries onto the atoms. For this, the switching rate between the different trap configurations has to exceed the corresponding trapping frequency significantly in order to display a static trapping potential for the atoms. In Fig. 5.4, we give an example of such a time-averaged optical potential. Here, we switch periodically with a frequency of 500 kHz between two different rectangular 2x2 lattice configurations. This results in a 8-site ring lattice structure as schematically depicted in Fig. 5.4(a). Fig. 5.4(b) presents the realization of this ring lattice with our setup, showing the corresponding light intensity distribution in the focal plane. In the given case, the ring diameter measures $\sim 6.9\,\mu$m with an approximate spot size of 800 nm for each lattice site. This value is slightly above the achievable minimal spot size, as we did not use the full numerical aperture of the optical system for the given example. As demonstrated for the square lattice configuration in the previous section, the site separation in the ring lattice can also be controlled arbitrarily down to about one micrometer, which is not shown here.

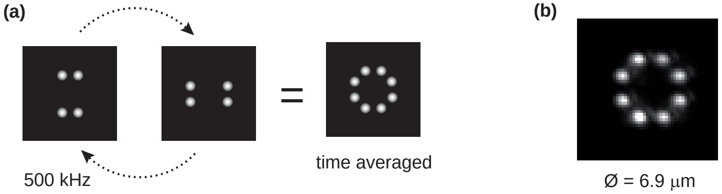

Fig. 5.4: (a) Simulation data illustrating the generation of a time-averaged ring lattice: two 2x2 rectangular square lattices - arranged perpendicular to each other around a common symmetry axis - are alternately projected onto the atoms. The switching frequency between the two configurations is 500 kHz, well above the trapping frequency of each individual lattice site. (b) Real data image showing the light intensity distribution of the resulting 8-site ring lattice with a diameter of $6.9\,\mu$m.

5.3 Atoms in micro-potentials

5.3.1 Loading the micro-traps

The micro-trap patterns are filled from the reservoir of cold atoms captured in the optical dipole trap (FORT) which is used for the transport and the final evaporative cooling in the glass cell. For this, the transport beam and the micro-traps are spatially superimposed as sketched in Fig. 5.1. Fig. 5.5(a) corresponds to the experimental implementation, showing an *in-situ* absorption image of the center part of the atomic sample held in the FORT (black region). On top, a 4x4 lattice is imprinted whose intensity distribution is simultaneously imaged, here appearing as white dots. For the transfer of atoms, we smoothly ramp up the power of the micro-trap potential to its final value (about 100 μW per site) in 200 ms and then switch off the transport trap rapidly.

5.3.2 Single-site resolved imaging

Imaging atoms in the micro-traps is challenging as the individual tightly focussed laser beams spatially overlap at a certain distance along the axial direction, depending on their separation. Moreover, the atoms typically populate energy levels up the edge of the trap right after the transfer. Using resonant absorption imaging along the microscope axis, the individual atomic samples in different trapping potentials therefore appear as a continuous shadow cast on the CCD camera. However, the filling of the micro-traps can be reduced by sending resonant light onto the atoms prior to the imaging. For this purpose, we apply a resonant light pulse of 4 μs at one tenth of the ^{6}Li saturation intensity (2.54 mW/cm^2) onto the sample. This removes the atoms in trap regions of shallow potential depth and only leaves atoms in the tightly confining center. By a second resonant light pulse (24 μs) at twice the saturation intensity, the remaining atoms are then imaged through the microscope setup onto the CCD camera. Fig. 5.5(b) shows the *in-situ* absorption image of the remaining atoms trapped in a 4x4 two-dimensional square lattice. Here, the site separation amounts to 2.5 μm, which is easily resolved by the imaging setup.

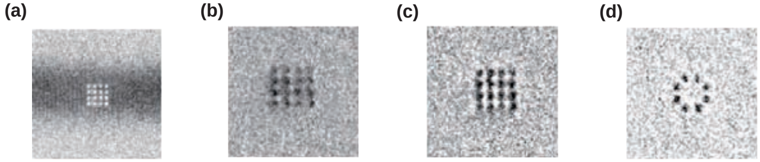

Fig. 5.5: (a) 4x4-site 2D optical lattice superimposed to a fermionic atom cloud trapped in the transport dipole trap. For this image, the bandpass filter for 671 nm in front of the CCD camera was removed, allowing to image both the trapped atom cloud with resonant absorption imaging at 671 nm and the focal light intensity distribution of the 4x4 lattice at 767 nm. (b) Resonant absorption image of atoms trapped in the lattice structure after a preparatory resonant light pulse was applied which removed atoms in the shallow trapping regions. (c) Off-resonant imaging of the same system, red-detuned by $\sim 10\Gamma$ with respect to the upper hyperfine ground state of ^{6}Li (illumination time: 12 μs). The lattice spacing in (b) and (c) is 2.5 μm. (d) Equivalent red-detuned imaging of atoms trapped in the 8-site ring lattice pattern (diameter 6.9 μm) given in Fig. 5.4. All images are divided by a reference image taken without atoms being present.

Alternatively, due to the high optical density the atoms can also be imaged with off-resonant laser light, which only reveals the atoms captured in the center of each micro-trap. For this, we red-detune the imaging light driving the $|2S_{1/2}\rangle$ to $|2P_{3/2}\rangle$ transition by about 10Γ with respect to the second lowest hyperfine sub-state of ^{6}Li. Here, $\Gamma = 5.9\,\mathrm{MHz}$ is the natural line width of the $D2$ transition of ^{6}Li. The resulting off-resonant dispersive image can be seen in Fig. 5.5(c), where the atoms in the different trap centers of the 4x4 lattice appear as well separated dark spots. In this case, a preparatory resonant light pulse in advance is not required. We applied the same off-resonant imaging technique to atoms trapped in the 8-site ring lattice structure of Fig. 5.5(b) (see Fig. 5.5(d)).

The number of trapped atoms can be estimated in a time of flight (TOF) measurement: Having released the trapped sample from the confining optical potential, we image the expanding cloud after a certain TOF by means of resonant absorption imaging through the microscope. From a fit to the detected density profile we determine the total atom number. For the given situation in Fig. 5.5(c), the fit gives an upper limit of 300 atoms per lattice site.

5.3.3 Lifetime in micro-traps

We also determined the lifetime of the trapped sample in a separate experiment, measuring the remaining atom number for different hold times in the trap. The corresponding data are shown in Fig. 5.6. For the static potential (see Fig. 5.6(a)), we observe a two-stage loss process of the trapped atoms. In an initial fast decay on a short timescale ($\sim$100 ms), the atom number is approximately reduced by a factor of

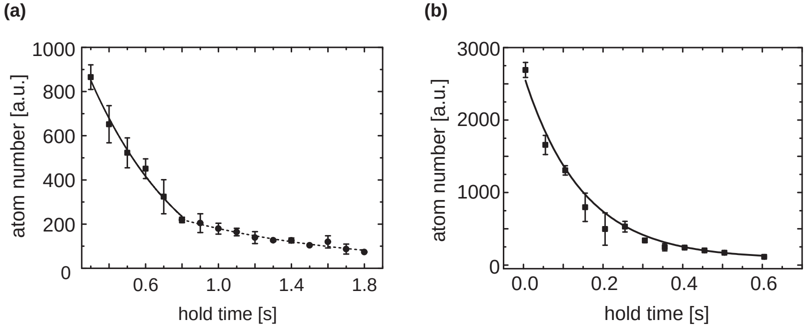

Fig. 5.6: Lifetime measurement of a weakly interacting Fermi gas trapped in different micro-trap configurations. (a) shows the measured particle decay from the static 4x4 square lattice system of Fig. 5.5(b). The solid and dashed curves are first order exponential fits for the first 800 ms and the subsequent hold time, respectively. (b) Corresponding particle decay for the time-averaged ring lattice configuration of Fig. 5.5(d). In contrast to (a), we observe a single-stage decay process only, fitted by a first order exponential model (black line).

2. Subsequently, the population decays exponentially on a longer timescale, yielding a lifetime of 800 ms. For the time-averaged ring lattice (see Fig. 5.6(b)), we find shorter lifetimes of about 100 ms.

A recent measurement of inelastic collisions in a two-component Fermi gas prepared in the strongly interacting BEC-BCS crossover [158] showed that two- and three-body collisions give rise to particle losses on a time scale well above one second. Our samples have a comparable density, yet are weakly interacting ($a = -300\,a_0$) and hence the effect of three-body collisions on the observed lifetime is expected to be negligible. In addition, we can exclude light scattering to affect the lifetime of the trapped sample. For the given trap parameters, the photon scattering rate is 0.25 Hz per atom. Most likely, the particle loss is caused by free evaporation from the initially completely filled micro-traps. Moreover, the intensity of the micro-trap was not actively stabilized for the presented measurement, possibly causing spilling of particles from the trap due to fluctuations in the trap depth. The even faster loss rates observed for the ring lattice potential are probably induced by heating of the sample due to the fact that this particular trapping configuration results from a time-averaged projection of two rectangular lattice patterns. Further investigation is needed to fully understand the observed lifetimes.

5.4 Summary

In conclusion, we have presented an experimental setup with two high-resolution microscope objectives that allows us to optically probe and prepare an ultracold Fermi gas on the microscopic length scale of the Fermi wavelength. Employing a 2D acousto-optical deflector, we have demonstrated the site-by-site generation of a finite two-dimensional square lattice and a 8-site ring lattice configuration. Moreover, we have shown the capability to load small numbers of atoms into these optical micro-potentials and to detect them with single-site resolution.

An immediate, although non-trivial extension of this work would be the measurement of the temperature in the micro-traps. Currently, the measured particle numbers and the known trap geometry should lead to a Fermi temperature close to the trap depth which gives us confidence in the assumption that the trapped sample might be quantum degenerate.

The expected substantial tunneling amplitudes for ^{6}Li atoms in combination with the possibility to tune the inter-particle interactions via Feshbach resonances promises a possible realization of Hubbard-model like physics beyond the standard optical lattice approach with interfering laser beams. While the site-by-site creation of lattice sites has the advantage of the intrinsic absence of additional external confinement, it also offers the ability to generate lattice systems of low symmetry or systems with inherent defects. In addition, our setup holds the potential for single-site addressability allowing the individual manipulation of atoms in different trap spots [36, 150, 159, 160].

6 Local observation of antibunching

The Pauli exclusion principle states one of the most fundamental principles in physics, ubiquitous in any Fermi system. In the research field of ultracold atoms, several outstanding experiments have provided evidence for effects of Pauli suppression in Fermi gases: indirect manifestations of the Pauli principle have been observed by the suppression of elastic atomic collisions [161], clock shifts in radio frequency spectroscopy [162], and in the spatially modified extension of a degenerate Fermi gas affected by Pauli pressure [39]. Moreover, measurements of two-particle anticorrelations in Hanbury Brown-Twiss experiments with superfluid ^{3}He [96] and ultracold fermions in optical lattice [20] revealed fermionic antibunching in an interferometric way. However, a direct manifestation of antibunching in real space has not yet been demonstrated.

In this chapter, we report on the direct visualization of the Pauli exclusion principle in real space via high-resolution *in-situ* measurements of density fluctuations in an ultracold Fermi gas of weakly interacting ^{6}Li atoms. From a number of absorption images recorded under the same experimental conditions, we extract the mean and the variance of the density profile. Our measurements show that the density fluctuations in the center of the trap are suppressed for a quantum degenerate gas as compared to a non-degenerate gas. This manifestation of antibunching is a direct result of the Pauli principle and constitutes a local probe of quantum degeneracy. We analyze our data using the predictions of the fluctuation-dissipation theorem, which relates the density fluctuations of the gas to its isothermal compressibility. Thereby, we demonstrate a new technique for a fluctuation-based temperature measurement [26, 27, 100].

Parts of this chapter are published in [93]: T. Müller, B. Zimmermann, J. Meineke, J.-P. Brantut, T. Esslinger, and H. Moritz, 'Local Observation of Antibunching in a Trapped Fermi Gas', *Phys. Rev. Lett.* **105**, 040401 (2010). This publication [93] and a related work by C. Sanner, et al. at the MIT [163] have been highligthed by a *'Viewpoint'* in the APS journal *Physcis* [164] and by a *'news&views'* article in *Nature Physics* [165].

6.1 Introduction

A finite-size system in thermodynamic equilibrium with its surrounding shows characteristic fluctuations as it has been discussed in chapter 2.4. These fluctuations carry important information about the quantum statistical and thermodynamic properties of the system as a whole. Suppose we have a large-volume ideal gas and probe a small subvolume within it in different temperature regimes. In a classical thermal gas, particles are distinguishable and uncorrelated, and hence the repeated measurement of the particle number contained in the probe volume would yield a Poissonian distribution for the particle fluctuations. However, as soon as quantum mechanics comes into play at low temperatures, particle fluctuations are fundamentally governed by the specific quantum statistics and the many-body state of the constituent particles. Most striking, particles become identical and thus subject to quantum mechanical exchange symmetry. For bosons, positive density correlations build up, until Bose-Einstein condensation occurs. This effect is commonly denoted as bunching and gives rise to enhanced density fluctuations when the particles in the fictitious probe volume above are bosons at sufficient low temperatures. In contrast, fermions obey the Pauli exclusion principle suppressing any process that requires two fermions to occupy the same quantum state. As a consequence, this induces anti-correlation between the particles and leads to the effect known as fermionic antibunching. Thus, fluctuation of particle numbers in an ideal Fermi gas are squeezed below the Poissonian shot noise level.

6.2 Probing density fluctuations in a trapped Fermi gas

Although the effect of the Pauli suppression on density fluctuations seems to obvious by theory, antibunching apparently turns out to be intrinsically difficult to be directly observed in real space. In general, measurements of density fluctuations in a specific probe volume can be performed either on a trapped sample, i.e. *in-situ*, or after free ballistic expansion which maintains the phase space density and thus only leads to a re-scaling of the characteristic fluctuations according to a distinctive scaling transformation. The latter method has been successfully applied in [163] to measure the suppression of density fluctuations in a nearly non-interacting quantum degenerate Fermi gas. However, the time-of-flight expansion of a Fermi gas with notable interparticle interactions is highly non-ballistic, and thus a re-scaling of the measured density fluctuations back to the initial in-trap situation becomes impossible. Hence, free ballistic expansion method is only applicable to a restricted number of systems. In contrast, *in-situ* probing circumvents all these limiting constraints and is thus applicable to a larger variety of physical systems [27]. Yet, *in-situ* probing generally requires high spatial resolution, for which our microscope setup presented in chapter 4 is ideally suited.

6.2.1 Preparation and measurement procedure

We first describe the experimental procedure to prepare the object under investigation, a weakly-interacting Fermi gas of about 6×10^4 ^{6}Li atoms equally populating the two lowest hyperfine sub-states ($|1\rangle = |m_J{=}-1/2, m_I{=}1\rangle$ and $|2\rangle = |m_J{=}-1/2, m_I{=}0\rangle$). Following the method described in chapter 3.7, the atoms are loaded into an optical dipole trap created by a far off-resonant laser with a wavelength of 1064 nm, focused to a $1/e^2$-radius of $(22\pm1)\,\mu$m. The cloud is then optically moved [107] into the octagonal glass cell (see Fig. 6.1). In the glass cell, forced evaporation is performed by reducing the trap power from initially 2 W to 4.7 mW. During evaporation a homogeneous magnetic field of 300 G is applied to set the s-wave scattering length a for inter-state collisions to $-300\,a_0$. The magnetic field is then ramped to 475 G in 150 ms, changing a to $-100\,a_0$, and finally the power of the trapping beam is increased to 10 mW in 100 ms. Alternatively, we prepare the lithium gas at temperatures above quantum degeneracy. For this, we evaporate to 50 mW before re-compressing to 100 mW, followed by a 100 ms period of parametric heating. In both cases, the cloud is allowed to thermalize for 350 ms before an absorption image is taken. Since $|k_\mathrm{F} a| < 10^{-2}$ with k_F the Fermi wave vector, the gas is weakly

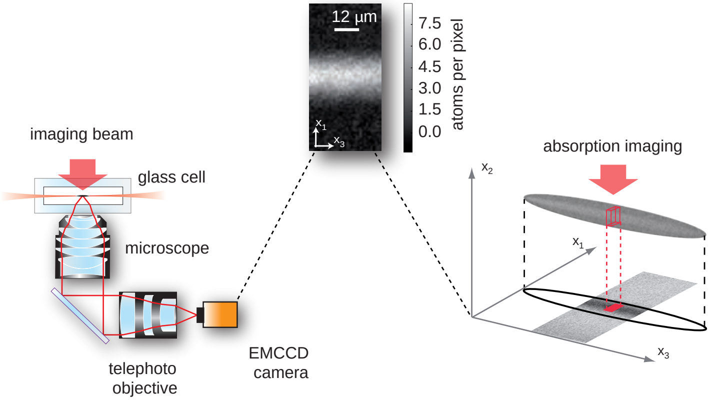

Fig. 6.1: Left: Setup for high-resolution imaging of the trapped ^{6}Li gas. The shadow cast by the atoms held in the dipole trap is imaged through the microscope objective and a telephoto objective onto an EMCCD chip. The resolution ($1/e^2$-radius) is 1.8 μm at a wavelength of 671 nm and the magnification is 54. The resolution of the microscope objective has been artificially reduced with a diaphragm in order to increase the depth of field to the order of the cloud size. Center: Density distribution (atoms per pixel) of the trapped atoms obtained by averaging over 20 realizations. The effective pixel size measures 1.2 μm, the maximum optical density is ~ 2. The images which we evaluate are $\sim 40\,\mu$m wide showing the center of the cloud, which has a total length of 500 μm. Right: Construction of the observation volume: A 4×4 pixel area defines the probe volume along the line of sight of the absorption imaging.

interacting and thus almost ideal.

Our imaging setup is sketched in Fig. 6.1. The probe light, resonant with the lowest hyperfine state of the $|2S_{1/2}\rangle$ to $|2P_{3/2}\rangle$ transition, is collected by the high-resolution microscope objective and imaged on the electron-multiplying CCD (EMCCD) chip. The atoms are illuminated for $8\,\mu$s. Thereby, each atom scatters about 20 photons on average. Typical data are presented in the upper part of Fig. 6.1. There, we show the average density distribution obtained from absorption images of 20 experiments. Since our imaging setup only offers a limited field of view of $100\,\mu\text{m} \times 100\,\mu\text{m}$, while the cloud measures $\sim 500\,\mu$m in axial direction, we only probe the center part of the cigar-shaped cloud. However, our detection method stands out to be local as will be demonstrated in the next paragraph, and therefore, the restricted detection area does not limit the measurement at all.

6.2.2 Data processing

The basic idea of our experiment rests upon the repeated production of a cold Fermi gas and the determination of the number of atoms contained in a small subvolume of the full cloud. Evaluating the statistics over the different experimental realization, we extract the mean and variance of the atomic density within the probe volume. In the following paragraphs, we provide a detailed discussion of the data processing which had to be carried out with reasonable care since also other noise sources than the atomic noise contribute to the raw data, and for which appropriate corrections must be done. As we will see, the main contribution stems from photon shot noise owing to the fact that even the same number of atoms does not always scatter the same number of photons when doing repeated measurements.

Our probe volume is specified as depicted in Fig. 6.1(right). The position of each pixel in the imaging plane of the camera defines a line of sight intersecting with the atomic cloud. Correspondingly, each pixel [1], having an effective area A, determines our observation volume in the atomic cloud along its line of sight. On the one hand, this volume is sufficiently small to be considered as a subsystem in thermal equilibrium with the remaining part of the cloud in terms of the grand canonical ensemble. On the other hand, it is also sufficiently large to cover the exchange hole in the fermionic pair correlation $g^{(2)}(\boldsymbol{r}-\boldsymbol{r}')$ (see Fig. 2.7). If the observation volume was to small, i.e. smaller than the distinctive correlation length of the nearly ideal Fermi gas given by k_F^{-1}, the measured fluctuations in the probe volume would be lower than expected from thermodynamics. Thus, we have also adapted the spatial resolution of the microscope to the size of the effective area A. For the measurements throughout this chapter, the resolution has been artificially reduced to $1.8\,\mu$m, which in turn helps to increase the depth of field to the order of the cloud size.

In general, the number of atoms in the probe volume is related to the amount of light which passes through the cloud and is finally detected on the camera. This relation is parameterized by the transmission coefficient t. At low saturation, the transmission t of the probe light through an observation volume containing N atoms reads [108]

---

[1] For the present measurement we apply a 4×4 software binning of the camera pixels. One camera pixels has a physical size of $16\,\mu\text{m} \times 16\,\mu\text{m}$. Due to the 54-fold magnification of the imaging system, one camera pixel represents an effective area of $300\,\text{nm}\times 300\,\text{nm}$ in the object plane (position of atom cloud). Thus, the binning area $A = 1.2\,\mu\text{m} \times 1.2\,\mu\text{m}$ defines the size of a "pixel" referred to in this chapter.

$$t = e^{-\sigma \cdot N/A}\,, \tag{6.1}$$

where σ is the photon absorption cross section. As a consequence, for small Gaussian fluctuations of the atom number, the *relative* fluctuations of the transmission coefficient are equal to the *absolute* fluctuations of the optical density and are thus directly proportional to the number fluctuations. Standard error propagation yields:

$$\frac{(\Delta t)^2}{\langle t \rangle^2} = \frac{\sigma^2}{A^2}(\Delta N)^2\,. \tag{6.2}$$

Here, $(\Delta t)^2$, $\langle t \rangle$ and $(\Delta N)^2$ are the variance and the mean of the transmission coefficient, and the variance of the atom number, respectively.

During the detection process, incoming photons are registered by the EMCCD chip, converted into photoelectrons and finally displayed as electronic counts. Hence, the repeated measurements of identically prepared clouds provide us with a set of count numbers C for each pixel, i.e. each observation volume. Typically, we register ~ 1300 counts, corresponding to ~ 130 photons at the position of the atoms. For each pixel, we finally compute the variance $(\Delta C)^2$ and mean $\langle C \rangle$ over a set of images taken under the same conditions. The relative noise of the counts and the relative noise of the transmission are related by:

$$\frac{(\Delta C)^2}{\langle C \rangle^2} = \frac{2g}{\langle C \rangle} + \frac{(\Delta t)^2}{\langle t \rangle^2}\,. \tag{6.3}$$

Here, g is the gain of the camera for converting photoelectrons to counts. A derivation of equation (6.3) is given in appendix C. The first term owes to the contribution of photon shot noise while the second term is the contribution of atomic noise. The factor 2 in the photon shot noise term is caused by the electron-multiplying register [166]. We extract the contribution of the atoms to the relative fluctuations of the counts, by subtracting photon shot noise on each pixel according to (6.3). This requires the value of g (typically ~ 15), which we determine from the linear relationship between the variance and the mean of the number of counts in a set of repeated measurements [2]. The atom number fluctuations are subsequently obtained from (6.2). We note, that at this stage no division by a reference image has been performed, avoiding this source of noise.

---

[2] Without applying the 4×4 software binning of the camera pixels, photon shot noise is the dominating contribution to the data while atomic shot noise is nearly undetectable. Thus, the second term in equation (6.3) is negligible under those conditions, and g is given by the linear relationship between the variance and the mean of the number of counts. We use this fact, to determine the value of g. Imaging of the atomic cloud without software binning provides us with different count values C over the pixel array, from nearly zero at the position of the atoms to rather high values from regions without atoms. We then deduce the mean and variance for each pixel over a set of images obtained from repeated measurements. A fit to the slope of the plot "variance versus mean" finally yields the value of g.

To reduce technical noise adding to these fluctuations, we reject images showing the largest deviations of the total atom number or cloud position. For the present data, images deviating more than 1.5 (1.0) standard deviations, corresponding to $0.72\,\mu$m ($5\,\%$) in the mean position (total atom number). In total, this amounts to excluding about 30% of the images. The remaining shot-to-shot fluctuations of the total atom number $(\Delta N_{\mathrm{tot}})^2$ are taken into account by further subtracting the quantity $(\Delta N_{\mathrm{tot}})^2/N_{\mathrm{tot}}^2 \langle N \rangle^2$, which is less than $< 2\%$ of N [26]. Total probe intensity variations from shot to shot are below $0.5\,\%$. Applying this algorithm to each pixel of the images yields the variance of the atom number in different probe volumes and hence a local measurement of the variance of the atom number along the cloud.

The mean atom number per pixel is calculated by dividing the mean transmission profile by the mean of reference images taken without atoms after each shot, thus averaging shot-noise before division. The values for variance and mean, obtained by applying the above procedures, are then averaged along equipotential lines of the trap, mainly along the axial direction. These lines deviate from horizontal lines (x_3-axis) in our images by less than half a pixel ($0.6\,\mu$m), and therefore this averaging process is reasonably justified.

6.3 Manifestation of antibunching in real space

6.3.1 Density fluctuations above and below quantum degeneracy

Fig. 6.2 shows the observed variance of the atom number plotted against the mean atom number detected on a pixel. The different mean values originate from different areas in the cloud with more and less particles. For the presented data, we additionally applied a binning of the mean values in groups of similar average atom numbers and according to this averaged over the variance values in the corresponding bins. For comparison, we have studied the density fluctuations of the weakly interacting Fermi gas in two different temperature regimes: one set of data of identically prepared atom clouds has been taken at temperatures above quantum degeneracy (red squares), i. e. for a thermal gas with $T/T_{\mathrm{F}} > 1$, the other set of data pertains to a quantum degenerate gas (blue circles).

Density fluctuations in a thermal Fermi gas

Above quantum degeneracy, the observed variance is found to be proportional to the mean number of atoms as it is expected for a subvolume of an ideal thermal gas in thermal equilibrium with its surrounding (see chapter 2.4.1). Moreover, the linear behavior confirms that the fluctuations originate from atomic shot noise only and the data processing removes reliably the dominating contribution of the photon shot noise.

However, the slope of this linear relation between the observed variance and mean values of the atom number is not equal to one as expected for a Poissonian distribution. To quantitatively understand the slope of the noise curve, which is fitted to be

0.20 ± 0.02, two main effects have to be considered which may reduce the observed variance and explain the deviation from a slope of one. First, the effective size of the pixel ($1.2\,\mu$m) is of the order of the resolution of the imaging system ($1.8\,\mu$m). As a consequence, the observed noise is the result of a blurring of the signal over the neighboring pixels. This effect has also been observed in similar experiments addressing density fluctuations in bosonic systems [26, 27]. We performed a simulation accounting for the effect of finite spatial optical resolution and verified the reliability of this simulation by a variation of the data processing. In general, a larger pixel size is supposed to increase the slope, because then the spatial volume for the atom counting is larger than the resolution area and blurring over neighboring pixels becomes suppressed. According to this, we applied a 16×16 (instead of 4×4) software binning of the camera pixel which results in an increase of the slope to 0.8 agreeing with the predictions of our simulation. With respect to the present data, the simulation is able to explain a reduction factor of 0.22. A larger pixel size, however, implies a worse signal-to-noise ratio. We therefore proceed with a binning size of $1.2\,\mu$m. The second effect causing a decrease of the slope is related to the intensity of the probe light. The light intensity used for the detection is $(15 \pm 1)\%$ of the saturation intensity. This leads to a reduction of the photon absorption cross section due to saturation by a factor of 0.95 and due to the Doppler-shift by a factor of about 0.9. In combination, both effects lead us to expect a slope of about 0.19, in good agreement with the observed slope of 0.20 ± 0.02.

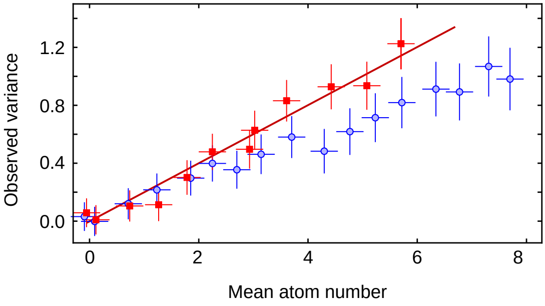

Fig. 6.2: Observed variance versus mean of the atom number detected on a pixel. Red squares show the data for a non-degenerate and blue circles for a quantum degenerate gas. The solid red line is a linear fit to the non-degenerate gas, yielding a slope of 0.20 ± 0.02. For the data shown, 80 experiments were performed, 60 for the degenerate case and 20 for the non-degenerate case. About 30% of the experiments were excluded. The error bars shown are estimated from the subtraction of photon shot noise which is the dominant contribution.

Density fluctuations in a quantum degenerate Fermi gas

We now turn to the data taken for the quantum degenerate gas (blue circles in Fig. 6.2). At low densities, the variance is again found to be proportional to the mean density. For increasingly higher densities, we observe a departure from the linear behavior and the density fluctuations are well reduced compared to the shot noise limit seen for the non-degenerate gas. This signature of suppressed density fluctuations is a clear manifestation of antibunching in our system, appearing as a direct consequence of the Pauli principle. In a certain way, one can think of the Pauli principle as giving rise to an interatomic "repulsion", which increases the energy cost for large density fluctuations. This situation is similar to the case of bosonic systems with strong interparticle interactions, where observations have shown a reduction of density fluctuations [26] and squeezing of the fluctuations below the shot noise limit [27, 167].

6.3.2 Density fluctuation profiles

In contrast to previous measurements on antibunching [20, 96] in atomic Fermi systems, we have measured density fluctuations in a spatially resolved way. Fig. 6.3 shows the same data for the variance (points/squares) and the mean (solid lines) of the atom number as Fig. 6.2, however here as a function of the radial position in the trap. Fig. 6.3(a) and (b) present the data for the thermal gas and the quantum degenerate Fermi gas, respectively. In both cases, the variance has been re-scaled according to the slope fitted in Fig. 6.2. In contrast to Fig. 6.2, the observed variances along the profile have not been averaged over regions with equal mean density.

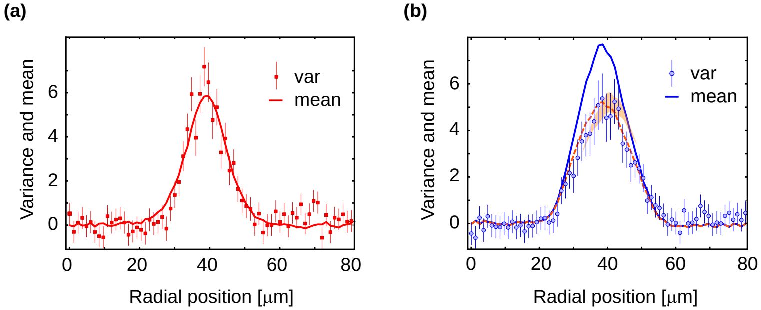

Fig. 6.3: (a)/(b): Spatially resolved measurement of antibunching. The red (blue) line shows the mean atom number and the red squares (blue circles) the corresponding variance along the x_1-axis for a thermal gas (a9, respectively for a degenerate gas (b). The variances are re-scaled using the slope fitted in Fig. 6.2. Error bars are estimated from the subtraction of photon shot noise, which is the dominant contribution. The dashed line shows the variance derived from theory. The shaded region in (b) indicates the uncertainty originating from uncertainties in the trap parameters.

In the thermal gas, the re-scaled variance profile (red squares) fairly follows the mean density profile (red solid line) due to the Poissonian nature of the shot noise, which predicts $(\Delta N)^2 = \langle N \rangle$. In contrast, for the quantum degenerate gas we observe a clear reduction of the variance profile (blue dots) with respect to the mean density profile (blue line). While the variance is proportional to the mean in the wings, at low density, we measure a reduction of the variance by about 2 dB close to the center, at higher density. The reduction of fluctuations can be interpreted as a direct indication of the level of quantum degeneracy of the gas. The larger the average occupation of a single quantum state, the more the effect of the Pauli principle becomes evident and fluctuations are consequently suppressed. Fig. 6.3(b), which corresponds to the column integrated analogue of Fig. 2.6, represents thus a direct measurement of the local quantum degeneracy, which is larger in the center of the cloud than in the wings.

To understand this quantitatively, we describe the atoms contained in an observation volume in terms of the grand canonical ensemble. In addition, we apply the local density approximation which gives rise to a local chemical potential as we have discussed in detail in the course of chapter 2.4.3. For a non-interacting gas, the ratio of the mean atom number and its variance is determined by the fugacity z of the system and directly results from the ratio of equations (2.38) and (2.37) given in chapter 2.4.2. We find the following equation

$$\frac{(\Delta N)^2}{\langle N \rangle} = \frac{\int \mathrm{Li}_{1/2}(-z(x_1, x_2))dx_2}{\int \mathrm{Li}_{3/2}(-z(x_1, x_2))dx_2}\,, \tag{6.4}$$

where Li_i is the i-th polylogarithm function, x_1 and x_2 are radial coordinates of the cloud. Since the imaging process yields the column density due to projection onto the CCD camera, the two integrals account for the corresponding line-of-sight integration, in the present case along the x_2-axis. The red dashed line in Fig. 6.3(b) describes the variance profile in terms of the grand canonical ensemble and has been computed using (6.4). For this, we assign the experimentally observed mean profile to the denominator of the left hand side. Moreover, we need to determine the chemical potential $\mu(\boldsymbol{r}) = \mu_0 - V(\boldsymbol{r})$ in the local density approximation (see 2.4.3), which depends on the spatial shape of the trapping potential. In contrast to common habit, we do not approximate the trap by an harmonic potential, but consider the correct Gaussian shape of the trap. Additionally, we determine the central fugacity $z_0 = 13^{+18}_{-4}$ in an independent time-of-flight experiment (see below). In conclusion, the dashed line shows that our description in terms of the grand canonical potential assuming an ideal gas reproduces the experimental data within the error bars. Note that, even though adjacent pixels in one image might still be correlated, we do not run into problems with the grand canonical interpretation, since we first calculate the variance for each pixel in depth, i.e. over many realizations. By this, the variances get uncorrelated and averaging is unproblematic.

6.4 Fluctuation-based thermometry

We now focus on the interpretation of our results in terms of the fluctuation-dissipation theorem, resuming the discussion of chapter 2.5. At thermal equilibrium, density fluctuations are universally linked to the thermodynamic properties of the gas via the fluctuation-dissipation theorem, which reads

$$k_B T \frac{\partial \langle N \rangle}{\partial \mu} = \delta N^2. \tag{6.5}$$

Here, T is the temperature of the gas, μ the chemical potential and k_B the Boltzmann constant. Since the local density approximation allows one to assign a local chemical potential to any position in the trap, it is possible to determine the compressibility $\frac{\partial \langle N \rangle}{\partial \mu}$ directly from the mean density profiles as demonstrated in [27]. Referring to equation (6.5), the ratio of this quantity to the measured variance profile of the cloud provides a universal method for fluctuation-based thermometry[3] as proposed by [100]. We apply this procedure to our data by computing the compressibility,

$$\frac{\partial \langle N \rangle}{\partial \mu} = \frac{\partial \langle N \rangle}{\partial x} \left(\frac{\partial \mu}{\partial x} \right)^{-1}, \tag{6.6}$$

where we again take the Gaussian shape of the optical dipole trap into account. To avoid the problems of numerically differentiating experimental data, we fit the mean density profile with a linear combination of the first six even Hermite functions and use the fitted curve as a measure of the density profile in equation (6.5) [4]. Fig. 6.4 shows the variance of the atom number plotted against the dimensionless compressibility $U_0 \frac{\partial \langle N \rangle}{\partial \mu}$, where U_0 is the trap depth. We observe the linear relation described by equation (6.5) with a slope of $\frac{k_B T}{U_0} = 0.27 \pm 0.04$ for both data sets, the degenerate and the non-degenerate. From the physics of evaporative cooling it is expected that both slopes are the same [170], yielding the temperatures in units of the trap depth. Using the trap depths experimentally derived from the measured laser powers of the dipole trap, we obtain temperatures of $(145 \pm 31)\,\mathrm{nK}$ for the quantum degenerate gas and $(1.10 \pm 0.06)\,\mu\mathrm{K}$ non-degenerate gas, respectively.

In order to estimate the accuracy of these values and the quality of this new thermometry method, we have also performed time-of-flight measurements with clouds prepared under the same conditions. In this method, we determine the temperatures by fitting the measured density profiles after free expansion of 1.5 ms (1 ms for the non-degenerate gas) to the calculated shape of a non-interacting gas released from a Gaussian trap. This procedure gives us slightly higher temperatures for the degenerate and the non-degenerate clouds, which are $(205 \pm 30)\,\mathrm{nK}$ $(T/T_F = 0.34 \pm 0.1)$ and $(1.6 \pm 0.2)\,\mu\mathrm{K}$ $(T/T_F = 1.9 \pm 0.1)$, respectively. We attribute the discrepancy between both temperature measurements mainly to two effects. One effect is due to the uncertainty in the exact knowledge of the trapping potential, which both methods are quite sensitive to. A deviation of the measured waist of only 5% to 10% already causes a doubling of the temperature resulting from the fluctuation-based thermometry. In contrast, the density profile of a degenerate Fermi gas in the time-of flight method becomes nearly independent of the temperature, when the gas is highly degenerate, whereas fluctuations decrease linearly with lower temperatures. Hence, the fitting-method is for sure less reliable at very low temperatures. The second effect leading to the observed discrepancy owes to residual experimental fluctuations from shot to shot which still affect the data even after processing and post-selection.

---

[3] For other fluctuation-based temperature measurements we refer to [168] and [169]

[4] The difference of this method with the direct numerical differentiation of data (where possible) is within the error bars.

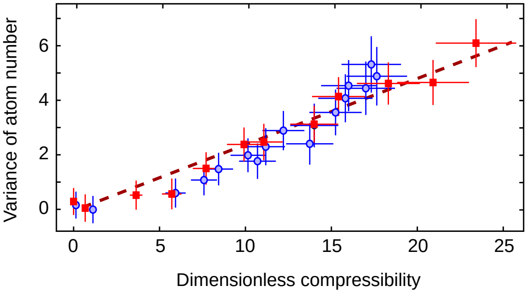

Fig. 6.4: Fluctuation-based temperature measurement. Variance of the atom number detected on an effective pixel versus the dimensionless compressibility. The blue circles and red squares show the data for the quantum degenerate and the non-degenerate case, respectively. The dashed red line is fitted to the red squares, giving the temperature according to equation (6.5).

6.5 Summary

In summary, we have measured *in-situ* density fluctuations in a trapped Fermi gas at two different temperatures. At high temperature above quantum degeneracy, we observe the expected atomic shot noise. Below quantum degeneracy at lower temperatures, density fluctuations are suppressed due to the Pauli principle which manifests a direct signature of antibunching in real space. We note that the suppression effect is more pronounced at the center of the cloud where the density is higher. This feature can be interpreted as a local indicator for the level of quantum degeneracy in the gas. Since our measurements are performed at thermal equilibrium, the variance of the atom number is related to thermodynamic quantities via the fluctuation-dissipation theorem. Within the local density approximation, we use the fluctuation-dissipation theorem to demonstrate a model independent thermometry for cold fermions.

While in the present situation with weak interactions this thermometry is comparable to the usual time-of-flight method, we expect it to be of particular interest in strongly interacting clouds where time-of-flight is not tractable. Moreover, fermions unlike bosons cannot exhibit first-order long range coherence due to the Pauli principle. In contrast, when a Fermi system enters a quantum correlated phase, for example a superfluid phase, long range even order correlations build-up [171]. Here, density fluctuations, probing second-order correlations, thus seem to be a natural tool for studying strongly correlated Fermi gases.

7 A local interferometer probing spin fluctuations in a quantum gas

Currently, the research with quantum degenerate Fermi gases is exploring a great variety of strongly correlated many-body regimes such as the pseudo-gap physics [67], spin-ordering [172], or the Fulde-Ferrell-Larkin-Ovchinnikov phase [88]. These phenomena are driven by pair formation and are characterized by distinctive spin correlations, which may vary in space. Conversely, theoretical and experimental efforts are directed towards the measurement of spin correlations in Fermi gases, using for example linear response [22, 23, 70], or directly through noise measurements [99, 173, 174]. Yet, the quantitative measurement of spin correlations in a trapped gas poses severe experimental challenges. In order to characterize strong correlations in the ground-state of interacting many-body systems, it has been recently proposed [30] to use interferometric methods that have proven successful in quantum optics and allow the full characterization of a light field that carries information about the systems under consideration.

In this chapter[1] we present the *in-situ* measurement of the spin fluctuations in weakly and strongly interacting two-component Fermi gases using a shot-noise limited interferometric technique with a spatial resolution of $1.2\,\mu$m. We are thus able to directly probe the correlations present in the many-body state of the system in a spatially resolved way. The spin fluctuations are directly related to the magnetic susceptibility of the system via the fluctuation-dissipation theorem as expressed by equation (2.48) in chapter 2.5 in the theory part of this thesis. We use this relation to deduce the magnetic susceptibility for both the weakly and the strongly interacting gas.

7.1 Local interferometry

In a two-component Fermi gas consisting of an incoherent mixture of atoms in two different hyperfine sub-states, the spin polarization in a given volume is defined by the difference of the atom number in the two states $M = N_1 - N_2$. Due to the hyperfine splitting, the frequency of a light beam that passes through the atoms can be chosen such that the spin polarization is mapped to the phase shift of the beam. In particular, the use of a tightly focussed probe beam leads to a stronger coupling to individual atoms, which enhances the phase shift caused by a single atom [175] and makes it possible to detect spin fluctuations due to a few atoms only. Most important, a small probe makes it possible to address specific parts of the gas and thus to measure the spin polarization locally. To create such a tightly focussed probe beam, with a waist on the micrometer scale and hence of the order of the Fermi wavelength, our microscope setup is ideally suited.

---

[1] Parts of this chapter and appendix D are adopted from a manuscript in preparation for publication by J. Meineke, J.-P. Brantut, D. Stadler, T. Müller, H. Moritz, and T. Esslinger (2011).

7.1.1 Concept of the local interferometer

In order to accurately retrieve the phase-imprinted spin polarization, we place the quantum gas in one of the arms of an interferometer which allows to determine the phase shift with shot-noise limited accuracy. The essential idea of our measurements is best explained by noting the analogy to Young's double slit experiment. Two tightly focussed beams of the same frequency, denoted as probe and the local oscillator, are focussed by our microscope setup to two separate points as shown in Fig. 7.1(a). In the focal plane, both beams have a Gaussian waist of 1.2 μm, defining the dimension of the local probing region. Outside the focal plane, both beams overlap which gives rise to an interference pattern that is finally imaged onto a CCD camera. The

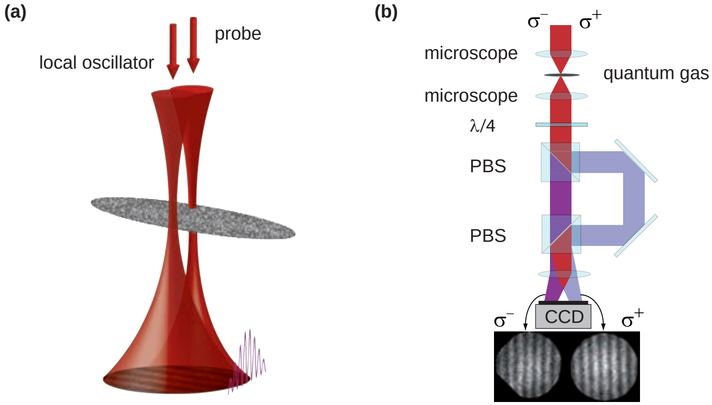

Fig. 7.1: (a) Interferometer beams in the vicinity of the atomic cloud: While the probe passes through the cloud shown in grey, the local oscillator passes by the side of it. The beams overlap to give an interference pattern as shown, which is averaged parallel to the fringes for processing. (b) Optical path used to separate the two polarizations: Using a quarter-wave retardation plate ($\lambda/4$) and two polarizing beam splitters (PBS), we separate the σ^-- and σ^+-polarized light to obtain two interference patterns on one image. The shown interference pattern for the σ^- component is truncated by the edges of the CCD chip for technical reasons. This does not influence the precision of the measurement.

position and visibility of the interference pattern is determined by changes in phase and amplitude of the probe beam, which passes through the trapped cloud of ^{6}Li atoms, while the local oscillator does not. The analysis of the interference pattern thus allows to reconstruct both quadratures, phase and amplitude, of the probe beam, and to extract information about the local properties of the atomic cloud. The interferometer beams are created in an inherently phase-stable way, so that both beams pass through exactly the same optical elements, by using the two-axis acousto-optical deflector (AOD) described in chapter 5.1. We apply two radio frequencies differing by 20 MHz along each axis of the AOD. This results in four beams in the (-1$^{\text{st}}$/-1$^{\text{st}}$)-order diffraction order, arranged in square. Two of these beams have the same frequency, corresponding to the probe beam and the local oscillator, and thus form the interference pattern on the camera (see Fig. 7.1(a)). This avoids the need for active stabilization of the interferometer. The other two beams are detuned by ±20 MHz and their interference patterns average out over the duration of the probe pulses. The intensities of the beams can be controlled via the power in the individual radio frequencies. Phase stability is ensured by deriving each radio frequency from the same source for both axes [140].

A second interference pattern, not affected by the atoms but recorded on the same image, is used to track residual long-term drifts. For this we make use of the birefringence of the atomic cloud due to the fact that only σ^--polarized light interacts with the atoms in a magnetic field [131]. As depicted in Fig. 7.1(b), elliptically polarized light is sent onto the atoms. While only the σ^--polarized component interacts with the atoms driving the $|2S_{1/2}\rangle$ to $|2P_{3/2}\rangle$ transition, the σ^+ component passes undisturbed. After the atoms, both components are split in two different paths using a quarter-wave retardation plate and polarizing beam splitters. This leads to two separate interference patterns on the camera, which are denoted as σ^-- and σ^+-pattern for further reference. An example of the recorded interference patterns is shown in the lower part of Fig. 7.1(b). Together with a reference image taken without atoms, this allows us to accurately extract the phase-shift due to the atoms (see appendix D).

7.1.2 Imprinting atomic spin onto light phase

In order to demonstrate how the presence of an atomic cloud affects the light field, we experimentally determine the phase shift and the optical density as a function of the light detuning for a thermal Fermi gas containing only the second lowest hyperfine sub-state $|2\rangle$ of ^{6}Li. For the preparation, we proceed as shown in the previous chapter and additionally use a so-called p-wave Feshbach resonance at 159 G [48] to remove the second spin component $|1\rangle$ during the final evaporative cooling. We determine the phase shift applying a simultaneous sinusoidal fit to the σ^--patterns in the images with and without atoms. The optical density is determined from the same data by analyzing the visibility of the interference pattern and thus the amount of absorbed light (see equation (3.13)). Fig. 7.2 displays the results of this measurement showing the characteristic asymmetric dispersion curve for the phase shift and the Lorentzian curve for the optical density, slightly broadened due to the finite linewidth of the laser and saturation. To fit the data for the phase shift, we use the model $\phi =$

$-\frac{n_{\text{col}}\sigma_0}{2}\frac{2\delta}{1+s+4\delta^2}$, where $n_{\text{col}}\sigma_0$, s and δ are the on-resonance optical density, the saturation parameter and the detuning from the atomic resonance in units of the linewidth, respectively. The optical density is then given by $d = \frac{n_{\text{col}}\sigma_0}{2}\frac{1}{1+s+4\delta^2}$. Fig. 7.2 shows the results of the fit, where the optical density is calculated using the results of the fit to the phase with no further adjustable parameters. The measured data and theory are in agreement, provided the probe duration is $\sim 1\,\mu$s and the intensity limited to less than $\sim 10\,I_{\text{Sat}}$. The use of stronger (longer) pulses leads to a systematic shift of the measured phases to larger values. Most important, the measurement proves that the signal detected by the interferometer is directly and unambiguously relatable to an atomic property, i.e. the spin population, as opposed to [99]. We also emphasize, that our method to determine the phase shift is by design insensitive to intensity noise in the probe beam, because the phase shift is encoded in space. This is in contrast to the case of Mach-Zehnder interferometers or phase contrast imaging, where the phase is determined from changes in the light intensity.

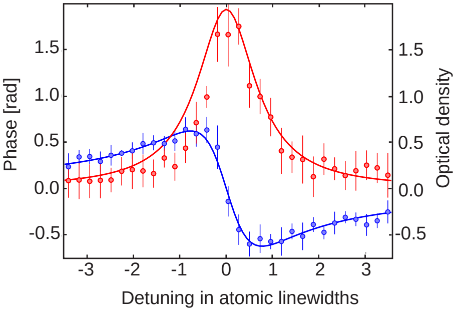

Fig. 7.2: Measured phase (blue circles) and optical density (red circles) as a function of the probe light detuning. The maximum intensity of the probe beam was $I = 1.2 \times I_{\text{Sat}}$, with I_{Sat} the saturation intensity. The duration of the probe pulses was $1.2\,\mu$s. The lines are calculated using the model described in the text by fitting to the phase data giving $n_{\text{col}}\sigma_0 = 3.2$ and $s = 0.6$. The fitted linewidth is 20% broader than the natural linewidth due to the finite linewidth of the probe laser.

7.1.3 High-precession at the shot noise limit

Our measurement of the probability distribution of the spin polarization relies on the faithful mapping of the spin polarization to the phase shift of the probe beam. We therefore show that photon shot noise limits the precision with which we can measure the phase of the light field when no atoms are present in the interferometer. For the determination of the phase fluctuations around a given mean phase, we find that it is more precise to analyze the change of the correlations between the σ^-- and the σ^+-pattern in consecutive images. The phase shift is encoded in the displacement of the zero-crossings of the correlations. This analysis method is also applied in the spin fluctuation measurements below and described in detail in appendix D.

Fig. 7.3 shows the phase variance as a function of the photon number and features the expected power law behavior of the phase fluctuations as a function of the photon number in the probe beam. Indeed, the measured phase variance is expected to be $\delta\phi^2 = \frac{1}{\eta N}$ [176], where η is the quantum efficiency for the photon detection and N is the number of photons in the probe beam. Consequently, using this novel interferometric technique, the phase shift measured in a single experiment reveals the spin imbalance (see next section) for a specific realization of a two-component Fermi gas with the maximum achievable precision, i.e. at the quantum limit.

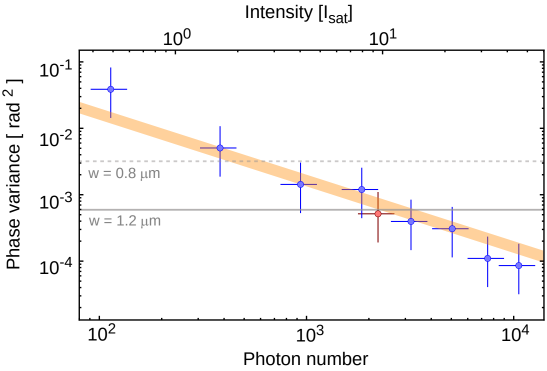

Fig. 7.3: Measured phase variance $\delta\phi^2$ (blue circles) as a function of the photon number in the probe beam determined from 100 measurements for each point. The red point indicates the phase variance for the intensity at which the spin polarization measurements were made. Error bars are an uncorrelated sum of statistical and systematic uncertainties. The orange line shows the expected phase noise for a quantum efficiency $\eta = 0.6$, determined in an independent measurement. The width of the line corresponds to 20% errors estimated from the uncertainty of our determination of η. The gray lines indicate the square of the phase shift expected for a single atom fixed in space at a detuning of half the atomic linewidth for the indicated $1/e^2$-waists of the probe beam [175].

7.2 Probing spin fluctuations in a two-component Fermi gas

We use the interferometer to locally probe the spin fluctuations of different quantum phases in the central region of a balanced two-component Fermi gas, consisting of a mixture of ^{6}Li in the lowest two hyperfine states, denoted by $|1\rangle$ and $|2\rangle$. This directly probes the correlations of the many-body state of the system [30]. By choosing a frequency for the probe light, that is exactly in between the resonances for the states $|1\rangle$ and $|2\rangle$ (see Fig. 7.4 (b)), the phase shift ϕ measured in a single experiment is proportional to the local spin polarization m, expressed by $\phi = m\frac{\delta}{1+s+4\delta^2}$. Here, δ is the detuning from resonance for both state $|1\rangle$ and $|2\rangle$. Repeating this measurement allows us to reconstruct the full distribution of the spin polarization.

7.2.1 Spin fluctuations in a weakly interacting Fermi gas

We first measure the distribution of the spin polarization for weakly interacting Fermi gases at different temperatures. As in the previous chapter, we load a balanced mixture of ^{6}Li in the states $|1\rangle$ and $|2\rangle$ in a single-beam optical dipole trap with a

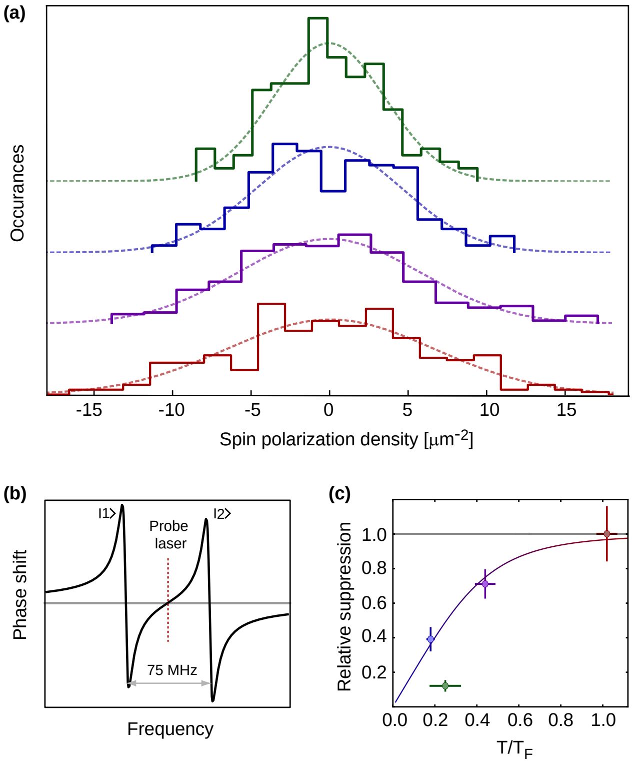

Fig. 7.4: (a) Normalized histograms for the measured phases for weakly interacting gases $T_{\text{thermal}} = 1.02(2)\,T_F$ (red), $T_{\text{hot}} = 0.44(5)\,T_F$ (violet) and $T_{\text{cold}} = 0.18(2)\,T_F$ (blue) as well as a strongly interacting gas of molecules at T=300 nK (green). For the histograms, the respective measurements were repeated 400 times with a probe duration of 1.2 μs and a maximum probe light intensity of $I = 9\,I_{\text{Sat}}$. Each measurement corresponds to a single realization of a Fermi gas, for which a new sample has to be prepared each time. (b) Phase shift as a function of the detuning for a balanced mixture of ^{6}Li. The dashed line indicates the detuning for the measurement of the spin-polarization. (c) Relative suppression of the spin fluctuations as a function of the reduced temperature. Data points are colored identical to (a). The solid line shows the calculated relative suppression of the spin-polarization, accounting for the line-of-sight integration and the geometry of the combined trap.

$1/e^2$-radius of $22 \pm 1\,\mu$m. In addition, a second dipole trap, which runs parallel to the probe beam and perpendicular to the first dipole trap, is focussed to a $1/e^2$-radius of $9\,\mu$m and allows us to prepare the gases at different temperatures but with the same column density in the probe region. In this combined trap, we prepare weakly interacting Fermi gases at a scattering length of $a = -100a_0$ and with different temperatures of $T_{\mathrm{thermal}} = 1.02(2)\,T_F$, $T_{\mathrm{hot}} = 0.44(5)\,T_F$ and $T_{\mathrm{cold}} = 0.18(2)\,T_F$, where T_F is the Fermi temperature in the probe region. The column density for the gas at $T_{\mathrm{thermal}} = 1.02(2)\,T_F$ is 20% lower than for the other two gases.

Fig. 7.4(a) shows the normalized histograms, corresponding to the probability distribution of the spin polarization. Comparing the widths of the distributions for the weakly interacting gases, we find that the distributions are narrower the lower the temperature of the gas. The distributions show no significant asymmetry and are well described by a Gaussian function as expected from the large number of atoms in the probe beam (about 250 in each state). For weakly interacting Fermi gases, number fluctuations in each hyperfine state are independent, so that fluctuations of the spin polarization are given by $\delta m^2 = \delta n_1^2 + \delta n_2^2$. As a consequence, when the temperature is lowered and the gas becomes quantum degenerate, the fluctuations in each state are reduced because only atoms close to the Fermi energy contribute, due to the Pauli principle [93]. The measured variances of the spin polarization, in order of decreasing temperature, are $\delta m^2_{\mathrm{thermal}} = 35(6)\,\mu\mathrm{m}^{-4}$, $\delta m^2_{\mathrm{hot}} = 27(3)\,\mu\mathrm{m}^{-4}$ and $\delta m^2_{\mathrm{cold}} = 15(3)\,\mu\mathrm{m}^{-4}$, where the contribution to the variance originating from photon shot noise $\delta m^2_{\mathrm{bgr}} = 6.5\,\mu\mathrm{m}^{-4}$ has been subtracted. This corresponds to a suppression of the spin fluctuations as compared to a thermal gas having same the column density by 1.9(2) dB for the hot gas, and 4.5(3) dB for the cold gas. As shown in Fig 7.4 (c), this is in agreement with the expected values taking into account line-of-sight integration and the geometry of our combined trap. The agreement between theory and experiment in Fig. 7.4 (c) can thus also be interpreted as evidence for the full thermalization of the gas in the dimple trap with the surrounding bath.

7.2.2 Spin fluctuations in a strongly interacting Fermi gas

We now turn to the study of a gas with strong repulsive interactions, prepared close to the Feshbach resonance with a scattering length of $a \sim 7000a_0$ and a temperature of 300 nK (preparation, see chapter 3.7.3). The resulting histogram is displayed in Fig. 7.4 (a) and shows a distribution of the spin polarization that is significantly narrower than for the weakly interacting gases. This reflects the fact that for interacting gases correlations are present between the hyperfine states. In particular, for strong repulsive interactions close to a Feshbach resonance, weakly bound molecules form. The measured spin fluctuations in such a gas consisting of pairs are created at the cost of breaking the molecules and are consequently very low. We measure $\delta m^2_{\mathrm{pair}} = 5(2)\,\mu\mathrm{m}^{-4}$, with the background $\delta m^2_{\mathrm{bgr}} = 7.5\,\mu\mathrm{m}^{-4}$ subtracted as before. This corresponds to a reduction by 9.2(8) dB as compared to a non-interacting thermal gas. This is lower than the reduction of 18 dB expected for the given scattering length and the waist of the probe beam in our experiment [30]. A possible explanation are frequency fluctuations of the probe beam. Shot-to-shot frequency fluctuations with a variance of $2\,\mathrm{MHz}^2$ correspond to apparent spin fluctuations of $5\,\mu\mathrm{m}^{-4}$. Other reasons for the measured increased fluctuations might be the dissociation of the molecules due to the scattering of photons and subsequent movement of the atoms, or a remaining fraction of unpaired atoms.

7.3 Magnetic susceptibility

In analogy to the fluctuation-dissipation relation between the compressibility and density fluctuations used in the previous chapter and [93], the measured values of the spin fluctuations can be related to the magnetic susceptibility χ. The behavior of the spin susceptibility as a function of temperature and interaction strength is of particular interest for the study of phase-transitions to magnetically ordered states, and hence are currently studied in experiments [99] and theory [16]. The fluctuation-dissipation theorem is applicable when the probed system can be regarded to be in grand canonical equilibrium with its surrounding. Due to the column integration in our experiment, the fluctuation-dissipation theorem then reads $k_{\mathrm{B}}T\chi_{\mathrm{col}} = A\delta m^2$, where χ_{col} and $A = \pi w_0^2/2$ are the column-integrated magnetic susceptibility and the area of the probed column, respectively. The latter is determined by the waist w_0^2 of the probe beam. For small volumes and at low temperatures corrections are expected, because correlations between the probed system and its surrounding cannot be neglected [177]. These corrections are roughly estimated to be lower than 25% in our case because of column integration. However, this estimation needs further detailed investigation.

Fig. 7.5 shows the susceptibility scaled by the column density $\chi_{\mathrm{col}}/n^0_{\mathrm{col}}$ as a function of temperature. For higher temperatures, the susceptibility of the weakly interacting Fermi gas decreases as expected, which means that it takes more energy to polarize the gas. The graph also contains the measured susceptibility for the strongly interacting

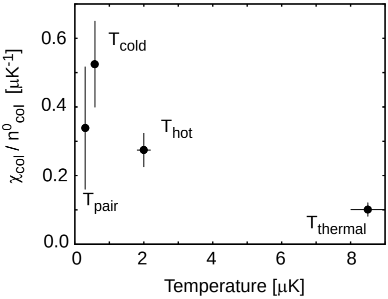

Fig. 7.5: Column integrated magnetic susceptibility scaled by the column density $\chi_{\mathrm{col}}/n^0_{\mathrm{col}}$ as a function of temperature. The graph shows the corresponding values for a weakly interacting gas at three different temperatures and also the measured value for a strongly interacting gas of pairs.

gas of pairs, being roughly a factor of two smaller than the susceptibility of the ideal Fermi gas. However, it is presumably much lower since the susceptibility is supposed to be only due to unpaired atoms which are exponentially suppressed at low temperatures.

7.4 Summary

In conclusion, we have measured the probability distribution of the local spin polarization in a balanced two-component Fermi gas using a new spatially resolved interferometric technique. We have measured the suppression of spin fluctuations due to the Pauli principle of up to 4.5(3)dB for weakly interacting gases and 9.2(8)dB due to pairing for a strongly interacting gas of molecules. Our method is ideally suited to study interaction induced correlations in trapped many-body systems, where the optical density is large. The ability to accurately control the trap depth only in the probed region facilitates measurements of temperature dependent observables. In particular, our observations suggest that the phase space density of the Fermi gas can be locally increased by the additional trap and thermalization occurs even for moderate interparticle interactions. For measurements of the spin polarization in two-dimensional systems (see outlook in chapter 8), the focus of the probe beam could be further reduced, resulting in a larger phase shift per atom, and there would be no further need for column integration. This should allow the observation of possible magnetically ordered domains, consisting exclusively of atoms of one state.

8 Conclusions and outlook

For the last decade, ultracold atomic Fermi gases are increasingly serving as experimental playground to create and study strongly correlated many-body physics with a great variety of highly tunable parameters. Within the scope of this thesis, a new level of control on theses systems has been achieved paving the way for a direct, local access to the underlying many-body physics on a microscopic scale. The experimental key tool for this advance is a pair of identical high-resolution microscope objectives which represents the core element of the new apparatus presented in this work.

Employing a high-resolution imaging setup, we have realized the *in-situ* measurement of density fluctuations in a fermionic quantum gas and presented the first observation of the Pauli exclusion principle in real space. In addition, the simultaneous *in-situ* measurements of density and density fluctuations allowed us to deduce thermodynamic quantities of the Fermi gas via the fluctuation-dissipation theorem. We have established a promising alternative to standard thermometry methods in quantum gases, demonstrating the first fluctuation-based temperature measurement in cold quantum gases.

Combining the precision of interferometry with the high spatial resolution of the microscopes, we have developed a novel shot-noise limited interferometric probe that enabled us to locally measure spin fluctuations in a weakly and strongly interacting Fermi gas.

Moreover, our high-resolution microscope setup has been designed for the site-by-site generation of versatile optical dipole potentials that can be tailored down to below one micrometer. The presented results on the trapping and detection of ultracold fermions in such micro-traps provide a novel route towards a local and flexible manipulation of quantum gases on the length scale of the atomic wave function.

Yet, the full resolution of our microscope setup has not been exploited. For the presented *in-situ* measurements of the density and spin fluctuations in the cigar-shaped 3D Fermi gas, the numerical aperture of the microscope system was decreased on purpose in order to match the depth of field of the imaging system to the extension of the atomic cloud along the line of sight. The latter typically amounts to about $20\,\mu$m, whereas the maximum numerical aperture corresponds to a depth of view of only $3\,\mu$m. Hence, a stronger confinement of the atom cloud will enable us to make use of the full spatial resolution. Currently, we are implementing a so-called light sheet to strongly confine the atoms along the line of sight of the microscopes using a repulsive optical potential created by a blue detuned laser at 532 nm in a TEM_{01} mode [178, 179, 180]. With moderate light power, trap frequencies of some kHz along the confining axis can be maintained over a region of some ten by ten micrometers in the imaging plane. In this small region, the temperature and the chemical potential will be set by the large, unperturbed region of the remaining part of the cloud which acts as a reservoir. The chemical potential will then be hardly affected by the confinement, allowing to reach a quasi-2D situation where the chemical potential is lower than the trapping frequency along the strong confinement. Once having achieved the 2D regime, the full potential of the microscope setup can be used to explore emergent many-body phenomena. In the following we will sketch a few of them.

Not only the mean and variance of density and spin fluctuations can be measured, yet also higher order moments of the atomic distributions contain important information to characterize the quantum state of a many-body system. This "full-counting statistics" approach is a subject of considerable interest in the field of mesoscopic physics, and by now has also attracted theoretical and experimental attention in the field of ultracold atoms [15, 28]. However, current measurements are limited by the resolution and the detection efficiency of the imaging setup. In that respect, our microscope setup will be ideally suited.

Physics often changes dramatically when going from three to lower dimensions. For example in two dimensions, the phase transition of a uniform ideal Bose gas to a BEC does not exist at finite temperature because thermal and quantum fluctuations strongly suppress the formation of long-range order. However, for an interacting 2D Bose gas, another type of phase transition, the topological Berezinski-Kosterlitz-Thouless (BKT) transition, has been predicted and by now become subject of investigations with ultracold quantum gases. A BKT-type phase transition is also expected for strongly interacting quasi-2D Fermi gas near the Feshbach resonance [181], featuring spontaneously created vortex-antivortex pairs at moderate temperatures [182]. Along the BEC-BCS crossover, these have a typical size of the order of the Fermi wavelength, which is about the resolution of our microscope, and are thus of particular interest to be studied with our setup.

Besides measurements of correlation-induced noise properties and the observation of macroscopic phase transitions in bulk systems, our new setup also holds the unique potential to cover the full experimental spectrum from single- and few-atom physics in tightly confining micro-traps to many-body physics in finite optical lattices. An ensemble of a controlled number of deeply degenerate fermions in a single micro-trap, like in [183], will be ideally suited to investigate the physics of finite Fermi systems in nature as for example atomic nuclei. In this context, fundamental questions of few-body physics may be addressed such as the occurrence of pairing in a finite Fermi system [184, 185] or the minimum number of fermionic particles needed to form a superfluid [186].

For the research with ultracold Fermi gases, our apparatus is in the vanguard concerning single-site resolution and single-site addressability, which otherwise has only been implemented in experiments working with bosons [5, 7, 36, 37, 187]. As a next step following the achievement reported on in chapter 5, we may combine an array of 8x8 micro-traps with the previously described 2D confinement in order to generate a finite isotropic 2D optical lattice. The possible small site separation of below one micrometer, together with the low mass of ^{6}Li will lead to tunneling amplitudes of about one kHz. In this lattice, which is localized only in a small region of the large degenerate cloud, the gas will be surrounded by the cold remaining 3D cloud, leading to low temperatures, low compared to the interaction strength and even compared to the tunneling rate. For a half-filled optical lattice, this situation may lead to the formation of charge density waves, a direct analogue of anti-ferromagnetic ordering in strongly repulsive Fermi gases [188]. This phase, featuring alternatingly holes and double occupancy of lattices sites, might then be directly mapped out with the high-resolution imaging setup.

A Physical constants

In this thesis, the following physical constants are used:

Property	Symbol	Value
Speed of light	c	$299792458\,\mathrm{m\,s^{-1}}$
Planck constant	h	$6.6260693(11) \cdot 10^{-34}\,\mathrm{J\,s}$
Planck constant over 2π	$\hbar$	$1.054571628(53) \cdot 10^{-34}\,\mathrm{J\,s}$
Fine-structure constant	α	$7.297352568(24) \cdot 10^{-3}$
Electric constant	ϵ_0	$8.854187817 \cdot 10^{-12}\,\mathrm{F\,m^{-1}}$
Elementary charge	e	$1.60217653(14) \cdot 10^{-19}\,\mathrm{C}$
Electron mass	m_e	$9.1093826(16) \cdot 10^{-31}\,\mathrm{kg}$
Atomic mass constant	u	$1.66053886(28) \cdot 10^{-27}\,\mathrm{kg}$
Boltzmann constant	k_B	$1.3806505(24) \cdot 10^{-23}\,\mathrm{J\,K^{-1}}$
Bohr radius	a_0	$0.5291772108(18) \cdot 10^{-10}\,\mathrm{m}$
Bohr magneton	μ_B	$9.27400949(80) \cdot 10^{-24}\,\mathrm{J\,T^{-1}}$
Nuclear magneton	μ_N	$5.05078343(43) \cdot 10^{-27}\,\mathrm{J\,T^{-1}}$
Electron g-factor	g_e	$2.0023193043718(75)$

Table A.1: Physical constants from CODATA [189].

B Atomic properties of ^{6}Li

B.1 Fundamental physical properties of ^{6}Li

Property	Value
Mass	6.0151214 u
Natural abundance	7.6%
Total electronic spin S	1/2
Total nuclear spin I	1
Total nuclear g_I-factor	-0.0004476540
$2P$ fine structure splitting	10.053044 GHz
$2^2S_{1/2}$ hyperfine ground state splitting	228.2 MHz
Vacuum Wavelength λ_{D1}	670.992421 nm
Natural linewidth Γ_{D1}	$2\pi \times 5.8724$ MHz
Vacuum Wavelength λ_{D2}	670.977338 nm
Natural linewidth Γ_{D2}	$2\pi \times 5.8724$ MHz
Saturation intensity I_{sat} of D_2-line (σ^+-polarized light)	2.54 mW/cm^2

Table B.1: Atomic properties of ^{6}Li [190].

B.2 Atomic level structure of ^{6}Li

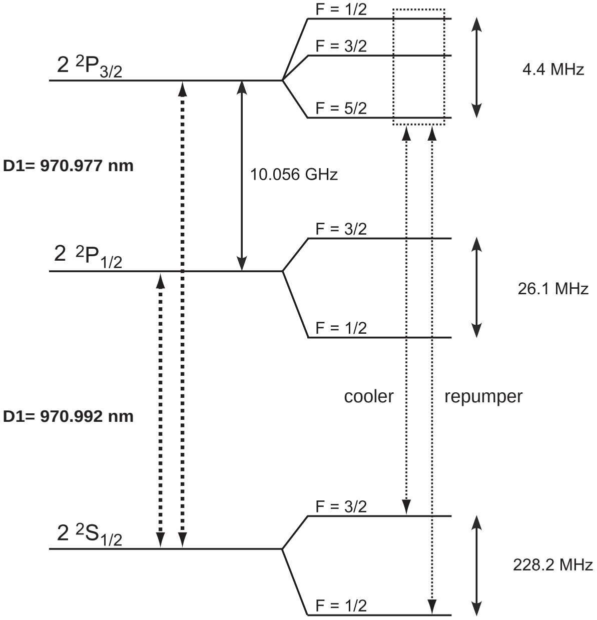
F = 1/2
F = 3/2
2 ^{2}P$_{3/2}$
4.4 MHz
F = 5/2
D1= 970.977 nm
10.056 GHz
F = 3/2
2 ^{2}P$_{1/2}$
26.1 MHz
F = 1/2
cooler
repumper
D1= 970.992 nm
F = 3/2
2 ^{2}S$_{1/2}$
228.2 MHz
F = 1/2

Fig. B.1: Level structure of the ground (S) and excited (P) states of ^{6}Li [190, 191]. Given are the hyperfine spin states F with $F \leq |J \pm I|$, where J is the coupled electronic and orbital spin and $I = 1$ is the nuclear spin. The dashed arrows indicate the transitions used as cooler and repumper for the magneto-optical trap. The splitting in the $2P_{3/2}$ excited state is of the order of the natural linewidth Γ of the D2-line, which can not be resolved. Energy splittings are not to scale.

B.3 Zeeman splitting of ground and excited state levels

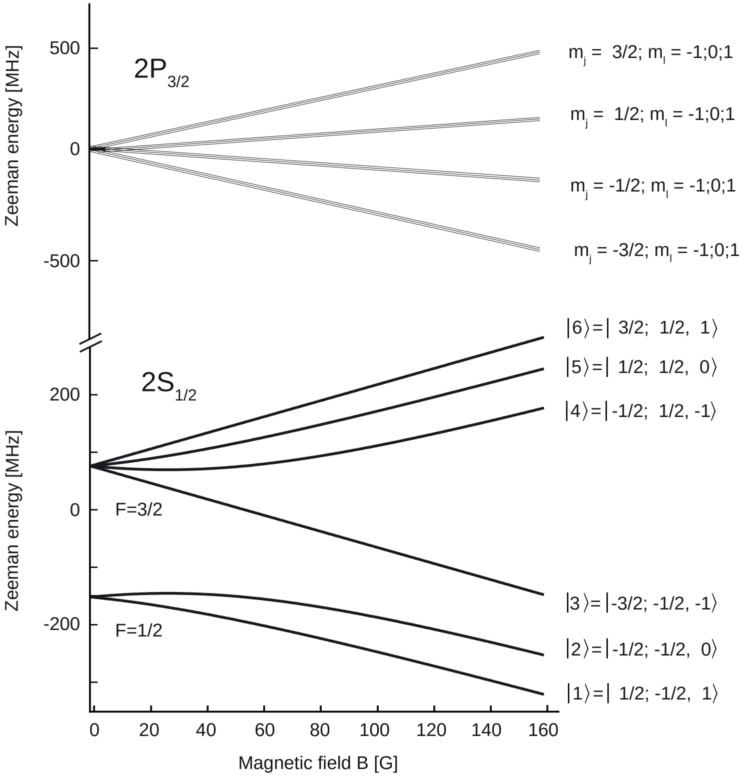

Fig. B.2: Zeeman hyperfine levels of the ^{6}Li electronic $2S_{1/2}$ ground and the $2P_{3/2}$ excited state [190, 191]. For large magnetic fields nuclear and electron spin decouple and optical transitions become closed due to selection rules for electric dipole transitions. The notation for the states $|1\rangle$ to $|6\rangle$ reflects the quantum numbers corresponding to the orientation of the hyperfine angular momentum, the electron spin and the nuclear spin $|m_F; m_s, m_i\rangle$.

C Noise propagation

In this appendix, we provide the derivative of the noise propagation through the imaging process, yielding the noise relation between the output signal of the EMCCD camera and the transmission of probe light as given by equation (6.3) in chapter 6 on the density fluctuations.

Physically, the probing of density fluctuations via absorption imaging consists of several consecutive processes. Photons sent onto the atomic sample are partially absorbed and lead to an attenuation of the initial photon number N_i expressed by the transmission factor t of the probe light. The transmitted photon stream N_o is registered by the EMCCD chip, converted into photoelectrons N_e and finally displayed as electronic counts C. Each step is governed by a distinctive stochastic conversion process. We start with the first noise propagation process when a certain number of incoming photons N_i encounters the atomic cloud causing the transmission of N_o outgoing photons according to $N_o = t \cdot N_i$. On average, the mean number of outgoing photons $\langle N_o \rangle$ is given by

$$\langle N_o \rangle = \sum_{N_o} p(N_o) \cdot N_o = \sum_{N_i, N_o, t} N_o \cdot p(N_o|t, N_i) \cdot p(N_i) \cdot p(t) = \langle t \rangle \cdot \langle N_i \rangle \,. \tag{C.1}$$

Here, $p(x)$ denotes the probability for a certain value x of a quantity. The expression $p(N_o|t, N_i) = \binom{N_i}{N_o} t^{N_o}(1-t)^{N_i - N_o}$ is the conditional probability to have N_o photons at a given N_i and t, following a Bernoulli distribution. Accordingly, we calculate the expectation value of N_o^2:

$$\begin{aligned}
\langle N_o^2 \rangle &= \sum_{N_i, N_o, t} N_o^2 \cdot p(N_o|t, N_i) \cdot p(N_i) \cdot p(t) = \sum_{N_i, t} \langle N_o^2 \rangle_{N_i, t} \cdot p(N_i) \cdot p(t) \\
&= \sum_{N_i, t} (t^2 \cdot N_i^2 + N_i \cdot t - N_i \cdot t^2) \cdot p(N_i) \cdot p(t) \\
&= \sum_t p(t) \cdot t \cdot \langle N_i \rangle + \sum_t p(t) \cdot t^2 \cdot (\langle N_i^2 \rangle - \langle N_i \rangle) \\
&= \langle t \rangle \cdot \langle N_i \rangle + \langle t^2 \rangle \cdot \langle N_i \rangle^2 \,.
\end{aligned} \tag{C.2}$$

In the second step, we used the fact that the variance of Bernoulli distribution is the number of trials times the probability of success times the probability of failure. In addition, for the last transformation we have assumed that the incoming photons are Poissonian distributed for which holds $\langle N_i^2\rangle - \langle N_i\rangle^2 = \langle N_i\rangle$. Combining equations (C.1) and (C.2), we obtain the variance $(\Delta N_o)^2$

$$(\Delta N_o)^2 = \langle N_o^2\rangle - \langle N_o\rangle^2 = \langle N_o\rangle + \langle N_o\rangle^2 \cdot \frac{(\Delta t)^2}{\langle t\rangle^2} \,. \tag{C.3}$$

The same equation holds for the conversion from photons into photoelectrons by the EMCCD camera

$$(\Delta N_e)^2 = \langle N_e\rangle + \langle N_e\rangle^2 \cdot \frac{(\Delta t)^2}{\langle t\rangle^2} \,. \tag{C.4}$$

Finally, we consider the amplification process from photoelectrons into secondary electrons (= counts C) by the EMCCD register. Here, the average gain factor is g. Given a certain number N_e of primary electrons, the probability distribution of counts C is accurately approximated by [166]

$$p(C|N_e)) = \frac{C^{N_e-1}}{(N_e-1)! \cdot g^{N_e}} e^{-\frac{N_e}{g}} \tag{C.5}$$

For a fixed number of primary electrons N_e, this distribution has the mean value $\langle C\rangle = g \cdot N_e$ and the variance $(\Delta C)^2 = g^2 \cdot N_e$. It follows

$$\langle C\rangle = \sum_{N_e,C} C \cdot p(C|N_e) \cdot p(N_e) = \sum_{N_e} g \cdot N_e \cdot p(N_e) = g \cdot \langle N_e\rangle \,, \tag{C.6}$$

and

$$\begin{aligned} \langle C^2\rangle &= \sum_{N_e,C} C^2 \cdot p(C|N_e) \cdot p(N_e) = \sum_{N_e} g^2 \cdot N_e \cdot p(N_e) + \sum_{N_e} g^2 \cdot N_e^2 \cdot p(N_e) \\ &= g^2 \cdot \langle N_e\rangle + g^2 \cdot \left((\Delta N_e)^2 + \langle N_e\rangle^2\right) \,. \end{aligned} \tag{C.7}$$

Hence, the noise relation between the transmission t and the measured count number C reads

$$\begin{aligned} (\delta C)^2 &= \langle C^2\rangle - \langle C\rangle^2 = g^2 \cdot \langle N_e\rangle + g^2 \cdot (\Delta N_e)^2 \\ &= g \cdot \langle C\rangle + g^2 \cdot \left(\langle N_e\rangle + \langle N_e\rangle^2 \cdot \frac{(\Delta t)^2}{t^2}\right) \\ &= 2g \cdot \langle C\rangle + \langle C\rangle^2 \cdot \frac{(\Delta t)^2}{t^2} \,. \end{aligned} \tag{C.8}$$

D Data processing for interferometry

For the determination of the phase fluctuations[1] in chapter 7, we find it advantageous to analyze the correlations between the probe signal (σ^+-polarization) and the reference signal (σ^+-polarization) on each image. This allow us to exploit the similarity of the two interference patterns, and analogous to homodyne techniques to use the σ^+-pattern to noiselessly amplify the signal contained in the σ^--pattern. Fig. D.1 illustrates the different steps of this data processing algorithm. The two parts of the experimental images contain the probe and reference signals (Fig. D.1(a)). A line sum along the direction of the fringes is first computed, yielding a one dimensional fringe pattern signal. The right part of the signal is scaled so that the probe and reference have roughly the same intensity. A filter in Fourier space is then applied to the full scaled signal, conserving only the Fourier components around the fringe spacing. The precise shape of the filter does not influence the obtained results, provided the low frequency components are removed, which contain the envelope of the two fringe patterns and the background. We then compute the autocorrelation function of the processed fringe pattern. Fig. D.1(b) presents a typical autocorrelation signal. A fixed spacing is inserted between the probe and reference signal in the processed fringe pattern before the correlation function is computed. Doing so, the autocorrelation function displays two separated parts. The sum of the correlation functions of the reference with itself and the probe with itself appears at the center. Conversely, the correlation function of the probe with the reference appears at the sides. The center part of this probe-reference (σ^+ - σ^-) correlation signal is selected and the positions of the zero crossings are extracted by linear interpolation of the discrete signal, as depicted in Fig. D.1(b). The mean position of the zero-crossings is taken as the position of the probe fringe pattern with respect to the reference. The ratio of this position to the period of the fringe pattern yields the phase.

Each run of the experiment yields three pictures: one taken in the presence of the atoms (A1), and two pictures taken in the absence of atoms (A2 and A3). The position of the crossings and thus the fringe displacements are measured for each of these pictures. To obtain the distribution of the fringe displacements, the experiments are repeated up to 400 times, over about 2 hours. Over this period, slow drifts of the

---

[1] Parts of chapter 7 and appendix D are adopted from a manuscript in preparation for publication by J. Meineke, J.-P. Brantut, D. Stadler, T. Müller, H. Moritz, and T. Esslinger (2011).

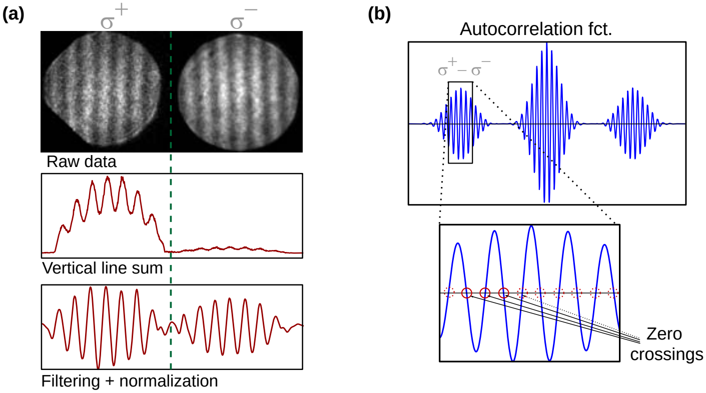

Fig. D.1: Data processing using the correlation method. (a) Raw picture observed on the camera, with the reference signal on the left (σ^+) and the probe signal on the right (σ^-). The actual power ratio of the two is 20, but here the (σ^-) has been re-scaled for demonstration reasons. The signals from the picture is accumulated in the direction of the fringes, yielding a one-dimensional fringe pattern. The visibility of the fringes reflects the ratio of the probe to the local oscillator. The probe signal on the right side has been scaled up, and the full fringe pattern is spatially filtered leaving only the interference contribution. (b) shows the autocorrelation function of the filtered fringe yielding σ^+ - σ^- correlations at both sides, and contributions form σ^+ - σ^+ and σ^- - σ^- correlations in the center. In a selected region centered on the left side of the correlation signal, containing the σ^+ - σ^- correlations, the positions of the zero-crossings of the correlation function are measured.

phase on the atom pictures of up to 5 degrees are observed, most probably due to temperature variations in the environment. In order to compensate for those drifts, a sliding average (over 15 runs) of the positions of the crossings on picture A3 is computed. We take this as a measurement of the drift, and subtract this averaged signal from the positions measured on pictures A1 and A2. This substraction operation amounts to measuring the displacement of each crossing of picture A1 with respect to the corresponding crossing of picture A3, corrected for long term deviations. Taking the average of this corrected quantity over the crossings (i.e. averaging the position measured for all the patterns), we obtain the relative displacement of the fringes on pictures A1 and A2 compared to A3. The ratio of this mean displacement to the period of the fringes yields the phase shift observed on pictures A1 and A2 compared to A3. We now have two phase shifts measured for each run of the experiment, with and without atoms. Thus, we obtain the statistical distribution of the phase shifts in the presence of the atoms from all the shifts of picture A1, together with the distribution of shifts on pictures A2, taken under exactly the same conditions but without atoms. To measure the phase variance due to the atoms, we subtract the phase variance on picture A2 from the phase variance of picture A1.

E Alignment of the microscope setup

In the following sections we present a procedure that has proven to allow a comfortable and accurate alignment of the microscope setup. The given instruction for use summarizes the most essential steps in sequence and lists expedient aids.

Preparation

- Set up a pilot beam (collimated beam with a waist of about 1 mm at 671 nm) on the upper optical breadboard holding the upper microscope.
- Use the last two 2" mirrors in front of the upper microscope to align the pilot beam to hit the atoms held in the FORT and to be perpendicular to the glass cell top window simultaneously. To check whether the beam hits the atoms, observe the blast of atoms along the x-axis imaging or implement a simple imaging system along the z-axis. The orthogonality to the glass cell window can be readily verified by monitoring back reflections from the glass cell through a pinhole.
- Use a flipping mirror or a glass plate on the upper breadboard to send back the reflections onto a CCD camera. Fix this position!
- Set up both 2"/45 ° mirror, below the glass cell and in front of the EMCCD camera. Mount the EMCCD camera (about 900 mm behind glass cell) and record the pilot beam. Check that the aluminum block below the glass cell is in the center position. For this, also mount the piezo translation stage (*Tritor*) and the goniometer with a custom made pinhole. Adjust roughly the angle of the goniometer by putting a mirror on top and mapping the back reflection on the upper CCD camera.
- Fix the position of the massive aluminum block and the two-axis translation stage (*OWIS*) which supports the 2" inch mirror below the glass cell, e.g. using bedstops from two sides.
- Install the 25 mm polarizing beam splitter cube (PBS) in front of the telephoto objective (distance to the aluminum block ∼ 6 cm). Check the orthogonal orientation via the back reflections.
- Set up a second pilot beam from below. Feed it in via the PBS and overlap it

with the pilot beam from above. Map the upper pilot beam and/or the glass cell back reflection of the lower pilot beam onto another CCD camera in the side port path of the PBS.

Installation of the telephoto objective

- Mount the telephoto objective into the four-axis translation (*SPECIAL OPTICS*) stage attached to the linear translation stage (*NEWPORT*). Place the telephoto objective about 450 mm in front of the EMCCD.
- Iteratively, align the angles and the transverse position. For the accurate angles, press a small reflective glass plate against the last lens of the telephoto objective and overlap the back reflection with the incoming pilot beam. For the transverse position, re-align the pilot beam onto the fixed position on the EMCCD.

Installation of the lower microscope objective

- Remove the aluminum block with the 2" mirror, the piezo translation stage and the goniometer, but leave the two-axis translation stage attached to the optical table.
- Remove the goniometer from the aluminum block and the piezo translation stage, and screw the lower part of the *MACOR* tube into the thread of the goniometer. Put the $\lambda/4$ retardation plate on top of the lower *MACOR* tube.
- Insert the microscope objective attached to the upper part of the *MACOR* tube into the slot of the lower Feshbach coil.
- Attach the lower *MACOR* tube to the upper part.
- Lift the goniometer, the *MACOR* tubes and the microscope and slide in the aluminum block. Watch out not do touch the glass cell!
- Reassemble the aluminum block, the goniometer and the two-axis translation stage.
- Roughly adjust the focussing of the microscope by turning the *MACOR* tube in the goniometer thread. The distance between the microscope objective and the lower glass cell window is about 1.2 mm.
- Align the angle of the lower microscope (via goniometer): Put a thin glass plate on top of the most upper lens of the objective: Take care when inserting this plate between the objective and the glass cell. Monitor the back reflection on the upper CCD camera.
- Try to find and image the atoms in the FORT on the EMCCD: Sequentially change the transverse and axial position of the microscope. Once the atoms are found, readjust the focussing with the *MACOR* thread. Then lock the coarse alignment of the axial position.
- Iteratively, align the transverse position (two-axis translation stage and piezo translation stage) and the tilt of the microscope (goniometer). The accurate

tilt can be mapped by the monitored back reflections from the microscope lenses on the CCD cameras. A proper position adjustment is most practicable by overlapping the various back reflections originating from the different lens surfaces of the microscope on the CCD camera, and also by keeping the image of the cloud on the EMCCD camera.

- A fine adjustment of the lower microscope can be accomplished by fluorescence imaging of the trapped cloud in the FORT giving rise to a pronounced contrast effect.

Installation of the upper microscope objective

- Mount the two-axis translation stage (NEWPORT), the piezo translation stage and the goniometer on the upper breadboard. Using the pilot beam, do a coarse adjustment of the transverse position with a pinhole and the tilt via the back reflection from a mirror placed on top of the goniometer.
- Remove the 2" mirror above the glass cell and insert the microscope objective attached to the *MACOR* tube into the coil slot.
- Do a coarse adjustment in the axial direction via the goniometer thread (distance between microscope and glass cell is about 1.2 mm).
- As in the case of the lower microscope, the transverse position and the tilt can be aligned via the various back reflections from the different lens surfaces of the microscope objective. Try to overlap all back reflections simultaneously onto the fixed position of the pilot beam on the upper CCD camera.
- Send a large collimated beam (12 mm waist) at 767 nm through the upper microscope to form a micro-trap. Image the trapped atoms in the micro-trap along the x-axis. Overlap the micro-trap with the FORT along the x-axis and also along the x/y- plane. The latter can be accomplished by monitoring the trap spot on the EMCCD camera. Once the z-position of the micro-trap is fixed, the lower microscope can be re-aligned in axial direction by focussing onto the minimum waist of the micro-trap.

Bibliography

[1] I. Bloch, J. Dalibard, and W. Zwerger. 'Many-body physics with ultracold gases'. *Rev. Mod. Phys.* **80**, 885–964 (2008).

[2] S. Giorgini, L. P. Pitaevskii, and S. Stringari. 'Theory of ultracold atomic Fermi gases'. *Rev. Mod. Phys.* **80**(4), 1215–1274 (2008).

[3] W. Ketterle and M. W. Zwierlein. 'Making, probing and understanding ultracold Fermi gases'. Proceedings of the International School of Physics "Enrico Fermi", Course CLXIV, Varenna, edited by M. Inguscio, W. Ketterle, and C. Salomon, IOS Press, Amsterdam (2008).

[4] K. D. Nelson, X. Li, and D. S. Weiss. 'Imaging single atoms in a three-dimensional array'. *Nat Phys* **3**(8), 556–560 (2007).

[5] T. Gericke, P. Würtz, D. Reitz, T. Langen, and H. Ott. 'High-resolution scanning electron microscopy of an ultracold quantum gas'. *Nature Phys.* **4**, 949–953 (2008).

[6] W. S. Bakr, J. I. Gillen, A. Peng, S. Fölling, and M. Greiner. 'A quantum gas microscope for detecting single atoms in a Hubbard-regime optical lattice'. *Nature* **462**(7269), 74–77 (2009).

[7] J. F. Sherson, C. Weitenberg, M. Endres, M. Cheneau, I. Bloch, and S. Kuhr. 'Single-atom-resolved fluorescence imaging of an atomic Mott insulator'. *Nature* **467**(7311), 68–72 (2010).

[8] P. C. Martin and J. Schwinger. 'Theory of Many-Particle Systems. I'. *Phys. Rev.* **115**(6), 1342–1373 (1959).

[9] P. A. M. Dirac. 'On the Theory of Quantum Mechanics'. *Proceedings of the Royal Society of London. Series A* **112**(762), 661–677 (1926).

[10] E. Fermi. 'Sulla quantizzazione del gas perfetto monoatomico'. *Rend. Lincei* **3**, 145–9 (1926).

[11] A. Zannoni. 'On the Quantization of the Monoatomic Ideal Gas'. *arXiv:cond-mat/9912229* (1999).

[12] E. Altman, E. Demler, and M. D. Lukin. 'Probing many-body states of ultracold atoms via noise correlations'. *Phys. Rev. A* **70**(1), 013603– (2004).

[13] M. Anderson, J. Ensher, M. Matthews, C. Wieman, and E.A.Cornell. ‘Observation of Bose-Einstein condensation in a dilute atomic vapor’. *Science* **269**, 198 (1995).

[14] K. B. Davis, M. O. Mewes, M. R. Andrews, N. J. van Druten, D. S. Durfee, D. M. Kurn, and W. Ketterle. ‘Bose-Einstein Condensation in a Gas of Sodium Atoms’. *Phys. Rev. Lett.* **75**, 3969 (1995).

[15] W. Belzig, C. Schroll, and C. Bruder. ‘Density correlations in ultracold atomic Fermi gases’. *Physical Review A* **75**(6), 063611 (2007).

[16] A. Recati and S. Stringari. ‘Spin fluctuations, susceptibility and the dipole oscillation of a nearly ferromagnetic Fermi gas’. *arXiv:cond-mat/1007.4504* (2010).

[17] R. Hanbury Brown and R. Twiss. ‘A Test of a New Type of Stellar Interferometer on Sirius’. *Nature* **178**, 1046 (1956).

[18] A. Öttl, S. Ritter, M. Köhl, and T. Esslinger. ‘Correlations and Counting Statistics of an Atom Laser’. *Phys. Rev. Lett.* **95**(9), 090404– (2005).

[19] S. Fölling, F. Gerbier, A. Widera, O. Mandel, T. Gericke, and I. Bloch. ‘Spatial quantum noise interferometry in expanding ultracold atom clouds’. *Nature* **434**(7032), 481–484 (2005).

[20] T. Rom, T. Best, D. van Oosten, U. Schneider, S. Fölling, B. Paredes, and I. Bloch. ‘Free fermion antibunching in a degenerate atomic Fermi gas released from an optical lattice’. *Nature* **444**, 733 (2006).

[21] M. Greiner, C. Regal, and D. Jin. ‘Probing the Excitation Spectrum of a Fermi Gas in the BCS-BEC CrossoverRegime’. *Physical Review Letters* **94**, 070403 (2005).

[22] D. Greif, L. Tarruell, T. Uehlinger, R. Jördens, and T. Esslinger. ‘Probing nearest-neighbor correlations of ultracold fermions in an optical lattice’. *arXiv:cond-mat/1012.0845* (2010).

[23] G. Veeravalli, E. Kuhnle, P. Dyke, and C. J. Vale. ‘Bragg Spectroscopy of a Strongly Interacting Fermi Gas’. *Phys. Rev. Lett.* **101**(25), 250403 (2008).

[24] E. D. Kuhnle, H. Hu, X. Liu, P. Dyke, M. Mark, P. D. Drummond, P. Hannaford, and C. J. Vale. ‘Universal Behavior of Pair Correlations in a Strongly Interacting Fermi Gas’. *Physical Review Letters* **105**(7), 070402 (2010).

[25] E. D. Kuhnle, S. Hoinka, P. Dyke, H. Hu, P. Hannaford, and C. J. Vale. ‘Temperature dependence of the contact in a unitary Fermi gas’. *arXiv:cond-mat/1012.2626* (2010).

[26] J. Esteve, J.-B. Trebbia, T. Schumm, A. Aspect, C. I. Westbrook, and I. Bouchoule. ‘Observations of Density Fluctuations in an Elongated Bose Gas: Ideal Gas and Quasicondensate Regimes’. *Phys. Rev. Lett.* **96**(13), 130403– (2006).

[27] N. Gemelke, X. Zhang, C.-L. Hung, and C. Chin. ‘In situ observation of incompressible Mott-insulating domains in ultracold atomic gases’. *Nature* **460**(7258), 995–998 (2009).

[28] J. Armijo, T. Jacqmin, K. V. Kheruntsyan, and I. Bouchoule. ‘Probing Three-Body Correlations in a Quantum Gas Using the Measurement of the Third Moment of Density Fluctuations’. *Physical Review Letters* **105**(23), 230402 (2010).

[29] Schwabl. *Quantenmechanik für Fortgeschrittene*. 4. Auflage (Springer-Verlag, Berlin, 2005).

[30] G. M. Bruun, B. M. Andersen, E. Demler, and A. S. Sørensen. ‘Probing Spatial Spin Correlations of Ultracold Gases by Quantum Noise Spectroscopy’. *Phys. Rev. Lett.* **102**(3), 030401– (2009).

[31] R. Grimm, M. Weidemüller, and Y. B. Ovchinnikov. ‘Optical dipole traps for neutral atoms’. *Adv. At. Mol. Opt. Phys.* **42**, 95 (2000).

[32] I. Bloch. ‘Ultracold quantum gases in optical lattices’. *Nat Phys* **1**(1), 23–30 (2005).

[33] D. Jaksch, C. Bruder, J. I. Cirac, C. W. Gardiner, and P. Zoller. ‘Cold bosonic atoms in optical lattices’. *Phys. Rev. Lett.* **81**, 3108–3111 (1998).

[34] D. Jaksch and P. Zoller. ‘The cold atom Hubbard toolbox’. *Ann. Phys.* **315**, 52–79 (2005).

[35] T. Esslinger. ‘Fermi-Hubbard Physics with Atoms in an Optical Lattice’. *Annual Review of Condensed Matter Physics* **1**(1), 129–152 (2010).

[36] P. Würtz, T. Langen, T. Gericke, A. Koglbauer, and H. Ott. ‘Experimental demonstration of single-site addressability in a two-dimensional optical lattice’. *Phys. Rev. Lett.* **103**, 080404 (2009).

[37] W. S. Bakr, A. Peng, M. E. Tai, R. Ma, J. Simon, J. I. Gillen, S. Fölling, L. Pollet, and M. Greiner. ‘Probing the Superfluid-to-Mott Insulator Transition at the Single-Atom Level’. *Science* **329**(5991), 547–550 (2010).

[38] B. DeMarco and D. S. Jin. ‘Onset of Fermi Degeneracy in a Trapped Atomic Gas’. *Science* **285**, 1703 (1999).

[39] A. G. Truscott, K. E. Strecker, W. I. McAlexander, G. B. Partridge, and R. G. Hulet. ‘Observation of Fermi Pressure in a Gas of Trapped Atoms’. *Science* **291**, 2570 (2001).

[40] F. Schreck, L. Khaykovich, K. L. Corwin, G. Ferrari, T. Bourdel, J. Cubizolles, and C. Salomon. ‘Quasipure Bose-Einstein Condensate Immersed in a Fermi Sea’. *Phys. Rev. Lett.* **87**(8), 080403– (2001).

[41] G. Roati, F. Riboli, G. Modugno, and M. Inguscio. ‘Fermi-Bose Quantum Degenerate ^{40}K$-^{87}$Rb Mixture with Attractive Interaction’. *Phys. Rev. Lett.* **89**, 150403 (2002).

[42] Z. Hadzibabic, C. A. Stan, K. Dieckmann, S. Gupta, M. W. Zwierlein, A. Görlitz, and W. Ketterle. ‘Two-Species Mixture of Quantum Degenerate Bose and Fermi Gases’. *Phys. Rev. Lett.* **88**, 160401 (2002).

[43] S. R. Granade, M. E. Gehm, K. M. O’Hara, and J. E. Thomas. ‘All-Optical Production of a Degenerate Fermi Gas’. *Phys. Rev. Lett.* **88**, 120405 (2002).

[44] C. Chin, R. Grimm, P. Julienne, and E. Tiesinga. 'Feshbach resonances in ultracold gases'. *Rev. Mod. Phys.* **82**(2), 1225– (2010).

[45] M. Houbiers, H. T. C. Stoof, W. I. McAlexander, and R. G. Hulet. 'Elastic and inelastic collisions of ^6Li atoms in magnetic and optical traps'. *Phys. Rev. A* **57**(3), R1497–R1500 (1998).

[46] J. Dalibard. 'Collisional dynamics of ultra-cold atomic gases'. In *Bose-Einstein Condensation in Atomic Gases*, edited by M. Inguscio, S. Stringari, and C. Wieman (IOS Press, 1999).

[47] M. Bartenstein, A. Altmeyer, S. Riedl, R. Geursen, S. Jochim, C. Chin, J. Hecker-Denschlag, R. Grimm, A. Simoni, E. Tiesinga, C. J. Williams, and P. S. Julienne. 'Precise determination of ^{6}Li cold collision parameters by radio-frequency spectroscopy on weakly bound molecules'. *Phys. Rev. Lett.* **94**, 103201 (2005).

[48] C. H. Schunck, M. W. Zwierlein, C. A. Stan, S. M. F. Raupach, W. Ketterle, A. Simoni, E. Tiesinga, C. J. Williams, and P. S. Julienne. 'Feshbach resonances in fermionic ^{6}Li'. *Phys. Rev. A* **71**(4), 045601– (2005).

[49] K. O'Hara, S. Hemmer, M. Gehm, S. Granade, and J. Thomas. 'Observation of a Strongly Interacting Degenerate Fermi Gas of Atoms'. *Science* **298**, 2179 (2002).

[50] S. Jochim, M. Bartenstein, A. Altmeyer, G. Hendl, S. R. A. Chin, J. Hecker-Denschlag, and R. Grimm. 'Bose-Einstein Condensation of Molecules'. *Science* **302**, 2101 (2003).

[51] M. W. Zwierlein, C. A. Stan, C. H. Schunck, S. M. F. Raupach, S. Gupta, Z. Hadzibabic, and W. Ketterle. 'Observation of Bose-Einstein Condensation of Molecules'. *Phys. Rev. Lett.* **91**, 250401 (2003).

[52] M. Greiner, C. A. Regal, and D. S. Jin. 'Emergence of a molecular Bose-Einstein condensate from a Fermi gas'. *Nature* **426**(6966), 537–540 (2003).

[53] J. Bardeen, L. N. Cooper, and J. R. Schrieffer. 'Theory of Superconductivity'. *Phys. Rev.* **108**, 1175 (1957).

[54] M. Bartenstein, A. Altmeyer, S. Riedl, S. Jochim, C. Chin, J. H. Denschlag, and R. Grimm. 'Crossover from a molecular Bose-Einstein condensate to a degenerate Fermi gas'. *Phys. Rev. Lett.* **92**, 120401 (2004).

[55] C. A. Regal, M. Greiner, and D. S. Jin. 'Observation of Resonance Condensation of Fermionic Atom Pairs'. *Phys. Rev. Lett.* **92**, 040403 (2004).

[56] T. Bourdel, L. Khaykovich, J. Cubizolles, J. Zhang, F. Chevy, M. Teichmann, L. Tarruell, S. Kokkelmans, and C. Salomon. 'Experimental Study of the BEC-BCS Crossover Region in Lithium 6'. *Phys. Rev. Lett.* **93**, 050401 (2004).

[57] C. Chin, M. Bartenstein, A. Altmeyer, S. Riedl, S. Jochim, J. H. Denschlag, and R. Grimm. 'Observation of the Pairing Gap in a Strongly Interacting Fermi Gas'. *Science* **305**(5687), 1128–1130 (2004).

[58] M. W. Zwierlein, C. A. Stan, C. H. Schunck, S. M. F. Raupach, A. J. Kerman,

and W. Ketterle. ‘Condensation of Pairs of Fermionic Atoms near a Feshbach Resonance’. *Phys. Rev. Lett.* **92**, 120403 (2004).

[59] G. B. Partridge, K. E. Strecker, R. I. Kamar, M. W. Jack, and R. G. Hulet. ‘Molecular Probe of Pairing in the BEC-BCS Crossover’. *Phys. Rev. Lett.* **95**, 020404 (2005).

[60] C. H. Schunck, Y.-i. Shin, A. Schirotzek, and W. Ketterle. ‘Determination of the fermion pair size in a resonantly interacting superfluid’. *Nature* **454**(7205), 739–743 (2008).

[61] M. W. Zwierlein, J. R. Abo-Shaeer, A. Schirotzek, C. H. Schunck, and W. Ketterle. ‘Vortices and superfluidity in a strongly interacting Fermi gas’. *Nature* **435**, 1047 (2005).

[62] G. B. Partridge, W. Li, R. I. Kamar, Y.-a. Liao, and R. G. Hulet. ‘Pairing and Phase Separation in a Polarized Fermi Gas’. *Science* **311**(5760), 503–505 (2006).

[63] M. W. Zwierlein, C. H. Schunck, A. Schirotzek, and W. Ketterle. ‘Direct observation of the superfluid phase transition in ultracold Fermi gases’. *Nature* **442**, 54 (2006).

[64] Y. Shin, M. W. Zwierlein, C. H. Schunck, A. Schirotzek, and W. Ketterle. ‘Observation of Phase Separation in a Strongly Interacting Imbalanced Fermi Gas’. *Phys. Rev. Lett.* **97**(3), 030401–4 (2006).

[65] Y. Shin, M. W. Zwierlein, C. H. Schunck, A. Schirotzek, and W. Ketterle. ‘Observation of Phase Separation in a Strongly Interacting Imbalanced Fermi Gas’. *Phys. Rev. Lett.* **97**, 030401 (2006).

[66] Y. Shin, C. H. Schunck, A. Schirotzek, and W. Ketterle. ‘Phase diagram of a two-component Fermi gas with resonant interactions’. *Nature* **451**(7179), 689–693 (2008).

[67] J. P. Gaebler, J. T. Stewart, T. E. Drake, D. S. Jin, A. Perali, P. Pieri, and G. C. Strinati. ‘Observation of pseudogap behaviour in a strongly interacting Fermi gas’. *Nat Phys* **6**(8), 569–573 (2010).

[68] T.-L. Ho. ‘Universal Thermodynamics of Degenerate Quantum Gases in the Unitarity Limit’. *Phys. Rev. Lett.* **92**(9), 090402– (2004).

[69] M. Horikoshi, S. Nakajima, M. Ueda, and T. Mukaiyama. ‘Measurement of Universal Thermodynamic Functions for a Unitary Fermi Gas’. *Science* **327**(5964), 442–445 (2010).

[70] S. Nascimbène, N. Navon, K. J. Jiang, F. Chevy, and C. Salomon. ‘Exploring the thermodynamics of a universal Fermi gas’. *Nature* **463**(7284), 1057–1060 (2010).

[71] N. Navon, S. Nascimbène, F. Chevy, and C. Salomon. ‘The Equation of State of a Low-Temperature Fermi Gas with Tunable Interactions’. *Science* pp. science.1187582– (2010).

[72] C. J. Pethick and H. Smith. *Bose-Einstein Condensation in Dilute Gases*

(Cambridge University Press, 2002).

[73] L. Pitaevskii and S. Stringari. *Bose-Einstein Condensation* (Oxford University Press, 2003).

[74] K. Huang. *Statistical Mechanics* (John Wiley & Sons, 1987).

[75] S. Jochim, M. Bartenstein, A. Altmeyer, G. Hendl, C. Chin, J. H. Denschlag, and R. Grimm. 'Pure Gas of Optically Trapped Molecules Created from Fermionic Atoms'. *Phys. Rev. Lett.* **91**, 240402 (2003).

[76] C. A. Regal, C. Ticknor, J. L. Bohn, and D. S. Jin. 'Creation of ultracold molecules from a Fermi gas of atoms'. *Nature* **424**, 47 (2003).

[77] J. Sakurai. *Modern Quantum Mechanics* (Addison-Wesley, 1994).

[78] C. Chin. 'A simple model of Feshbach molecules'. *arXiv:cond-mat/0506313v2* (2005).

[79] H. Feshbach. 'Unified theory of nuclear reactions'. *Ann. Phys.* **5**, 357 (1958).

[80] A. Moerdijk, B. Verhaar, and A. Axelsson. 'Resonances in ultracold collisions of ^{6}Li, ^{7}Li, and ^{23}Na'. *Physical Review A* **51**, 4852 (1995).

[81] S. Kokkelmans. private communication (2004).

[82] K. M. O'Hara, S. L. Hemmer, S. R. Granade, M. E. Gehm, J. E. Thomas, V. Venturi, E. Tiesinga, and C. J. Williams. 'Measurement of the zero crossing in a Feshbach resonance of fermionic 6Li'. *Phys. Rev. A* **66**(4), 041401– (2002).

[83] D. M. Eagles. 'Possible Pairing without Superconductivity at Low Carrier Concentrations in Bulk and Thin-Film Superconducting Semiconductors'. *Phys. Rev.* **186**, 456 (1969).

[84] A. J. Leggett. *Modern Trends in the Theory of Condensed Matter* (Springer-Verlag, Berlin, 1980).

[85] M. Zwierlein, C. Stan, C. Schunck, S. Raupach, A.J.Kerman, and W. Ketterle. 'Condensation of Pairs of Fermionic Atoms near a Feshbach Resonance'. *Physical Review Letters* **92**, 120403 (2004).

[86] J. Kinast, S. L. Hemmer, M. E. Gehm, A. Turlapov, and J. E. Thomas. 'Evidence for Superfluidity in a Resonantly Interacting Fermi Gas'. *Phys. Rev. Lett.* **92**, 150402 (2004).

[87] D. Petrov, C. Salomon, and G. Shlyapnikov. 'Weakly Bound Dimers of Fermionic Atoms'. *Physical Review Letters* **93**, 090404 (2004).

[88] M. Randeria. 'Ultracold Fermi gases: Pre-pairing for condensation'. *Nat Phys* **6**(8), 561–562 (2010).

[89] Y. an Liao, A. S. C. Rittner, T. Paprotta, W. Li, G. B. Partridge, R. G. Hulet, S. K. Baur, and E. J. Mueller. 'Spin-imbalance in a one-dimensional Fermi gas'. *Nature* **467**(7315), 567–569 (2010).

[90] P. Fulde and R. A. Ferrell. 'Superconductivity in a Strong Spin-Exchange Field'. *Phys. Rev.* **135**(3A), A550–A563 (1964).

[91] A. I. Larkin and Y. N. Ovchinnikov. ‘Inhomogeneous state of superconductors’. *Sov. Phys. JETP* **20**, 762–769 (1965).

[92] Schwabl. *Statistische Mechanik.* 3. Auflage (Springer-Verlag, Berlin, 2006).

[93] T. Müller, B. Zimmermann, J. Meineke, J.-P. Brantut, T. Esslinger, and H. Moritz. ‘Local Observation of Antibunching in a Trapped Fermi Gas’. *Phys. Rev. Lett.* **105**, 040401 (2010).

[94] M. Yasuda and F. Shimizu. ‘Observation of Two-Atom Correlation of an Ultracold Neon Atomic Beam’. *Phys. Rev. Lett.* **77**(15), 3090– (1996).

[95] M. Greiner, O. Mandel, T. Esslinger, T. Hansch, and I. Bloch. ‘Quantum phase transition from a superfluid to a Mott insulator in a gas of ultracold atoms’. *Nature* **415**, 39–44 (2002).

[96] T. Jeltes, J. M. McNamara, W. Hogervorst, W. Vassen, V. Krachmalnicoff, M. Schellekens, A. Perrin, H. Chang, D. Boiron, A. Aspect, and C. I. Westbrook. ‘Comparison of the Hanbury Brown-Twiss effect for bosons and fermions’. *Nature* **445**(7126), 402–405 (2007).

[97] M. Henny, S. Oberholzer, C. Strunk, T. Heinzel, K. Ensslin, M. Holland, and C. Schönenberger. ‘The Fermionic Hanbury Brown and Twiss Experiment’. *Science* **284**(5412), 296–298 (1999).

[98] W. D. Oliver, J. Kim, R. C. Liu, and Y. Yamamoto. ‘Hanbury Brown and Twiss-Type Experiment with Electrons’. *Science* **284**(5412), 299–301 (1999).

[99] C. Sanner, E. J. Su, A. Keshet, W. Huang, J. Gillen, R. Gommers, and W. Ketterle. ‘Speckle Imaging of Spin Fluctuations in a Strongly Interacting Fermi Gas’. *Phys. Rev. Lett.* **106**(1), 010402 (2011).

[100] Q. Zhou and T. Ho. ‘Universal Thermometry for Quantum Simulation’. *arXiv:cond-mat/0908.3015* (2009).

[101] J. L. Bohn. ‘Cooper pairing in ultracold ^{40}K using Feshbach resonances’. *Phys. Rev. A* **61**(5), 053409 (2000).

[102] C. Regal and D. Jin. ‘Measurement of Positive and Negative Scattering Lengths in a Fermi Gasof Atoms’. *Physical Review Letters* **90**, 230404 (2003).

[103] F. Schreck, G. Ferrari, K. L. Corwin, J. Cubizolles, L. Khaykovich, M.-O. Mewes, and C. Salomon. ‘Sympathetic cooling of bosonic and fermionic lithium gases towards quantum degeneracy’. *Phys. Rev. A* **64**(1), 011402 (2001).

[104] Z. Hadzibabic, S. Gupta, C. A. Stan, C. H. Schunck, M. W. Zwierlein, K. Dieckmann, and W. Ketterle. ‘Fiftyfold Improvement in the Number of Quantum Degenerate Fermionic Atoms’. *Phys. Rev. Lett.* **91**(16), 160401 (2003).

[105] B. Zimmermann. ‘Microscopy of ultracold fermionic lithium’. Ph.D. thesis, ETH Zurich, Diss. ETH No. 19085 (2010).

[106] A. Mosk, S. Jochim, H. Moritz, T. Elsässer, M. Weidemüller, and R. Grimm. ‘Resonator-enhanced optical dipole trap for fermionic lithium atoms’. *Optics Letters* **26**(23), 1837–1839 (2001).

[107] T. L. Gustavson, A. P. Chikkatur, A. E. Leanhardt, A. Görlitz, S. Gupta, D. E. Pritchard, and W. Ketterle. 'Transport of Bose-Einstein Condensates with Optical Tweezers'. *Phys. Rev. Lett.* **88**(2), 020401– (2001).

[108] H. J. Metcalf and P. van der Straten. *Laser Cooling and Trapping* (Springer-Verlag, New York, 1999).

[109] R. D. Swenumson and U. Even. 'Continuous flow reflux oven as the source of an effusive molecular Cs beam'. *Review of Scientific Instruments* **52**(4), 559–561 (1981).

[110] W. D. Phillips. 'Nobel Lecture: Laser cooling and trapping of neutral atoms'. *Rev. Mod. Phys.* **70**(3), 721–741 (1998).

[111] L. Ricci, M. Weidemüller, T. Esslinger, A. Hemmerich, C. Zimmermann, V. Vuletic, W. König, and T. W. Hänsch. 'A compact grating-stabilized diode laser system for atomic physics'. *Optics Communications* **117**(5-6), 541–549 (1995).

[112] G. C. Bjorklund, M. D. Levenson, W. Lenth, and C. Ortiz. 'Frequency modulation (FM) spectroscopy'. *Applied Physics B: Lasers and Optics* **32**(3), 145–152 (1983).

[113] C. Zipkes. 'Lasersystem zum Kühlen, Fangen und Abbilden von fermionischem Lithium'. Master's thesis, ETH Zurich (2007).

[114] U. Schünemann, H. Engler, R. Grimm, M. Weidemüller, and M. Zielonkowski. 'Simple scheme for tunable frequency offset locking of two lasers'. *Rev. Sci. Instrum.* **70**(1), 242–243 (1999).

[115] S. Jochim. 'Bose-Einstein Condensation of Molecules'. Ph.D. thesis, Leopold-Franzens-Universität Innsbruck (2004).

[116] J. Dalibard and C. Cohen-Tannoudji. 'Laser cooling below the Doppler limit by polarization gradients: simple theoretical models'. *J. Opt. Soc. Am. B* **6**(11), 2023–2045 (1989).

[117] E. L. Raab, M. Prentiss, A. Cable, S. Chu, and D. E. Pritchard. 'Trapping of Neutral Sodium Atoms with Radiation Pressure'. *Phys. Rev. Lett.* **59**(23), 2631– (1987).

[118] T. B. Ottenstein, T. Lompe, M. Kohnen, A. N. Wenz, and S. Jochim. 'Collisional Stability of a Three-Component Degenerate Fermi Gas'. *Phys. Rev. Lett.* **101**(20), 203202 (2008).

[119] Siegman. *Lasers* (University Science Books, 1986).

[120] R. W. P. Drever, J. L. Hall, F. V. Kowalski, J. Hough, G. M. Ford, A. J. Munley, and H. Ward. 'Laser phase and frequency stabilization using an optical resonator'. *Applied Physics B: Lasers and Optics* **31**, 97–105 (1983). 10.1007/BF00702605.

[121] E. D. Black. 'An introduction to Pound–Drever–Hall laser frequency stabilization'. *Am. J. Phys.* **69**, 79–87 (2001).

[122] L. Simon and W. T. Strunz. 'Bose gas in a single-beam optical dipole trap'.

Phys. Rev. A **81**(6), 063620 (2010).

[123] R. Chati. 'Entwicklung eines Regelkreises auf einem FPGA mit Hilfe von LabVIEW zur Experimentkontrolle'. Technical report, ETH Zurich, Quantum Optics Group (2008).

[124] M. Bucher. 'Implementation of a PID control on an FPGA to spatially stabilize a laser beam'. Technical report, ETH Zurich, Quantum Optics Group (2010).

[125] T. Schnider. 'Design of a Second Generation Optical Lattice Experiment for an Ultra-Cold ^{40}K Quantum Gas'. Master's thesis, ETH Zurich (2009).

[126] W. Ketterle, D. Durfee, and D. Stamper-Kurn. 'Making, probing and understanding Bose-Einstein condensates'. In *Bose-Einstein condensation in atomic gases, Proceedings of the InternationalSchool of Physics "Enrico Fermi", Course CXL*, edited by M. Inguscio, S. Stringari, and C. Wieman (IOS Press, Amsterdam, 1999).

[127] G. Reinaudi, T. Lahaye, Z. Wang, and D. Guéry-Odelin. 'Strong saturation absorption imaging of dense clouds of ultracold atoms'. *Opt. Lett.* **32**(21), 3143–3145 (2007).

[128] T. Ottenstein. 'Few-body physics in ultracold Fermi gases'. Ph.D. thesis, Ruperto-Carola University of Heidelberg (2010).

[129] F. Zernike. 'Phase contrast, a new method for the microscopic observation of transparent objects'. *Physica* **9**(7), 674–698 (1942).

[130] M. R. Andrews, M.-O. Mewes, N. J. van Druten, D. S. Durfee, D. Kurn, and W. Ketterle. 'Direct, Nondestructive Observation of a Bose Condensate'. *Science* **273**, 84–87 (1996).

[131] C. C. Bradley, C. A. Sackett, and R. G. Hulet. 'Bose-Einstein Condensation of Lithium: Observation of Limited Condensate Number'. *Physical Review Letters* **78**(6), 985 (1997).

[132] C. C. Bradley, C. A. Sackett, and R. G. Hulet. 'Bose-Einstein Condensation of Lithium'. *Bra. J. Phys.* **27**, 154–161 (1997).

[133] T. Stöferle. 'Exploring atomic quantum gases in optical lattices'. Ph.D. thesis, ETH Zurich, Diss. ETH No. 16109 (2005).

[134] R. Grimm. 'Ultracold Fermi gases in the BEC-BCS crossover: a review from the Innsbruck perspective'. Proceedings of the International School of Physics "Enrico Fermi", Course CLXIV, Varenna, edited by M. Inguscio, W. Ketterle, and C. Salomon, IOS Press, Amsterdam (2008).

[135] K. M. O'Hara, M. E. Gehm, S. R. Granade, and J. E. Thomas. 'Scaling laws for evaporative cooling in time-dependent optical traps'. *Phys. Rev. A* **64**(5), 051403– (2001).

[136] L. Luo, B. Clancy, J. Joseph, J. Kinast, A. Turlapov, and J. E. Thomas. 'Evaporative cooling of unitary Fermi gas mixtures in optical traps'. *New Journal of Physics* **8**(9), 213 (2006).

[137] D. S. Petrov. 'Three-body problem in Fermi gases with short-range interparticle

interaction'. *Phys. Rev. A* **67**(1), 010703 (2003).

[138] J. Cubizolles, T. Bourdel, S. Kokkelmans, G. V. Shlyapnikov, and C. Salomon. 'Production of Long-Lived Ultracold ^{2}Li Molecules from a Fermi Gas'. *Phys. Rev. Lett.* **91**, 240401 (2003).

[139] D. Petrov and G. Shlyapnikov. 'Interatomic collisions in a tightly confined Bose gas'. *Physical Review A* **64**, 012706 (2001).

[140] B. Zimmermann, T. Müller, J. Meineke, T. Esslinger, and H. Moritz. 'High-resolution imaging of ultracold fermions in microscopically tailored optical potentials'. *New Journal of Physics* **13**(4), 043007 (2011).

[141] E. Hecht. *Optics* (Addison-Wesley, 2002), 4th edition.

[142] T. Ottenstein. 'A new objective for high resolution imaging of Bose-Einstein condensates'. Master's thesis, Kirchhoff Institute of Physics, Heidelberg (2006).

[143] J. W. Goodman. *Introduction to Fourier optics* (McGraw-Hill, 1996), 2nd edition.

[144] M. Albiez, R. Gati, J. Fölling, S. Hunsmann, M. Cristiani, and M. K. Oberthaler. 'Direct Observation of Tunneling and Nonlinear Self-Trapping in a Single Bosonic Josephson Junction'. *Phys. Rev. Lett.* **95**(1), 010402– (2005).

[145] V. Boyer, R. M. Godun, G. Smirne, D. Cassettari, C. M. Chandrashekar, A. B. Deb, Z. J. Laczik, and C. J. Foot. 'Dynamic manipulation of Bose-Einstein condensates with a spatial light modulator'. *Phys. Rev. A* **73**(3), 031402 (2006).

[146] W. H. Heathcote, E. Nugent, B. T. Sheard, and C. J. Foot. 'A ring trap for ultracold atoms in an RF-dressed state'. *New Journal of Physics* **10**(4), 043012 (2008).

[147] K. Henderson, C. Ryu, C. MacCormick, and M. G. Boshier. 'Experimental demonstration of painting arbitrary and dynamic potentials for Bose–Einstein condensates'. *New Journal of Physics* **11**(4), 043030 (2009).

[148] S. K. Schnelle, E. D. van Ooijen, M. J. Davis, N. R. Heckenberg, and H. Rubinsztein-Dunlop. 'Versatile two-dimensional potentials for ultra-cold atoms'. *Optics Express* **16**, 1405–1412 (2008).

[149] T. P. Meyrath, F. Schreck, J. L. Hanssen, C.-S. Chuu, and M. G. Raizen. 'Bose-Einstein condensate in a box'. *Phys. Rev. A* **71**(4), 041604 (2005).

[150] R. Dumke, M. Volk, T. Müther, F. B. J. Buchkremer, G. Birkl, and W. Ertmer. 'Micro-optical Realization of Arrays of Selectively Addressable Dipole Traps: A Scalable Configuration for Quantum Computation with Atomic Qubits'. *Phys. Rev. Lett.* **89**(9), 097903 (2002).

[151] R. W. Mu, Z. L. Wang, Y. L. Li, X. M. Ji, and J. P. Yin. 'A controllable double-well optical trap for cold atoms (or molecules) using a binary se plate: experimental demonstration and Monte Carlo simulation'. *Eur. Phys. J. D* **59**(2), 291–300 (2010).

[152] N. Friedman, L. Khaykovich, R. Ozeri, and N. Davidson. 'Compression of cold atoms to very high densities in a rotating-beam blue-detuned optical trap'.

Phys. Rev. A **61**(3), 031403 (2000).

[153] R. Onofrio, D. S. Durfee, C. Raman, M. Köhl, C. E. Kuklewicz, and W. Ketterle. 'Surface Excitations of a Bose-Einstein Condensate'. *Phys. Rev. Lett.* **84**(5), 810–813 (2000).

[154] http://gnuradio.org/trac. 'GNU radio project, software and instructions' .

[155] http://gnuradio.org/trac/wiki/USRP. 'GNU radio project, USRP documents' .

[156] J. Meineke. 'PhD thesis in preparation'. Ph.D. thesis, Swiss Federal Institute of Technology, Zürich (2011/2012).

[157] W. Zwerger. 'Mott-Hubbard transition of cold atoms in optical lattices'. *Journal of Optics B* **5**, S9 (2003).

[158] X. Du, Y. Zhang, and J. E. Thomas. 'Inelastic Collisions of a Fermi Gas in the BEC-BCS Crossover'. *Phys. Rev. Lett.* **102**(25), 250402 (2009).

[159] R. Scheunemann, F. S. Cataliotti, T. W. Hänsch, and M. Weitz. 'Resolving and addressing atoms in individual sites of a CO_2-laser optical lattice'. *Phys. Rev. A* **62**(5), 051801 (2000).

[160] M. Karski, L. Förster, J.-M. Choi, A. Steffen, N. Belmechri, W. Alt, D. Meschede, and A. Widera. 'Imprinting patterns of neutral atoms in an optical lattice using magnetic resonance techniques'. *New Journal of Physics* **12**(6), 065027 (2010).

[161] B. DeMarco, J. Bohn, J. J.P. Burke, M. Holland, and D. Jin. 'Measurement of p-Wave Threshold Law Using Evaporatively Cooled FermionicAtoms'. *Physical Review Letters* **82**, 4208 (1999).

[162] M. W. Zwierlein, Z. Hadzibabic, S. Gupta, and W. Ketterle. 'Spectroscopic Insensitivity to Cold Collisions in a Two-State Mixture of Fermions'. *Phys. Rev. Lett.* **91**(25), 250404 (2003).

[163] C. Sanner, E. J. Su, A. Keshet, R. Gommers, Y.-i. Shin, W. Huang, and W. Ketterle. 'Suppression of Density Fluctuations in a Quantum Degenerate Fermi Gas'. *Phys. Rev. Lett.* **105**(4), 040402 (2010).

[164] C. I. Westbrook. 'Suppressed fluctuations in Fermi gases'. *Physics* **3**, 59 (2010).

[165] Z. Hadzibabic. 'Quantum gases: The cold reality of exclusion'. *Nature Physics* **6**(9), 643–644 (2010).

[166] A. G. Basden, C. A. Haniff, and C. D. Mackay. 'Photon counting strategies with low-light-level CCDs'. *Monthly Notices of the Royal Astronomical Society* **345**(3), 985–991 (2003).

[167] J. Esteve, C. Gross, A. Weller, S. Giovanazzi, and M. K. Oberthaler. 'Squeezing and entanglement in a Bose-Einstein condensate'. *Nature* **455**(7217), 1216–1219 (2008).

[168] R. Gati, B. Hemmerling, J. Fölling, M. Albiez, and M. K. Oberthaler. 'Noise Thermometry with Two Weakly Coupled Bose-Einstein Condensates'. *Phys.*

Rev. Lett. **96**(13), 130404 (2006).

[169] S. Manz, R. Bücker, T. Betz, C. Koller, S. Hofferberth, I. E. Mazets, A. Imambekov, E. Demler, A. Perrin, J. Schmiedmayer, and T. Schumm. 'Two-point density correlations of quasicondensates in free expansion'. *Phys. Rev. A* **81**(3), 031610– (2010).

[170] O. J. Luiten, M. W. Reynolds, and J. T. M. Walraven. 'Kinetic theory of the evaporative cooling of a trapped gas'. *Phys. Rev. A* **53**(1), 381– (1996).

[171] C. N. Yang. 'Concept of Off-Diagonal Long-Range Order and the Quantum Phases of Liquid He and of Superconductors'. *Rev. Mod. Phys.* **34**(4), 694–704 (1962).

[172] G.-B. Jo, Y.-R. Lee, J.-H. Choi, C. A. Christensen, T. H. Kim, J. H. Thywissen, D. E. Pritchard, and W. Ketterle. 'Itinerant Ferromagnetism in a Fermi Gas of Ultracold Atoms'. *Science* **325**(5947), 1521–1524 (2009).

[173] K. Eckert, O. Romero-Isart, M. Rodriguez, M. Lewenstein, E. S. Polzik, and A. Sanpera. 'Quantum non-demolition detection of strongly correlated systems'. *Nat Phys* **4**(1), 50–54 (2008).

[174] T. Roscilde, M. Rodríguez, K. Eckert, O. Romero-Isart, M. Lewenstein, E. Polzik, and A. Sanpera. 'Quantum polarization spectroscopy of correlations in attractive fermionic gases'. *New Journal of Physics* **11**(5), 055041 (2009).

[175] S. A. Aljunid, M. K. Tey, B. Chng, T. Liew, G. Maslennikov, V. Scarani, and C. Kurtsiefer. 'Phase Shift of a Weak Coherent Beam Induced by a Single Atom'. *Phys. Rev. Lett.* **103**(15), 153601 (2009).

[176] J. E. Lye, J. J. Hope, and J. D. Close. 'Nondestructive dynamic detectors for Bose-Einstein condensates'. *Phys. Rev. A* **67**(4), 043609 (2003).

[177] G. E. Astrakharchik, R. Combescot, and L. P. Pitaevskii. 'Fluctuations of the number of particles within a given volume in cold quantum gases'. *Phys. Rev. A* **76**(6), 063616 (2007).

[178] T. Meyrath, F. Schreck, J. Hanssen, C. Chuu, and M. Raizen. 'A high frequency optical trap for atoms using Hermite-Gaussian beams'. *Opt. Express* **13**(8), 2843–2851 (2005).

[179] N. L. Smith, W. H. Heathcote, G. Hechenblaikner, E. Nugent, and C. J. Foot. 'Quasi-2D confinement of a BEC in a combined optical and magnetic potential'. *Journal of Physics B: Atomic, Molecular and Optical Physics* **38**(3), 223 (2005).

[180] M. Robert-de Saint-Vincent, J.-P. Brantut, B. Allard, T. Plisson, L. Pezzé, L. Sanchez-Palencia, A. Aspect, T. Bourdel, and P. Bouyer. 'Anisotropic 2D Diffusive Expansion of Ultracold Atoms in a Disordered Potential'. *Phys. Rev. Lett.* **104**(22), 220602 (2010).

[181] W. Zhang, G.-D. Lin, and L.-M. Duan. 'Berezinskii-Kosterlitz-Thouless transition in a trapped quasi-two-dimensional Fermi gas near a Feshbach resonance'. *Phys. Rev. A* **78**(4), 043617 (2008).

[182] S. S. Botelho and C. A. R. Sá de Melo. 'Vortex-Antivortex Lattice in Ultracold Fermionic Gases'. *Phys. Rev. Lett.* **96**(4), 040404 (2006).

[183] F. Serwane, G. Zürn, T. Lompe, T. B. Ottenstein, A. N. Wenz, and S. Jochim. 'Deterministic preparation of a tunable few-fermion system'. *arXiv:cond-mat/1101.2124* (2011).

[184] G. M. Bruun and H. Heiselberg. 'Cooper pairing and single-particle properties of trapped Fermi gases'. *Phys. Rev. A* **65**(5), 053407 (2002).

[185] H. Heiselberg. 'Pairing of fermions in atomic traps and nuclei'. *Phys. Rev. A* **68**(5), 053616 (2003).

[186] A. B. Migdal. 'Superfluidity and the moments of inertia of nuclei'. *Nuclear Physics* **13**(5), 655 – 674 (1959).

[187] C. Weitenberg, M. Endres, J. F. Sherson, M. Cheneau, P. Schauß, T. Fukuhara, I. Bloch, and S. Kuhr. 'Single-Spin Addressing in an Atomic Mott Insulator'. *arXiv:cond-mat/1101.2076* (2011).

[188] A. F. Ho, M. A. Cazalilla, and T. Giamarchi. 'Quantum simulation of the Hubbard model: The attractive route'. *Phys. Rev. A* **79**(3), 033620 (2009).

[189] CODATA. 'CODATA recommended values' (2002).

[190] M. E. Gehm. 'Properties of ^{6}Li'. Ph.D. thesis, Duke University (2003).

[191] E. Arimondo, M. Inguscio, and P. Violino. 'Experimental determinations of the hyperfine structure in the alkali atoms'. *Review of Modern Physics* **49**, 31 (1977).

Publications related to this thesis

1. ***Local observation of antibunching in a trapped Fermi gas***
   T. Müller, B. Zimmermann , J. Meineke, J.-P. Brantut, T. Esslinger,
   and H. Moritz
   Physical Review Letters **105**, 040401 (2010).
2. ***High-resolution imaging of ultracold fermions in microscopically tailored optical potentials***
   B. Zimmermann* , T. Müller*, J. Meineke, T. Esslinger, and H. Moritz
   New Journal of Physics **13**, 043007 (2011).
   * These authors contributed equally to the presented work.
3. ***Interferometric measurement of local spin-fluctuations in a quantum gas***
   J. Meineke, J.-P. Brantut, D. Stadler, T. Müller, H. Moritz, and T. Esslinger
   In preparation for publication, (2011).

Acknowledgements

An dieser Stelle möchte ich die Gelegenheit nutzen, mich ganz herzlich bei all denjenigen Menschen zu bedanken, die diese Arbeit erst ermöglicht haben und auf deren Hilfe und Unterstützung ich während meiner Doktorandenzeit an der ETH stets zurückgreifen konnte.

- An erster Stelle gebührt mein besonderer Dank Tilman Esslinger, zum einen für die Ermöglichung und Betreuung meiner Doktorarbeit, und zum anderen für die Schaffung einer so menschlichen und stimulierenden Arbeitsatmosphäre. Sein intuitives Verständnis von Physik und die bemerkenswerte Fähigkeit, komplexe Sachverhalte auf den Punkt zu bringen, haben mich immer wieder beeindruckt. Ich hoffe einiges davon mit auf den Weg nehmen zu können. Danke für das entgegenbebrachte Vertrauen.
- Ein ganz großer Dank gilt auch Henning Moritz, dem geistigen und schöpferischen Vater des Lithium-Experiments. Er hat sich das Konzept zur Apparatur ausgedacht und das Experiment durch seinen unermüdlichen Einsatz kontinuierlich vorangetrieben. Danke vor allem für die hervorragende Betreuung meiner Doktorarbeit. Ich wünsche einen erfolgreichen Start und gutes Gelingen in Hamburg.
- Mit Bruno Zimmermann, meinem Doktorandenkollegen der ersten Stunde, verbindet mich die einmalige und positive Erfahrung, gemeinsam in einem leeren Labor begonnen zu haben und jetzt ein funktionierendes und vor allem solides Experiment zu hinterlassen, das sicherlich auch in Zukunft noch spannende Physik liefern wird. Danke für die tolle und heitere Zusammenarbeit, und ganz besonders danke ich für die aktive Gastfreundschaft, die mir die Integration in die Schweiz mehr als angenehm gemacht hat.
- Ich bin froh, dass wir Jakob Meineke der theoretischen Physik abgewinnen konnten und mit ihm einen tatkräftigen und sehr qualifizierten Mitstreiter für unser Experiment gefunden haben. Ohne seinen Beitrag wären wir sicherlich nicht so schnell vorangekommen.
- Im letzten Jahr hat sich das Lithium-Team erweitert. Von unserem neuen PostDoc Jean-Philipp Brantut und unserem neuen Doktoranden David Stadler konnte das Experiment sehr schnell profitieren. Danke für die unschätzbaren

Impulse und Euren intensiven Einsatz.

- Für die tolle Arbeitsatmosphäre und die inspirierende Zusammenarbeit möchte ich mich beim jetzigen QO-Team bedanken. Das sind die Kollegen vom Cavity-Experiment Kristian Baumann, Ferdinand Brenecke, Rafael Mottl und Tobias Donner, sowie Leticia Taruell, Daniel Greif, Thomas Uehlinger und Gregor Jotzu vom Gitter-Experiment. Ich wünsche weiterhin viel Erfolg bei Euren spannenden Experimenten.
- Den ehemaligen QO-Gruppenmitglieder Stephan Ritter, Silvan Leinss, Christine Guerlin, Robert Jördens, Niels Strohmaier, Kenneth Günter, Thomas Bourdel, Michael Köhl und Yosuke Takasu danke ich für die tolle gemeinsame Zeit, auch ausserhalb des Labors.
- Alexander Frank ist von unschätzbarem Wert für unsere Gruppe. Sein Elektronik-Rundum-Sorglos-Paket trägt maßgeblich zum Gelingen unserer Experimente bei. Danke für die stets prompte Hilfe.
- Bei Veronica Bürgisser bedanke ich mich für die stets perfekte Administration. Ihr Einsatz für die Gruppe erlaubt uns genügend Freiraum für die Physik.
- Ganz besonders möchte ich mich bei den beiden "Altgedienten" Paul Herrmann und Jean-Pierre Stucki bedanken, auf deren langjährige Erfahrung in Sachen Experimentalphysik ich sehr gerne vertraut habe. Vor allem möchte ich Pauls Hilfe bei der Revidierung des Ofen und der Wasserkühlung am Zeeman-Slower erwähnen. Allen Mitarbeitern der mechanischen Werkstätten und der übrigen Departementsbetriebe, den Ingenieuren des D-PHYS und den Lagermitarbeitern danke ich für die kooperative Zusammenarbeit. Die hohe Qualität ihrer Arbeit habe ich sehr zu schätzen gelernt.
- Mein inniger Dank gebührt Martina für Ihre Liebe, Unterstützung und Geduld.
- Zuletzt möchte ich meiner Familie danken, ganz besonders meinen Eltern. Ihr habt mir all das ermöglicht und mich auf meinem Weg stets unterstützt. Vielen, vielen Dank!

Curriculum Vitae

Personal data

Name	Torben Müller
Date of birth	18.06.1980
Place of birth	Weilburg, Germany
Nationality	German

Education

06/2000	Abitur (Gymnasium Tilemannschule Limburg, Germany)
07/2009 – 09/2001	Civilian service (paramedic)
10/2001 – 07/2006	Study of physics at Johannes Gutenberg University Mainz, Germany
09/2003	Vordiplom in physics (University of Mainz, Germany)
03/2004–04/2006	Scholarship holder of the *”Studienstiftung des Deutschen Volkes”*
10/2004–03/2005	Research project at Imperial College, London *”Production of Cold Molecular Radicals by Laser Ablation“* under the supervision of Prof. Dr. E. Hinds
07/2005 – 07/2006	Diploma thesis (University of Mainz, Germany) *”Exploring excited Bloch bands in optical lattices via stimulated Raman transitions“* under the supervision of Prof. Dr. I. Bloch
07/2006	Diploma in physics
10/2006 – 03/2011	Graduate studies at ETH Zurich, Switzerland (Swiss Federal Institute of Technology) under the supervision of Prof. Dr. T. Esslinger
03/2011	PhD thesis (ETH Zurich, Switzerland) *”Microscopic Probing and Manipulation of Ultracold Fermions“*